DIPARTIMENTO DI INGEGNERIA INDUSTRIALE

Dottorato di Ricerca in Ingegneria Meccanica

XII Ciclo N.S. (2011-2013)

"Development of a Model-Based Diagnosis Algorithm oriented towards Solid Oxide Fuel Cell Systems: Approach and Application"

Ing. Pierpaolo Polverino

Il Tutor

Ch.mo Prof. Cesare Pianese

Il Co-tutor

Dott. Ing. Angelo Esposito

Il Coordinatore

Ch.mo Prof. Vincenzo Sergi

The research leading to the results presented in this dissertation received funding from the European Community's Seventh Framework Programme (FP7/2007-2013) for the Fuel Cell and Hydrogen Joint Technology Initiative under grant agreement N° 245128 (project GENIUS – Generic diagnosis instrument for SOFC systems).

The support of University of Salerno (FARB projects) is also acknowledged.

The scholarship related to this doctoral research activity was provided by the University of Salerno.

To my mom Alba
and my girlfriend Francesca
… Always

"A new type of thinking is essential
if mankind is to survive
and move toward higher levels".

Albert Einstein
Atomic Education Urged by Einstein,
New York Times, 1946.

Table of contents

Acknowledgements

Writing a dissertation is a breathing spell and an introspective process, through which it is possible to review what has been done and what the future could set aside. Even though I have already written two dissertations (the Bachelor and the Master ones), this thesis is a “premiere”, mainly because it derives from the contemplated choice to extend the educational path. The experience I have gained in writing this manuscript has helped me clarifying the reason of my choices and, of course, the core of my work. However, all the goals I have reached so far could not have been achieved without the guidance and the support of all the people who have sustained me during this complex journey.

First and foremost, I would like to thank my mom Alba, who has always been a point of reference to me even during the toughest moments. She has given me (and still does) the strength to carry on, even when I thought and feared she would not have been able to.

I need to express my intense gratitude to Prof. Cesare Pianese, University of Salerno, who gave me the opportunity to live this great experience. His expertise and his determination have driven me to improve day by day and to make the most of my efforts. He deeply contributed to my personal and professional growth, by providing me the possibility to make my unforgettable experience in Germany and involving me in several European Projects.

A special acknowledgment goes to Dr. Angelo Esposito, European Institute of Energy Research (EIFER) in Karlsruhe, who followed me from my “first steps” (I mean my Master Thesis!) to the completion of this intense and hard work. He helped me more than once understanding the core features of my research and he was a bright guide during the activity performed at the EIFER laboratories.

I wish to acknowledge Dr. Marco Sorrentino, Dr. Dario Marra and Ing. Arturo Di Filippi, who helped me during the development of the whole diagnostic methodology and from whose works I gathered most of the bases exploited in this thesis.

Concerning my experience in Germany, I want to thank in particular Dr. Nadia Yousfi-Steiner, as tutor of my activity at the EIFER institute. Her kindness and patience made my experience enjoyable and remarkable. Furthermore, a special thanks is mandatory to Mr. Bastian Ludwig, who guided me during my contribution to the experimental activity on the Galileo 1000N system.

I would also like to acknowledge the Department of Industrial Engineering at the University of Salerno and in particular the coordinator of the doctoral program, Prof. Vincenzo Sergi, for the work done to guarantee the opportunity of this educational path to the students.

The results presented in this thesis have been carried out in the framework of the European Community's Seventh Framework Programme (FP7/2007-2013) for the Fuel Cells and Hydrogen Joint Technology Initiative under grant agreement n° 245128 (Project GENIUS – *Generic diagnosis instrument for SOFC systems*). Special thanks goes to all the participants of the GENIUS project, in particular, the coordinator Philippe Moçotéguy (EIFER), Dr. Boris Iwanschitz (HEXIS AG), Mr. Hanspeter Kuratli (HEXIS AG) and Dr. Andreas Mai (HEXIS AG), for their technical support and expertise on the Galileo 1000N system.

Particular thanks goes to all my old and new colleagues – actually friends – of the Laboratory I5 of the Department of Industrial Engineering at the University of Salerno and to all the supporting staff: Andrea, Cecilia, Dario, Gianpaolo, Gina, Gaetano, Ivan, Raffaele and Rocco. With them I shared most of my activity in the lab and I really appreciate their friendship and patience "standing" me even during the toughest periods.

Furthermore, I would also like to thank all the friends who have supported me during this journey, sharing happiness, stress and … beers!

Last in these acknowledgments, but first in my heart, I want to express my endless gratitude to my girlfriend Francesca. Her incredible love and support in all my decisions, even in the wrong ones, has given me the will to go further, to aim at higher targets and to become a better person.

List of figures

List of tables

Nomenclature

Acronyms

APU	Auxiliary Power Unit
BOP	Balance Of Plant
CHP	Combined Heat and Power
CLT	Central Limit Theorem
CPO	Catalytic Partial Oxidizer
CPR	Critical Pressure Ratio
CV	Coefficient of Variation
DC/AC	Direct Current/Alternate Current
D-CODE	DC/DC converter-based diagnostic for PEM systems
DESIGN	Degradation signature identification for stack operation diagnostic
EIFER	European Institute for Energy Research
FCH JU	Fuel Cells and Hydrogen Joint Undertaking
FDI	Fault Detection and Isolation
FTA	Fault Tree Analysis
FSM	Fault Signature Matrix
GENIUS	Generic diagnosis instrument for SOFC systems
GUI	Graphic User Interface
HHV	Higher Heating Value
LSM	Strontium-doped Lanthanum Manganite
OC	Operating Characteristics
PEM	Polymer Electrolyte Membrane
pdf	Probability Density Function
PI	Proportional-Integral
RAM	Reliability, Availability and Maintainability
RTD	Research, Technological development and Demonstration

SOFC	Solid Oxide Fuel Cell
WGS	Water Gas Shift
YSZ	Yttria-Stabilized Zirconia
ZCA	Zero Capacity Approach

Roman Symbols

A	surface [m^2]
C	fluid heat capacity [$J\ K^{-1}$]
c	specific heat [$J\ kg^{-1}\ K^{-1}$]
C_D	empirical discharge coefficient [-]
c_p	specific heat at constant pressure [$J\ kg^{-1}\ K^{-1}$]
D	diameter [m]
d	scaling factor [-]
$\dot{E}$	energy flow rate [W]
F	Faraday constant [$C\ mol^{-1}$]
f	friction factor [-]
H_0	null hypothesis [-]
H_1	alternative hypothesis [-]
h	specific enthalpy [$J\ mol^{-1}$]
J	current density [$A\ m^{-2}$]
K	solid heat capacity [$J\ K^{-1}$]
L	length [m]
M	molar mass [$kg\ mol^{-1}$]
$\dot{m}$	mass flow [$kg\ s^{-1}$]
N	measurement noise [$-^{(1)(2)(3)}$]
n	sample size [-]
$\dot{n}$	molar flow [$mol\ s^{-1}$]
n_{cells}	cells number [-]
P	power [W]
p	pressure [Pa]
Q	thermal power [W]
R	gas constant [$J\ kg^{-1}\ K^{-1}$]

(1) The measurement unit can vary according to the context.
(2) The variable can be either a scalar, a vector, or a matrix.
(3) Possible multiple measurements units in case of vector or matrix.

r	residual [-[(1)(2)(3)]]
S_p	pooled standard deviation [-[(1)]]
s	analytical symptom [-[(2)]]
T	temperature [K]
t	time [s]
t_0	t statistic [-]
U	heat transfer coefficient [W m^{-2} K^{-1}]
U_f	fuel utilization [-]
V	voltage [V]
v	velocity [m s^{-1}]
VOL	solid parts volume [m^3]
X	real system input variables [-[(1)(2)(3)]]
x	molar fraction [-]
Y	real system output variables [-[(1)(2)(3)]]
$\hat{Y}$	simulated output variables [-[(1)(2)(3)]]
z	distance [m]

Greek Symbols

α	hypothesis test significance level [-]
β	pressure ration [-]
γ	polytropic coefficient [-]
Δ_0	reference populations averages difference [-[(1)]]
δ	quantizer step size [-[(1)]]
ε	fault coefficient [-]
η	efficiency [-]
λ	excess of air [-]
λ_{CPO}	CPO oxygen to carbon ratio [-]
μ	average [-[(1)(2)(3)]]
ξ	fault coefficient [-]
ρ	density [kg m^{-3}]
σ	standard deviation [-[(1)(2)(3)]]
τ	threshold level [-[(1)(2)(3)]]

(1) The measurement unit can vary according to the context.
(2) The variable can be either a scalar, a vector, or a matrix.
(3) Possible multiple measurements units in case of vector or matrix.

χ	fault coefficient [-]

Subscripts

1	before leakage
2	after leakage
AIR	air
B	blower
c	cold fluid
cer	ceramic
EM	electric motor
F	faulty
H	hole
h	hot fluid
HE	air pre-heater
in	inlet
NET	net
out	outlet
PB	post-burner
ref	fuel pre-reformer
samp	sample
SOFC	SOFC stack lumped volume

Summary

The present dissertation illustrates the complete procedure of developing a model-based diagnosis algorithm and shows its application to a pre-commercial Solid Oxide Fuel Cell (SOFC) system. The main motivations of this work can be found in the increasing demand for diagnostic techniques aimed at both ensuring system optimal performance and required lifetime. The purpose of a diagnostic algorithm is to detect and isolate undesired states (i.e. faults) within the system under study (e.g. both the stack and balance of plant – BOP – components of an SOFC system). The understanding of the main mechanisms inducing malfunctions or, in the worst case, abrupt interruptions (i.e. failures) of the system allows the definition of suitable control strategies to avoid these events and to ensure the required system performance.

Among all the diagnostic techniques available in literature, a model-based fault diagnosis methodology is taken into account. According to this technique, a process model is exploited to treat the data measured during the system operation to obtain insightful indicators of the system state. More in details, the measured data are compared to simulated variables to extract features, i.e. mathematical residuals, which are representative of the monitored variables behavior. The residuals computation is performed during the *monitoring process*. The detection of undesired or unexpected system behaviors is carried out through the comparison of the collected residuals to reference threshold values. These values are suitably tuned to take into account several uncertainties, like model inaccuracy and measurement noise, and the necessity to detect incipient faults. The comparison of the computed residuals to these thresholds allows the generation of analytical symptoms, which indicate whether an undesired event is occurring or not. The arise of a symptom points out that the behavior of the related variable is abnormal, completing the *detection process*. At this stage, although the occurrence of a fault is observed, its type is still unknown. To accomplish this last task, a reference set of information is exploited for the identification of

the malfunction nature and for the isolation of the faulty component(s) (*isolation process*). These information comprise the main faults the system can be affected by and the variables conditioned by the occurrence of these faults. The symptoms collected during the detection phase, which are representative of the variables showing an irregular (or unexpected) behavior, are compared to the reference information to correctly locate the fault on the system.

The first part of this manuscript entails the design procedure of a generic model-based diagnosis algorithm, describing in detail the development of the mathematical model and the definition of the reference information required by the methodology. The presented model derives from an SOFC system model, developed by Sorrentino et al. [1][2]. This model is based on a lumped approach and is able to simulate both steady and dynamic behaviors of the system state variables. The stack is assumed planar and co-flow and its voltage behavior is represented by a non-linear regression, function of fuel utilization, current density, excess of air and the temperatures at the stack inlet and at the stack outlet. On one hand, the temperature regulation of the stack inlet flows is achieved by means of two by-pass valves, one at the anode side and one at the cathode side. On the other hand, the stack inner temperature control is fulfilled through a PI controller, which acts on the air blower power to regulate the inlet air flow. The novelty of the presented model consists in several sub-models specifically developed to simulate the considered system both in normal and in faulty conditions. This feature allows the utilization of the model for the offline definition of the reference information exploited for the isolation process.

The reference information help in the isolation of the undesired event(s) occurring in the system during its normal operation. This task can be achieved through the correct identification of the relationships among the symptoms, generated during the detection process, and the possible faults the system can cope with. In the present work, a Fault Signature Matrix (FSM) developed by Arsie et al. [4] following a Fault Tree Analysis (FTA), is considered as the basis for the development of the aforementioned reference information. This FSM is improved through the simulation of different kind of faults in order to understand both the direct and the indirect correlations among the faults and the system variables. Moreover, the real effects induced by the considered fault on the affected variables are defined in terms of quantitative drifts of the

variables values from the normal condition. To achieve this task, the fault sub-models previously introduced are exploited to simulate the effects of several faults.

For the purpose of this work, five different faults related to an SOFC system are simulated, that are i) an increase in the air blower mechanical losses, ii) an air leakage, iii) a temperature controller failure, iv) a pre-reformer heat exchange surface corrosion and v) an increase in cell ohmic resistance. Through the faults simulation, a set of residuals is collected and its comparison with different threshold levels highlights the quantitative relationships among the faults and the conditioned variables. In this way, it is possible to point out the difference between an FSM developed through a heuristic approach (i.e. the FTA), accounting only for the qualitative relationships among the faults and the symptoms, and the one developed considering also the system sensitivity to the faults magnitude.

The second part of this thesis entails the characterization and the validation of the developed diagnostic algorithm on a pre-commercial micro-Combined Heat and Power (μ-CHP) SOFC system, the Galileo 1000N, manufactured by the Swiss company HEXIS AG. A dedicated experimental activity has been performed in order to induce controlled faulty states in the system. The further original feature of this work consists in the design of well-defined procedures to mimic faults on a real SOFC system. In some cases, the procedure involves only suitable maneuvers via software control system, whereas in other cases, specific hardware modifications are required.

Before applying the developed diagnostic algorithm to the Galileo 1000N, an adaptation process is performed, in order to suit each part of the algorithm to the system under analysis. The need for a fast and handy model, which can be rapidly tuned by the algorithm user, led to the development of a maps-based model to simulate the system in normal conditions and to extract residuals. This model exploits the average values of the monitored variables through numerical maps, which are function of the operating condition set-point values. Additionally, the FSM improved off-line via faults simulation is further modified taking into account the number of variables practically monitorable and the system control strategies. Moreover, a statistical hypothesis test is implemented in order to evaluate the probability of false alarm and missed fault. These analysis is significant for the correct interpretation of the generated symptoms

during the detection phase.

Concerning the impact of the present research activity, the developed algorithm aims at improving both the performance and the lifetime of an SOFC system by its implementation into a comprehensive control strategy. In this way it is possible to associate to the diagnosis of the system status specific counteractions performed by the system controller. In this way, both the manufacturer and the final users can obtain significant advantages in terms of management costs reduction (i.e. maintenance and materials costs) and overall efficiency increase.

To summarize, the main contributions and innovative features of this research activity are listed in the following:

- the development of a diagnostic algorithm following a model-based approach;
- the improvement of an FSM, based on an FTA, through the exploitation of fault models simulation to evaluate the sensitivity of the monitored variables to the faults magnitudes;
- the implementation of a statistical hypothesis test for the evaluation of false alarm and miss detection probability;
- the design of specific procedures and hardware modifications to mimic faults in a controlled way on a real SOFC system (i.e. the Galileo 1000N) for the diagnostic algorithm validation;
- the offline and the online validation of the proposed algorithm implemented on-board and controlled through a graphic user interface.

It is worth noting that the innovative features presented in this manuscript are a pioneering contribution in the available literature. Most of the results presented in this dissertation have been carried out within the framework of the European Project GENIUS (Generic diagnosis instrument for SOFC systems) and received funding from the European Community's Seventh Framework Programme (FP7/2007-2013) for the Fuel Cell and Hydrogen Joint Technology Initiative under grant agreement N° 245128.

CHAPTER 1 Introduction

Nowadays the increasing interest in renewable energies drives researchers' activity towards new energy power systems, such as Solid Oxide Fuel Cells (SOFCs). It is well known in the literature that an SOFC is one of the most promising energy conversion systems, and this is mainly due to several positive features: (i) high energy conversion efficiency, (ii) low pollutant emissions (only CO_2 is released during the reforming process), (iii) high flexibility and modularity, (iv) low acoustic emissions and (v) potential use in cogeneration applications, as a consequence of the high operating temperatures. Another important advantage is the possibility to exploit the internal reforming capabilities of SOFCs, thus simple pre-reformers can be implemented allowing the practical use of conventional fuels (e.g. Diesel, natural gas, methanol, propane, etc.), and achieving in this way a reduction of components manufacturing and system management costs [1][2][3][4][16]. On the other hand, a wide commercial diffusion of these energy systems is hindered by materials and production costs and durability issues.

Current SOFC systems are characterized by low reliability of both stack and balance of plant (BOP) due to a large variety of possible degradation mechanisms and malfunctions that may occur in real world operation [1]. Indeed, due to higher degradation rates, the SOFC system lifetime is still not long enough with respect to the durability requirements of either stationary (about 40,000 h) and transportation (about 20,000 h) applications [4][5]. In order to meet these lifetime targets, to improve degradation prevention capabilities and to optimize control actions, specific diagnostic methodologies coupled with real-time system monitoring are needed. The development of an effective diagnostic algorithm, suitably coupled with adaptive control strategies, allows to modify the control laws while the system is running, thus resulting in both lifetime and performance improvement. Moreover, due to their intrinsic features, adaptive control algorithms require the development of dynamic models, with high prediction accuracy and fast computational time. The

same characteristics are essential also for model-based diagnosis. This methodology entails developing a reliable and accurate model, which can simulate the monitored system in all its operating conditions. Through the comparison between the measured signals and the simulated ones, a specific inference process leads to the estimation of the current system status. Compared to traditional methods, like monitoring and automatic protection, the fault diagnosis supervision is the only one capable to detect incipient faults (early detection), with high accuracy both during steady and transient states and for several system components (process components, sensors, actuators, etc.) [9][21].

Generally, ensuring safe operation of a complex system entails accounting not only for the optimal operating set-points of the main variables and parameters, but also for the direct and indirect interactions among the different devices along with their possible faulty states. In this context, the availability of a reliable and accurate diagnostic algorithm enables checking and monitoring the system behavior (i.e. *condition monitoring*) as well as inferring on its state of health, also allowing to perform on-board modification of system control laws. Focusing on the diagnosis, to prevent the complete failure of a generic system (e.g. mechanical and electric devices, energy conversion systems, etc.) the most obvious decision is to shut it down whenever an abnormal functioning is observed. Nevertheless, even if this action could seem the most logical one, in many cases it is not the most convenient or even feasible. In these cases the remedial action must be taken while the system is in operation according to the specific time-constrains and the whole repairing costs [24]. Therefore, the capability to detect the occurrence of any faulty state and to identify its causes is a critical task [4], which is strongly related to the design procedure of the diagnostic algorithm. Indeed, the faulty states that can be isolated in the system are only those included in the model and in the inference process [26].

1.1 Model-Based Diagnosis Methodology

Fault detection and isolation (FDI) issues have been investigated since the early 1970s, in parallel with the increase in system automation degree, by reason of the development of cheaper and more reliable

microcomputers, for sensors and actuators production [10]. These studies started from the investigation into several approaches, such as analytical redundancy methods, which are quite different from the traditional physical redundancy ones [31]. Actually, according to these latter, redundant physical devices are equipped on a system to operate in case a fault occurs in regular components, whereas analytical redundancy methods exploit mathematical or signal models to simulate the process behavior. The treatment of the data extracted from the models helps the detection and isolation of the malfunctions, with a few advantages with respect to the physical redundancy methods. On one hand, the use of models allows to avoid using additional equipment, with a consequent reduction in system hardware costs, but, on the other hand, high reliability and accuracy of the models is strongly required.

As stated by many authors, such as Isermann [10], Witczak [11] and Simani et al. [31], the *fault diagnosis* process is generally characterized by three consecutive tasks: i) *fault detection*, through which the presence of a fault is determined; ii) *fault isolation*, which defines the kind of fault and its spatial and time location; iii) *fault identification*, through which the fault size and time-variant behavior are estimated. Within the diagnosis process, the results obtained from each task are strongly dependent on the basis from which the whole procedure has been developed. This basis is clearly defined starting from a deep study of the system itself (e.g. system structure, normal operating conditions, components interactions, etc.) and of the possible faults or malfunctions the system can be affected by.

However, more clarity should be first given upon the differences among the terminology adopted in this field in order to distinguish among the different kinds of abnormal states in which a generic system can run. Many efforts have been made to come to standard definitions, which would be common for different technological areas, as done, for example, through the Reliability, Availability and Maintainability (RAM) Dictionary [32]. Although the terms fault, malfunction and failure are often confused, there is a great difference among them. According to many renowned authors, a *fault* is considered as a deviation of at least one characteristic system property from the normal condition, whereas a *malfunction* is an intermitted irregularity in the desired functionality of the system, while a *failure* is the permanent interruption of system performance [10][11][31]. Thus, the term *fault diagnosis* is defined as the

capability to determine the type, location, time and size of the system unexpected or undesired deviations from acceptable conditions.

To achieve the objectives of the aforementioned tasks, specific features can be extracted from the cross-comparison of data acquired on the system and the ones replicated by the analytical FDI algorithm. The features extraction process can be carried out by means of specific methodologies, e.g. model-based, signal-based or knowledge-based. On one hand, the *model-based* approach exploits a mathematical model (i.e. state-space, multidimensional, lumped, neural network, etc.) for the simulation of the normal behavior of the system and the generation of system variables values at different operating conditions. On the other hand, the *signal-based* approach treats directly the signals acquired on the system to extract the required features, whereas the *knowledge-based* approach is mainly developed starting from the encoding of the heuristic knowledge hold by human experts. These aspects make in some cases the development of both *signal-* and *knowledge-based* algorithms faster than that of the *model-based* ones. However, it is essential to keep in mind that *signal-* and *knowledge-based* approaches require a large amount of complex experiments to be performed also in faulty conditions to correlate either signals or information to the faulty states. From time to time, these experiments could not be performed due to their complexity or the lack of knowledge on the faults to be reproduced. Consequently, experiments feasibility, costs and time issues may limit the development of *signal-* and *knowledge-based* diagnosis algorithms. These drawbacks headed the interest of this research activity towards a *model-based* approach, which, despite its design complexity, shows a greater generalizability as compared with the previous ones, due to its lower reliance on experimental data.

As previously asserted, the *model-based* methodology is grounded on a mathematical model required for the simulation of the system behavior. Therefore, it is possible to deduce that the reliability of the approach is mainly due to the accuracy of the model. Despite the need for a preliminary “a priori knowledge of the system”, the establishment of the model structure can be primarily defined following general physical laws. Moreover, since the model is based on proven physical equations, its validation can be performed with a reduced amount of experimental data in comparison with the other methodologies.

To better understand which model fits better the requirements of a

specific model-based diagnosis application, the description of the main modelling approaches is reported in the following.

Commonly, the most frequent models classification present in the literature consists of three categories, known as *white-box*, *grey-box* and *black-box*. On one hand, *white-box* models (i.e. multi-dimensional, multi-physic, etc.) are based on a deep knowledge of the physical properties and laws which characterize the system under study, and they usually exhibit a great generalizability and require few experimental data for their development and validation. On the other hand, the *black-box* models (e.g. regressions, neural networks, etc.) are less generalizable due to their reduced physical background and require a large amount of experimental data. However, the application of *white-box* models is limited mainly to the design process due to the high computational burden which implies slow computational time, whereas *black-box* models are faster and more suitable for real-time applications, i.e. control, optimization and online diagnosis. Anyhow, a good compromise among the aforementioned models can be found in the *grey-box* ones, which can be considered a trade-off between the accuracy of the *white-box* models and the fast computational time of the *black-box* models. A qualitative representation of the correlation between experimental data and model complexity is given in Figure 1.1 [33]. In this picture two classes of experimental data are taken into account: the training and the test data. The first are exploited to design the model in accordance with the system it should represent, whereas the latter are used for the model validation. As expected, the more complex the model (i.e. physical coherence), the less experimental data are required for the training process. Whereas, the less model complexity, the more both training and test experimental data amount must be exploited.

To overcome the difficulties related to the experimental activity (e.g. high costs and technical limitations), *white-box* models could be used to simulate the real system. In such a case, performing virtual experiments allows to gather a high amount of data with a sensible reduction of time and costs, for both training and test. For diagnosis purposes, such an option may allow to reproduce those operating conditions which might be complicated or even impossible to replicate on a test bench. From the assessments stated above it can be understood that the mathematical model represents the core of the methodology and it must be able to simulate the system in its global behavior. The term global highlights the

capability of the model to take into account both the direct and the indirect correlations among the system components, in order to extract suitable features required by the methodology to perform a correct diagnosis [27]. However, it must be kept in mind that the extraction of specific features is only one part of the whole procedure.

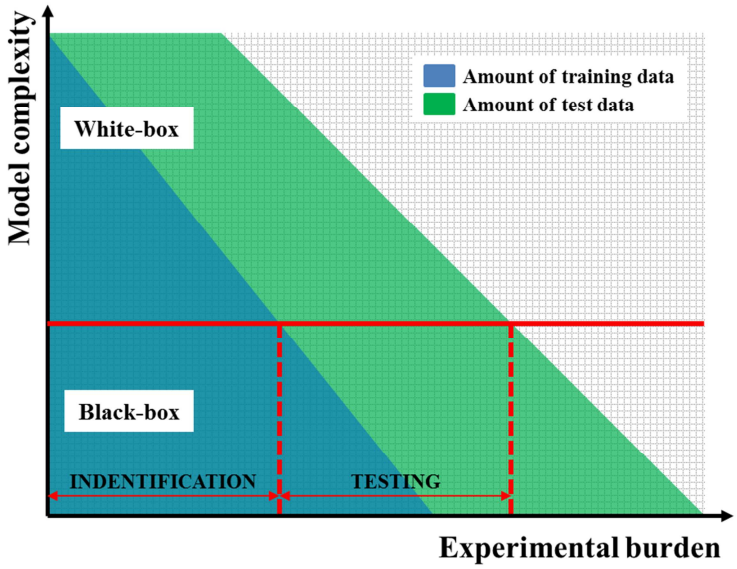

Figure 1.1 Qualitative dependency of required experimental data for training and test procedures on model complexity, adapted from [33].

In the scheme presented in Figure 1.2, all the diagnostic tasks are represented in more details. According to a straightforward approach, the mathematical model can be run in parallel to the real system [9][20], in order to monitor the system and to generate the required features. Referring to the scheme in Figure 1.2, the system input and output variables are expressed respectively as X and Y, and these latter are considered affected by noise N. The output variables measured on the system are compared to those simulated by the model $\hat{Y}$ as function of the input variables X. This comparison leads to the evaluation of the features, which are in this case *residuals*. They are defined as the difference between the variables measured on the system Y and those simulated by the model $\hat{Y}$ [4][9][10][11][17][20][21]:

$$r = Y - \hat{Y} \tag{1.1}$$

Equation (1.1) can be used either if the terms Y and $\hat{Y}$ are scalars or vectors. With the residuals evaluation the *monitoring* task is concluded.

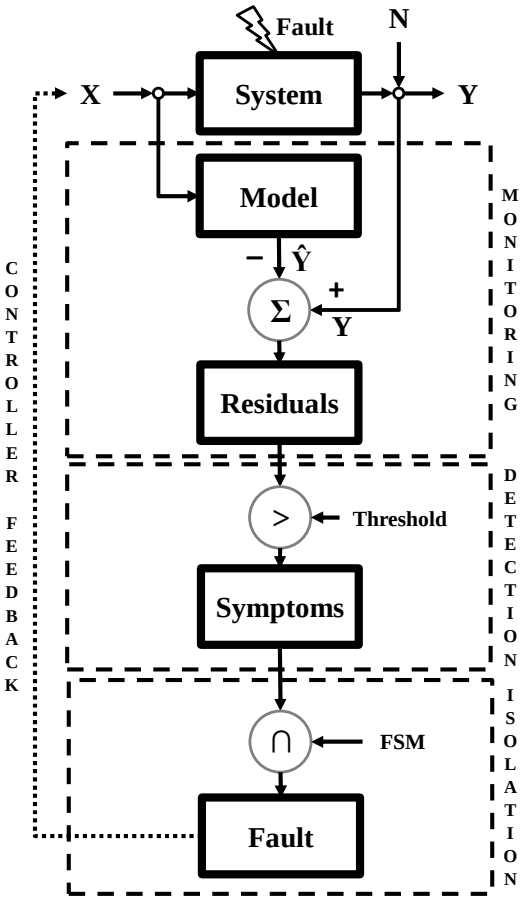

Figure 1.2 Model-based diagnosis scheme, adapted from [10]: X and Y are the control and the measured system variables, respectively, N is the measurement noise and $\hat{Y}$ are the variables simulated by the mathematical model.

Afterwards, the distinction between normal and faulty conditions represents the following task. To achieve this objective, the residuals

values are analyzed. Theoretically, when the system is in normal conditions, any residual should be equal to zero, whereas, in faulty conditions, some of them could diverge from this value. However, due to both the model intrinsic inaccuracy and the measurement uncertainties, residuals can show non-zero values even in normal state. For this reason a tolerance range, characterized by a threshold level τ, is introduced. Considering a scalar value, if the residual falls within the tolerance range, the system behaves normally, however, if the residual overcomes this value, a faulty state is detected.

Translating this qualitative description in a more formal representation, another feature, called *analytical symptom*, can be introduced. Thus, if the residual module is equal or less than the defined threshold level τ, the symptom is 0, otherwise, when the residual exceeds the threshold, it becomes 1, as shown below [17]:

$$s = \begin{cases} 0 & if \quad |r| \le \tau \\ 1 & if \quad |r| > \tau \end{cases} \tag{1.2}$$

When a symptom is active, an undesired (faulty) state is occurring in the system. According to this definition, each monitored variable is simulated through the model and all drifts from normal behavior are collected into a symptoms vector. After the establishment of this vector, the detection process ends with the following status check: if the symptom vector has all 0, the system is working in normal conditions, while, if at least one symptom is 1, an undesired behavior is occurring in the system.

It is worth noticing that the design of proper threshold levels is a very crucial task. These levels must take into account both model inaccuracy and measurement disturbances (i.e. signal noise). For low noise level, a simple threshold value (i.e. a fixed scalar) can be defined, whereas, for high noise level, a more advanced approach (e.g. statistics, fuzzy-logic, Kalman filters, etc.) should be implemented [21][23]. Furthermore, the threshold design process must also satisfy the trade-off between robust diagnosis and early detection [20]. The knowledge of the accuracy and the resolution of all the devices installed on the real system is undoubtedly significant. If the measurement devices exhibit poor resolutions due to, e.g., cheap instruments or low sensitivity, the residuals could always overcome a low threshold, resulting in a continuous faulty state detection.

On the other hand, the thresholds must be set as low as possible to be able to detect incipient faults.

An example of how a symptom arises is given in Figure 1.3. On one hand, the comparison of the residual time behavior *r* with the threshold level *τ'* leads to the generation of the symptom time behavior *S'* (dashed line), in which two faulty states are detected. On the other hand, if the residual is compared to the threshold level *τ"*, the symptom time behavior *S"* (straight line) is shaped, showing only one faulty state. Thus, with the same residual time behavior, two different symptoms patterns can be induced varying the reference threshold level. However, it worth remarking that the first faulty state of the symptom pattern *S'* might not be a faulty state but only a false alarm, induced by measurement errors or other external causes.

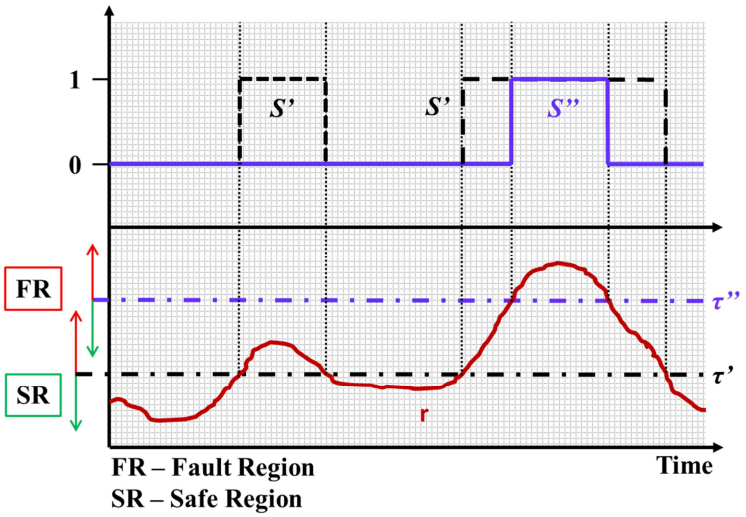

Figure 1.3 Example of symptom time behavior at different threshold levels.

For this reason, another crucial aspect of the threshold design process deals with the capability to distinguish among false alarms and missed faults. Generally speaking, the variables measured on a real system show probabilistic features rather than deterministic ones. As an example, in steady state condition, the measured value of a generic variable might oscillate around its local mean value and can be represented by statistical

indicators [7]. In some cases, the statistical distribution of the values can be represented by a normal probability density function (*pdf*). To perform the diagnosis the measured values can be compared to a set of thresholds. Moreover, in case of probabilistic correlations among the variables, the occurrence of false alarms and missed fault detection should be taken into account. In Figure 1.4 a comparison between deterministic and probabilistic residual evaluation is presented.

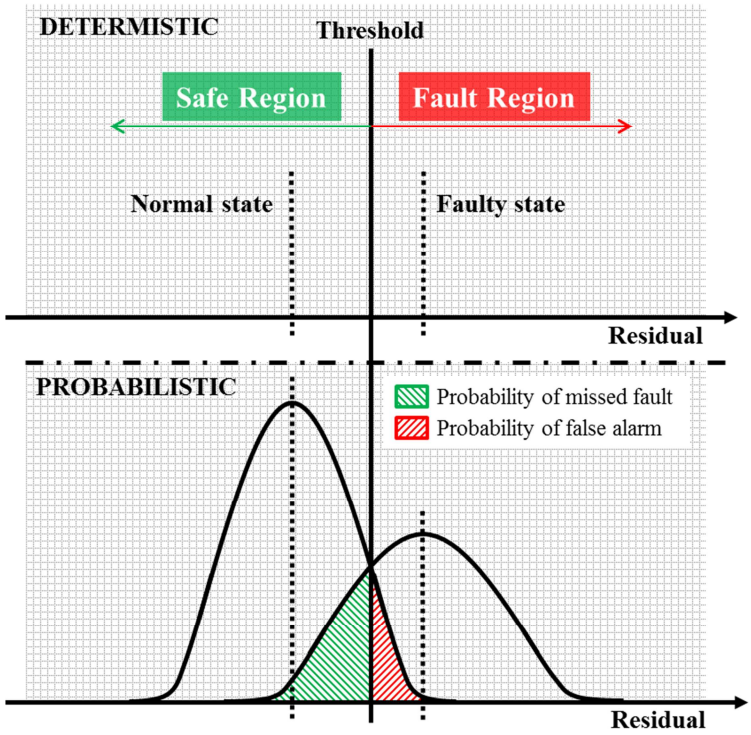

Figure 1.4 Comparison between deterministic (upper) and probabilistic (lower) residual evaluation process for the analytical symptoms generation via threshold setting, adapted from [7][13].

On one hand, in case of deterministic residuals, because no *pdf* is considered either in normal or faulty condition, the probability of missed fault or false alarm cannot be computed. On the other hand, assuming for each residual a stochastic behavior the probabilities of missing a fault or having a false alarm can be defined. The probability of missed fault is

computed by intersecting the *pdf* of the residual in faulty state with the threshold value (green dashed area in Figure 1.4), whereas the probability of false alarm is computed by intersecting the *pdf* of the residual in normal state with the aforementioned threshold (red dashed area in Figure 1.4) [7][13]. These features should be taken into account during both the threshold design process, which clearly affect the symptoms generation, and the diagnostic algorithm application.

Once an abnormal state is detected, in order to identify the location of the malfunction(s) (*isolation process*), the symptoms vector is compared to reference information, which links faults to symptoms. According to Isermann [9], these relations can be determined experimentally by inducing specific faults on the real system. Afterward, the affected variables are singled out to form an *explicit knowledge base*. However, an *a priori knowledge* can be also exploited to find these relationships, avoiding complex experimental activities, which are not always feasible. Indeed, in many cases all the system components are known and the literature provides details on their behavior and interactions. This knowledge significantly helps identifying the correlations among possible faults or failures and their corresponding symptoms. The definition of the causal relationships among faults and symptoms can be performed through different approaches, such as the Fault Tree Analysis (FTA). The FTA is a heuristic methodology which correlates a fault to a set of symptoms. At the end of this process a matrix, known as Fault Signature Matrix (FSM), is built and then used to develop an inferential isolation algorithm. More details about the FTA and the FSM are given in Chapter 3. It is worth noting that the availability of reliable reference information, embedded into the FSM, is mandatory to perform and effective diagnosis. Moreover, an univocal link among the monitored variables deviating from the normal state (i.e. symptoms) and the faults is required. The accuracy of the *isolation process* depends on the knowledge of both the physical behavior of each system component and the possible malfunctions that may occur. Once these references have been defined, the symptoms vector gathered during the *detection process* is compared to this basis (i.e. the FSM) in order to identify the location of the faulty component.

By using the information gathered during the inference process, the controller can act on the system inputs (see Figure 1.2) to drive the system towards safe operating states, if any. Indeed, precise counteractions can be taken to keep the system in a new operating

condition, e.g. to prevent the system shut down if maintenance is needed. As an example, rather than an abrupt shutdown, a suitable controller might slowly drive the SOFC system towards other operating conditions, so as to reduce inefficiency and maintenance costs.

In Figure 1.5 a schematic representation of the global interactions among all the components of a generic system with an embedded diagnostic algorithm is given. From this scheme, it can be evinced that the diagnostic algorithm (*diagnosis*) works in parallel with the controller (*control*) to perform an online – or at least a real-time – inference on the system status.

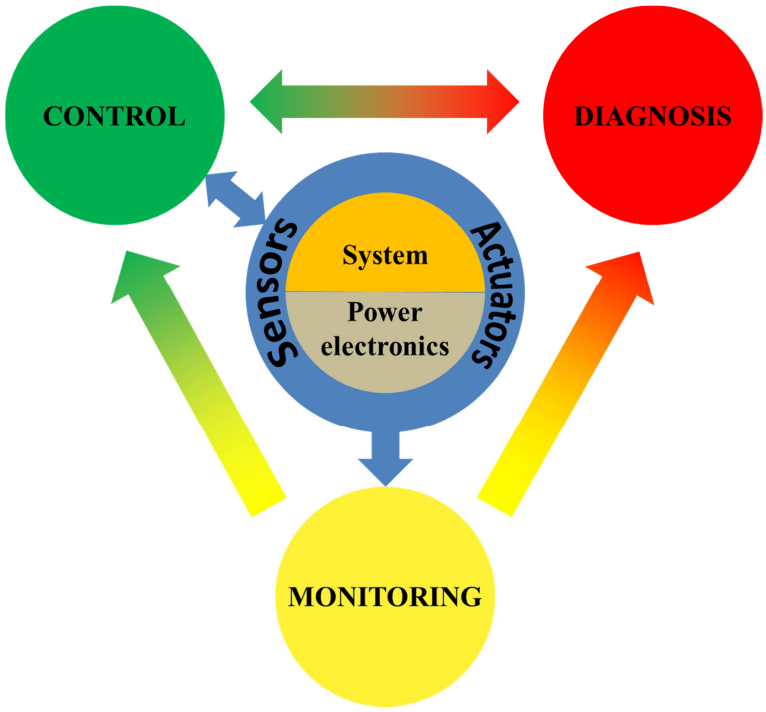

Figure 1.5 Representation of the mutual interactions among all the components of a generic system with an embedded diagnostic algorithm.

The core of the plant is characterized by the system components and the power electronics, whereas the sensors provide the external modules (i.e. *monitoring*, *control* and *diagnosis*) with the required signals. The *monitoring* block receives the signals from the sensors and feeds both the

control and the *diagnosis* blocks, which work in parallel. The *diagnosis* block handles the data, coming up with an inference on the system state. This block communicates with the *control* block providing the location of the faults and the counteractions that should be taken. Finally, the *control* block acts on the system components through the actuators, varying for example the set- points of specific components.

A mutual interaction between the *control* and the *diagnosis* blocks could be also considered: indeed, the knowledge of the control rules chosen for the system supervision must be taken into account during the diagnostic algorithm development, as better explained in the following chapters. The concepts presented so far well highlight the need for a reliable and effective diagnostic methodology able to quickly detect degradation behavior and/or malfunctioning states in the whole system and which can be coupled with an adaptive control strategy able to bring the system to the optimal operation whenever required.

Concerning the studies currently available in the literature, many authors have presented model-based diagnosis approaches and algorithms for several types of conventional systems, such as internal combustion engines [9][20][28], gas turbines [21] and other complex systems [22][23][24][25]. This approach is also widely applied to fuel cells systems, e.g. SOFCs [1][13][16] and Polymer Electrolyte Membrane (PEM) fuel cells [17][18][19]. Furthermore, it is worth remarking that a certain number of models developed for diagnosis purposes are not only developed from physical equations (i.e. mass conservation equations, momentum equations, etc.) but are also based on equivalent circuit elements coupled with electrochemical impedance spectroscopy measurements, such as in [16] and [19].

The present work focuses on Solid Oxide Fuel Cells systems and their main characteristics are presented in the following section.

1.2 Solid Oxide Fuel Cell Systems

A Solid Oxide Fuel Cell (SOFC) is a complete solid-state electrochemical device, which converts the chemical energy of a fuel and an oxidant gas (oxygen) into electrical and thermal power, without being limited by a thermodynamic cycle [5][34][35]. Another significant

advantage of an SOFC (and of all the other fuel cells in general) consists in having zero-pollutants emission when fed with pure hydrogen.

Generally speaking, SOFCs are characterized by a ceramic *electrolyte*, typically Yttria-Stabilized Zirconia (YSZ), which acts as a oxide ions conductor. This element is the most critical one, because it has to ensure high ionic conductivity and electric insulation at the same time. The exploitation of the YSZ as electrolyte material requires high operating temperatures, ranging from 600°C up to 1000°C, to guarantee oxygen ions transport [5]. These high temperatures obviously impose rigorous requirements for the cell materials [35], e.g. the thermal expansion coefficients of all the components should match each other to reduce thermal stresses [42]. The ceramic electrolyte is placed between two porous electrodes: the *anode* and the *cathode*. The most frequently used materials for the anode and cathode structures are a nickel-YSZ cermet and strontium-doped lanthanum manganite $(La_{0.84}Sr_{0.16})MnO_3$ (LSM) respectively [34]. Both anode and cathode materials must satisfy specific requirements, such as high electric conductivity, high catalytic activity (for fuel oxidation – anode – and oxygen reduction – cathode) [5]. The other components that complete the structure of an SOFC cell are the *interconnects* and the *sealing materials*. The interconnects have the main function of electrically connect the single cells and separate the reactant gases within the cell stack (e.g. bipolar plates for planar configurations). Their properties are usually chosen in agreement with the stack configuration, but some basic requirements are common: i) high electronic and thermal conductivities, ii) low ionic conductivity, iii) high mechanical strength, and iv) chemical stability with other components. The material used for the interconnectors structure depends mainly on the operating temperature, e.g. perovskite-type oxide ceramics based on rare earth chromites for temperatures higher than 900°C, or metallic alloys for lower temperatures [5]. Finally, the sealing materials are mainly required for planar SOFC stack configurations, where the challenge of sealing the oxidant from the fuel takes on a significant matter. Usually, glasses having a transition temperature close to the operating temperature of the cell are employed for this purpose [35]. Indeed, during warm up, the temperature rising induces a softening of the materials, which form seals in the required locations [34].

Coming to the description of the basic electrochemical reaction, which is common to all the hydrogen-based fuel cell typologies, what takes

place is the oxidation of the hydrogen, described through the following equation:

$$H_2 + \frac{1}{2}O_2 \rightarrow H_2O \quad (1.3)$$

Particularly, for an SOFC, the hydrogen is initially adsorbed and ionized at the anode side, and the released electrons flow through the external circuit, where a final user (e.g. an electronic load or other devices) draws electric power. The first anode reaction can be expressed as:

$$H_2 \rightarrow 2H^+ + 2e^- \quad (1.4)$$

On the other hand, the oxygen atoms are adsorbed at the cathode side and ionized by the electrons coming from the external circuit:

$$\frac{1}{2}O_2 + 2e^- \rightarrow O^{2-} \quad (1.5)$$

Then, the oxide ions flow through the electrolyte, reaching the anode side and reacting with the hydrogen ions, with consequent generation of water molecules:

$$2H^+ + O^{2-} \rightarrow H_2O \quad (1.6)$$

If the SOFC is fed with hydrogen-rich fuel (i.e. methane) instead of pure hydrogen, reforming reactions occur at anode side. The *oxygenolisis reactions* (see equation (1.7), referred to methane) and the associated water gas shift (WGS) reaction (equation (1.8)) normally take place over a supported nickel catalyst [34]. The global reactions are expressed as:

$$CH_4 + H_2O \rightarrow CO + 3H_2 \quad (1.7)$$

$$CO + H_2O \rightarrow CO_2 + H_2 \quad (1.8)$$

The main issue with the direct use of methane or other hydrocarbons is the risk of coke formation, which blocks and contaminates the anode [5].

Generally, two main SOFC designs can be found in the literature, known as planar and tubular design. The first one is characterized by square plates fed from the edges, or even circular discs, fed with fuel from the central axis. Two further classifications for the planar design can be done according to the gas flow configuration and the support type. On one hand, the gas flow configuration could be either co-flow or counter-flow, or even cross-flow [5]. On the other hand, the support type could be self-supporting, where one of the cell components serves as cell support (i.e. electrolyte-supported, anode-supported or cathode-supported), or external-supporting, where the cell is manufactured as a thin layer leant on the interconnect or on a porous substrate [5].

A detailed scheme of the structure of a planar anode supported SOFC, directly fed with methane at anode side, is given in Figure 1.6. Three close-ups offer an insight into the electrochemical reactions previously described. The first close-up (a) refers to the oxygen reduction reaction occurring at cathode side, expressed by equation (1.5). The second close-up (b) is located at the anode side, focusing on the hydrogen ions formation – equation (1.4) – and the water generation – equation (1.6). The last close-up (c) refers to the reforming reactions expressed by equations (1.7) and (1.8).

It is worth observing that the scheme represented in Figure 1.6 refers to a square design, whereas in Figure 1.7 an example of an SOFC with circular design is presented. About tubular designs, whose schematic representation is given in Figure 1.8, their classification can be done according to their diameter size, i.e. large diameter cells, if the diameter length is higher than 15 mm, or microtubular cells, if the diameter length is lower than 5 mm [5].

To provide the required amount of power output, single cells can be electrically connected to each other, in a so called *stack* design. However, it is important to remark that an SOFC stack cannot operate without a dedicated balance of plant (BOP). The BOP typically includes fuel processor, heat exchanger, thermal insulations, blowers, pipes, power conditioning and control system. The main moving parts in this plant are the blowers, together with a fuel pump, if pressurized fuel is not supplied [5].

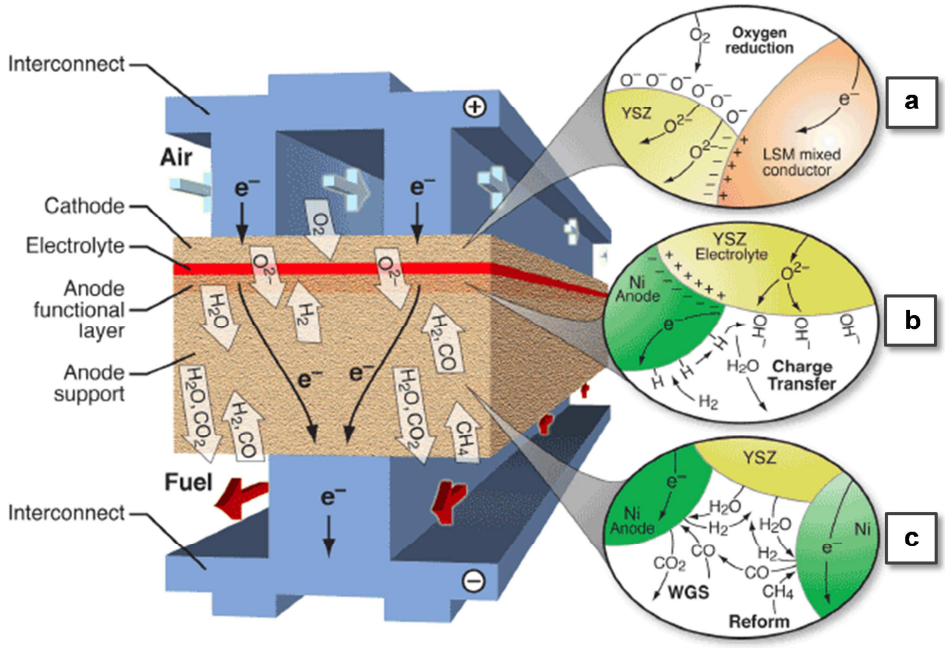

Figure 1.6 Detailed scheme of an anode supported Solid Oxide Fuel Cell directly fed with methane, adapted from [36].

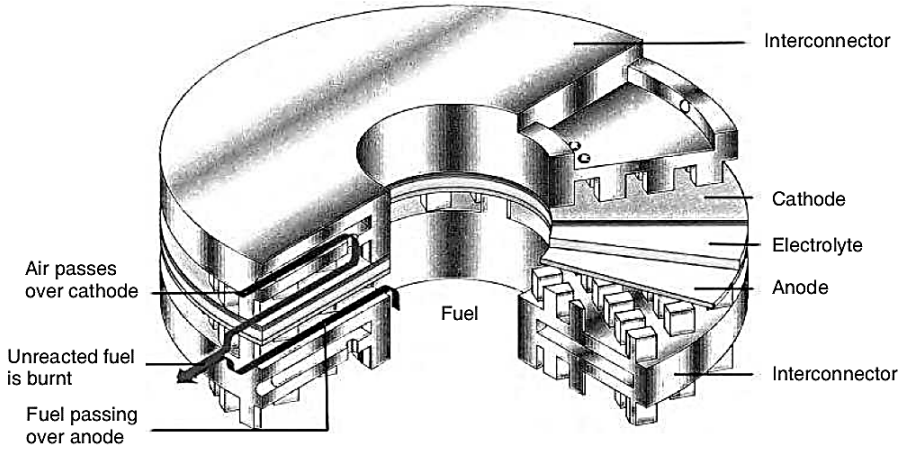

Figure 1.7 Planar SOFC with circular design [34].

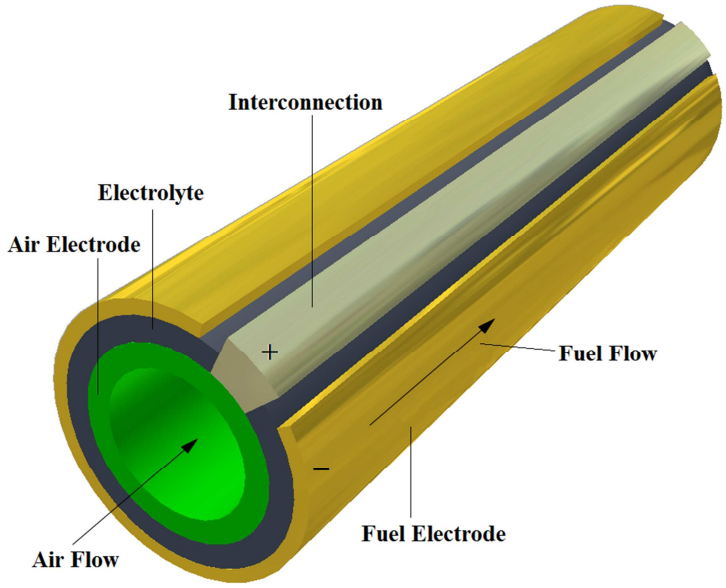

Figure 1.8 Schematic representation of a tubular SOFC design, adapted from [5] and [37].

Clearly, the SOFC design must be chosen according to its application. It is worth noting that the high temperatures, at which an SOFC usually works, induce two main binding features, i.e. slow dynamic response and high temperature byproduct heat [33]. The former feature makes SOFCs less appealing for automotive applications, characterized by high fluctuations of power demand. On the contrary, the latter feature drives SOFCs towards stationary applications, such as distributed power generation systems, cogeneration (Combined Heat and Power – CHP) plants and Auxiliary Power Units (APUs). These applications often exploit the SOFC stack in combination with other power generation system, e.g. internal combustion engines or gas turbine, as done by Siemens Westinghouse [5][34][38]. Nevertheless, despite showing slow dynamic responses, the advantage given by their high fuel flexibility, along with the absence of water management issues, allows SOFCs exploitation as APUs even for automotive applications, in order to match the power demand of the auxiliary components and extend the vehicle range [64].

Actually, the exploitation of SOFCs for automotive applications already exists since years, however not for power generation purposes.

Indeed, the capability of the YSZ to easily detect oxygen allows its application as oxygen sensor device in the exhaust manifold on traditional internal combustion engines (λ sensor). To guarantee the optimal operation of the exhaust catalyst, the oxygen sensor measurements are exploited to keep the exhaust gas mixture near the stoichiometric ratio [5].

1.3 Motivations, objectives and contributions

As previously stated, to increase reliability and lifetime of SOFC systems, suitable adaptive control strategies, ensuring optimal operating conditions at any power request level, should be designed. The shift from one operating point to another, especially for stationary systems designed to work at fixed operating conditions, or the occurrence of any unexpected event may accelerate the system degradation or induce other phenomena, which can lead to system fault, or worse, to system failure.

Starting from these concepts, the present work illustrates the complete procedure of developing a model-based diagnosis algorithm and shows its application to a pre-commercial SOFC system. Firstly, a brief overview on the state of the art available in the literature concerning modeling and diagnosis on SOFC systems is given in the following.

1.3.1 State of the art

The research efforts concerning SOFC diagnosis are mainly oriented towards the understanding of the degradation mechanisms and malfunctions which affect the cell components and the whole stack. Generally speaking, the stack performance can be affected by different mechanisms, which involve single components or induce mutual effects, such as electrode delamination, thermo-chemical and thermo-mechanical phenomena and electrode poisoning, just to mention a few. However, due to the equivalence of their effect on the stack performance, it is not possible to univocally identify a specific mechanism only through the

analysis of the output voltage at constant current, requiring more advanced diagnostic techniques [44]. For this reason, Barelli et al. [44] analyzed the different degradation mechanisms which can affect SOFCs and the diagnostic methodologies currently available in literature for their detection. To better describe stack degradation phenomena, Virkar [45] developed an SOFC stack model capable of simulating degradation induced by the increase of the resistance of an isolated cell (or few cells). As stated by this author, some causes leading to this phenomenon could be: i) formation of local hot spots, which can induce the modification of material properties and microstructures, ii) fuel or oxidant non-uniform distribution, iii) seals degradation or iv) electrode delamination induced by thermal cycling. Virkar [45] also highlights the need for estimating how long the cell requires to cause a stack failure since the deviation sets in. To the same purpose, Larrain et al. [46] developed an SOFC repeat element model for the investigation of stack degradation due to interconnect degradation and anode reoxidation potential. In the work carried out by Gemmen and Johnson [47] the attention is focused on the correlation between SOFC system efficiency and degradation, with a major concern about the role played by the auxiliaries.

Aside the last cited and other few available works, a deeper study on the influence of all the SOFC system components (i.e. stack and BOP) on the system behavior during normal and faulty condition is lacking in the current literature. Besides, a limited number of authors developed mathematical models to simulate systems malfunctions, faults or failures [17][58], and few works coupled this activity with a focused experimental activity, where controlled fault are induced on the system under study [59].

Concerning SOFC stack and system modeling, in the available literature, many papers deal with this topic, ranging from 3-D (e.g. white box) models to 0-D (e.g. black box) models in accordance with design, the former, or control, the latter, purposes [39]. As an example, Kakaç et al. [40] presented a detailed overview of the status of SOFC models, classifying them in two main categories, i.e. micro-models, in which the micro-scale behavior is described, and macro-models, in which the overall system behavior is considered. In Bove and Ubertini's work [41], an SOFC model is presented, taking into account different approaches, from 3-D to 0-D, and validating each model against experimental data. Faghri et Guo [42] gave a brief overview on the models and operations of

low temperature and high temperature fuel cells, referring to thermal management issues and materials requirements. Particularly for SOFCs, they highlight the importance of cell and system design with attention to materials compatibility and components interaction, in order to understand the optimal operating conditions for high efficiency and long-term operation. The SOFC thermal management issue has also been addressed by Tsikonis [43], who developed a dynamic model of an SOFC HotBox^{TM} commercialized by HTceramix and SOFCpower. In their works, Sorrentino et al. proposed a 1-D model [3][33] and a lumped model [1][2] of a planar SOFC, in order to design a hierarchical structure for the definition of low-level control strategies for transient operations.

1.3.2 Motivations and objectives

In the last decade, the researchers attention have become more sensible towards the aforementioned topics, increasing their efforts so as to accelerate the improvements on fuel cells and hydrogen technologies, especially for market introduction. An example of this effort is the Fuel Cells and Hydrogen Joint Undertaking (FCH JU), an European partnership between public and private stakeholders aimed at supporting research, technological development and demonstration (RTD) activities oriented towards fuel cells and hydrogen technologies [48]. By means of this partnership many projects were founded from 2008 through 2013 on several research topics, e.g. long-term, breakthrough-oriented and pre-normative. Despite the variety of the application scopes, some projects focused on fuel cell diagnosis, such as GENIUS (*Generic diagnosis instrument for SOFC systems*) [49] and DESIGN (*Degradation signature identification for stack operation diagnostic*) [50], concerning SOFCs, and D-CODE (*DC/DC converter-based diagnostics for PEM systems*) [51], concerning polymer electrolyte membrane (PEM) fuel cells.

The work described in the present dissertation focuses on the objectives evaluated by the GENIUS project, within whose framework part of the diagnostic methodology, the algorithm and its application have been carried out. The scope of the GENIUS project entails the development of a “generic” diagnostic algorithm for SOFC systems, which exploits process values to perform system diagnosis both offline

and online. The main targets of the project are to ensure maintenance reduction to yearly intervals and to help SOFC system lifetime to increase towards market requirements (e.g. 40,000 h) [49]. The novelty of the proposal resides in two main aspects: on one hand, the direct exploitation of the stack and the auxiliary components as sensors could overcome the constraints of current methodologies (e.g. absence of anticipation and low accuracy) and reduce system complexity (i.e. no use of further specific sensors); on the other hand, the term "generic" refers to the flexibility of the diagnostic methodology to be applied to different SOFC systems.

The main objective of this work is the definition and the application of a detailed procedure to develop a model-based diagnostic algorithm for online diagnosis. The description of this procedure explains in detail the steps that should be followed and draws the attention on the problems that can come up and what are the possible ways to solve them. The diagnostic algorithm development and application procedure entails two phases: i) an offline design phase and ii) an on-line application phase, as showed in Figure 1.9, where a scheme of the procedure is given.

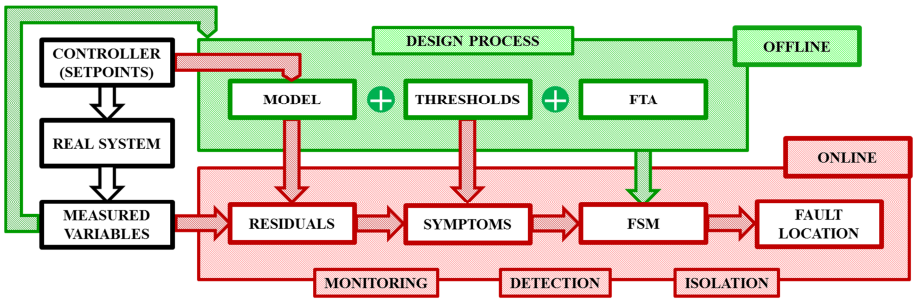

Figure 1.9 Development and application procedure scheme of a model-based diagnosis algorithm.

The offline design phase involves the development of the mathematical model, the reference thresholds and the FSM, whereas the online application phase involves the application of the complete algorithm on the real system, once a communication protocol between the system and the algorithm is defined. Focusing on the design phase, as previously stated, a model-based approach has been chosen as reference methodology for the algorithm development. According to what expressed in paragraph 1.2, the diagnostic algorithm is characterized by

three main elements: i) a mathematical model, which can simulate the system behavior at several operating conditions, allowing residuals calculation (*monitoring*), ii) specific threshold levels, required for the generation of analytical symptoms from the residuals (*detection*) and iii) an inferential isolation tool, i.e. an FSM developed from an FTA, which helps locating the faults in the system.

It is worth highlighting that the methodology here described can be considered generic, since it lists all the steps to be followed for the development of a complete model-based diagnosis algorithm, apart from the system the algorithm is related to. However, the development of the algorithm elements requires the knowledge of the specific monitored system, i.e. the number and type of components, the available measured variables, the controller strategies, the faults which can occur in the system, etc.

Clearly, to perform the design process a certain amount of experimental data, both in normal and faulty state, is required. These data are mandatory for the development of the model and the definition of missed faults and false alarm probabilities. Furthermore, as further explained in Chapter 3, the mathematical model can be also used, coupled with specific threshold levels, during the off line process to help developing the FSM.

A “standard” FSM developed following a FTA approach offers only a qualitative relationship among faults and symptoms without taking into account all the direct and indirect correlations among the system components. These correlations could be enhanced using a mathematical model able to simulate the system in both normal and faulty states. By means of this simulation process it is possible to evaluate the drift of the monitored variables from their normal behavior, and, comparing the obtained residuals with different threshold levels, the sensitivity of the system to faults magnitude can be also examined, improving the reliability of the developed FSM.

Once the offline design process is completed, the diagnostic algorithm can be built and applied to the monitored system, to perform an online fault diagnosis. Clearly, to ensure the correct operation of the diagnostic algorithm, a communication protocol between the algorithm and the real system must be defined.

1.3.3 Expected contributions of the research

The novelty of this work and its main contributions reside in four features:

1) the development of fault sub-models, implemented into a pre-existing SOFC system model:
2) the exploitation of faulty states simulation for the development of an FSM, evaluating the sensitivity of the monitored variables to the faults magnitude;
3) the design of specific procedures and hardware modifications to mimic faults in a controlled way on a real SOFC system;
4) the offline and the online validation of the proposed algorithm.

The procedures presented in this thesis have been designed within the framework of the GENIUS project to test the diagnostic algorithm on an SOFC μ-CHP system, the Galielo 1000N, manufactured by the Swiss company HEXIS AG (one of the industrial partners of the GENIUS project) [52]. The experimental activity accomplished with this system has been performed in a close collaboration among the University of Salerno, the European Institute for Energy Research (EIFER) and the HEXIS AG company. The experiments have been carried out at the EIFER laboratories in the frame of an exchange student program between the University of Salerno and EIFER. The results of this experimental activity and the on-line application of the diagnostic algorithm described in this work have already been presented during the 5th Fundamentals & Development of Fuel Cells (FDFC) Conference – 16th-18th April 2013, Karlsruhe, Germany – and for further details the readers are addressed to the corresponding references [53][54].

1.4 Thesis outline

This dissertation is organised into seven chapters. After the current introductive chapter, Chapter 2 gives a theoretical explanation of the mathematical SOFC system model, derived from a prior model developed

by Sorrentino et al. [1][2][3], with the definition of the main equations and the description of the faults sub-models developed within this work. In Chapter 3, the bases of the FTA approach are briefly discussed. Then, the improvement of a former FSM, developed by Arsie et al. [4], is presented. This improvement has been obtained by means of faulty state simulations with the developed model. In this way, the limitations of adopting a purely heuristic approach to develop an isolation tool are clarified. Chapter 4 presents the experimental activity performed on the Galileo 1000N in order to mimic controlled faulty states on a real system. In Chapter 5, first the characterization of the diagnostic algorithm on the Galileo 1000N system is described, focusing on the communication protocol between the algorithm and the system and on the tuning procedure of all the algorithm elements. Then, the results of the algorithm validation are presented and discussed. Finally the conclusions are drawn in Chapter 6, whereas the Chapter 7 gives a brief insight into the additional experimental activity performed on the Galileo 1000N system within the GENIUS project framework.

CHAPTER 2 SOFC System Model

In this chapter a dynamic model of a methane-fueled SOFC system, able to reproduce both normal operations and faulty states, is presented. This model has been derived from an SOFC-APU lumped model previously developed by Sorrentino et al. [1][2][3].

As a rule, an SOFC system is usually designed in such a way as to ensure normal stack operation through a proper configuration and optimized control of the auxiliary components. As a result, the behavior of the whole system does not depend only on the stack performance but also on the behavior of the BOP, which is prone to malfunctions and failures due to the large number of mechanical and electronic components.

A block diagram of a methane-fueled SOFC system is presented in Figure 2.1, where both the mass and the energy flows are represented [2][5]. It is worth noting that this scheme reproduces a generic SOFC system, whose application is suitable for a μ-CHP system as well. The whole system, enclosed in a dashed frame, is supplied with air and fuel from an external line and provides electric energy and useful heat to the final user.

The fuel (i.e. methane – in this case – or any other hydrogen-reach fuel) flows through a steam pre-reformer to produce hydrogen via partial reforming reactions (see equations (1.7) and (1.8)), which require a specific amount of water and heat. The former can be provided by an external line (e.g. a water tank joint with a controlled pump), whereas the latter is recovered from the post-burner exhaust gases. At the air side, an air blower supplies the system with the necessary amount of air, which flows through an air pre-heater to reach the required inlet set-point temperature.

Once both the fuel and the air flows reach the SOFC stack, the electrochemical reactions (see equations (1.4) to (1.6)) take place and the electric energy demand is fulfilled. However, before reaching the final user, power conditioning devices are usually needed to convert the stack

DC power to AC power and to boost the voltage (power electronics block). Sometimes, in APUs a battery pack is also associated to supply electric energy during warm-up maneuvers or peak power phases, in order to reduce the risk of thermal stresses, and to store energy during low power demand periods [2].

The gases leaving the stack are burned into a post-burner to increase the temperature of the exhausts. The hot gases are sent to the fuel pre-reformer, to control the reaction temperature by means of a heat exchange process. Then they flow through a heat exchanger, to heat up the fresh air provided by the blower. The residual heat could be finally recovered for co-generation uses.

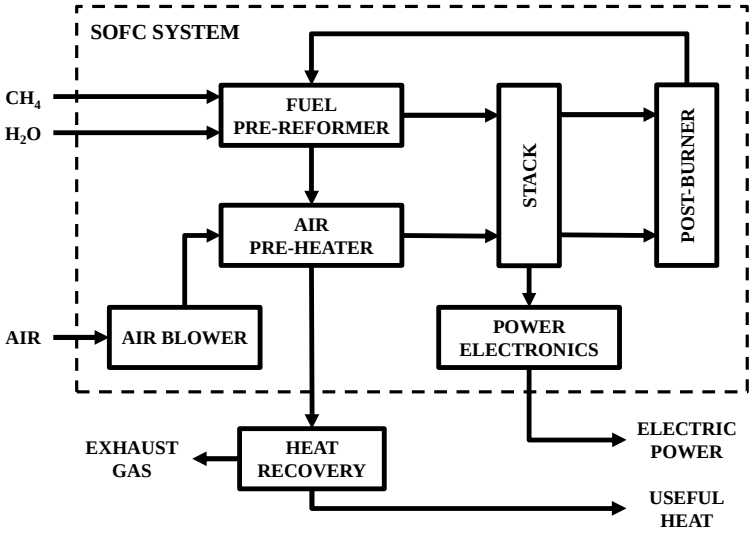

Figure 2.1 Block diagram of a methane-fueled SOFC system with mass and energy paths, adapted from [2] and [5].

Taking the block diagram presented in Figure 2.1 as a reference, in this work both the static and dynamic behaviors of all the aforementioned elements are simulated, but power electronics and heat recovery are not modeled. Moreover, with respect to the model developed by Sorrentino et al. [1][2][3], the present model includes the simulation of gas flow through the intake manifolds, both at air and fuel side, and several sub-models representing specific faulty states, which can affect the stack and the BOP components.

In the next paragraphs, a detailed description of the main physical equations representing normal and faulty behaviors of the SOFC components is given. As already mentioned, the basic equations have been retrieved from the reference papers of Sorrentino et al. [1][2][3].

2.1 Methane-fueled SOFC system model

A detailed scheme of the SOFC system components modeled in the present work is given in Figure 2.2. It is worth observing that two pipes are present at the air side, one linking the blower to the pre-heater and one located between the pre-heater and the stack. On the other hand, at the fuel side one pipe connects the pre-reformer and the stack. Following the same approach of Sorrentino et al. [1][2], the thermal management of the system is fulfilled by means of two by-pass valves, one at the pre-reformer side ($V_{pre\text{-}reformer}$) and one at the pre-heater side ($V_{pre\text{-}heater}$).

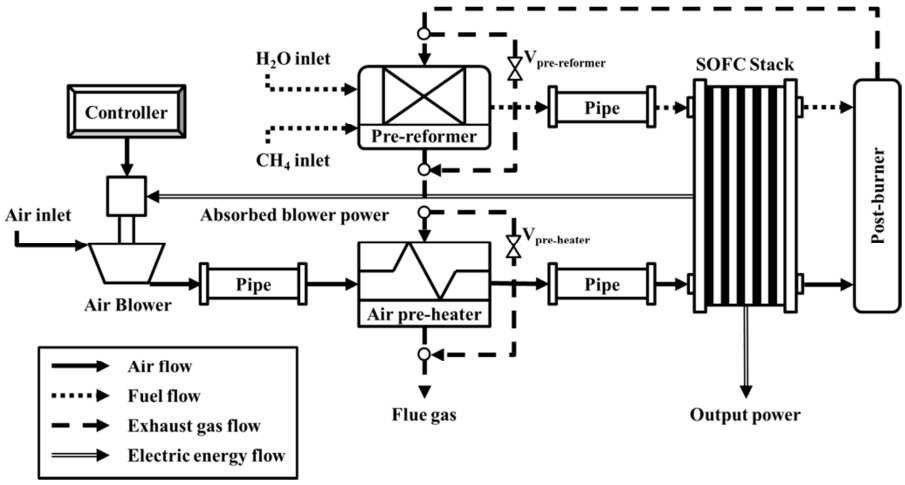

Figure 2.2 Plant scheme of the SOFC system model with the representation of the energy and mass flows. Compared to the one presented by Sorrentino et al. [1][2], three pipes have been added.

These valves are controlled in feed-forward mode, exploiting look-up tables function of the required current. Moreover, a proportional-integral

(PI) controller, designed in feedback mode, acts on the blower speed to ensure the required amount of air mass flow in order to keep the stack temperature near the set-point value.

The specifications of the SOFC system and the assumptions made for the development of the model are listed below:

- the stack is planar and co-flow;
- single cell performance is assumed extendable to the whole stack;
- a lumped model approach is applied: each component is represented by a specific lumped volume in which the spatial variations are neglected;
- electrochemical reactions and mass transfer are assumed instantaneous;
- all the components are considered adiabatic (i.e. no heat exchange with the surroundings);
- the WGS reaction is considered at equilibrium;
- The methane is assumed completely reformed before leaving the stack;

To better distinguish between normal and faulty states, a dynamic model is required. Indeed, with a steady-state model any deviation from a stationary condition might be interpreted either as a transient maneuver or as a deviation from a safe condition. An example of such a case is given in Figure 2.3. In this picture a transient maneuver from one operating condition to another is sketched. Initially, the monitored signal, represented by a straight line, lies within the reference threshold range related to the first operating condition, represented by two dashed lines. Once the transient maneuver starts, the signal diverges from the previous operating condition, leaving the related threshold range at *t'* and entering the second one, represented by two dot-dashed lines, at *t"*. Between this two moments, since no dynamic model is defined, the transient maneuver might be interpreted as an unexpected event. Therefore, to avoid the risk of misunderstanding, the use of a dynamic model is necessary [27]. An example of transient maneuver performed on a real system can be found in Chapter 7, where the description of experimental data measured on the Galileo 1000N system is given.

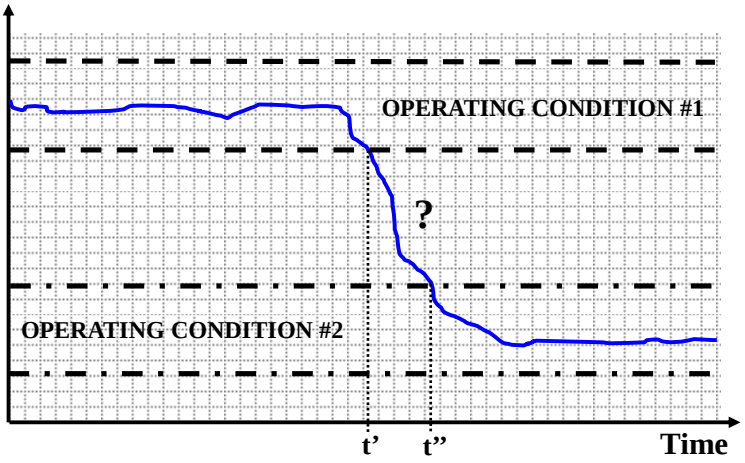

Figure 2.3 Example of transient maneuver not distinguishable from a faulty event with a diagnostic algorithm based on a steady-state model.

In the specific, paragraph 7.3.1 details the transient procedure followed to bring the system from one operating condition to another. In this case, the availability of a suitable dynamic model allows the right interpretation of such maneuver as an expected change in the operating condition rather than a faulty state.

2.1.1 SOFC stack

In accordance with the approach presented by Sorrentino et al. [1][2], the SOFC stack is modeled as a single control volume exchanging mass and energy with the surroundings. Applying the energy conservation equation to this volume, the following lumped capacity model equation can be derived:

$$K_{SOFC}\frac{dT_{SOFC,out}}{dt} = \dot{E}_{SOFC,in}\left(T_{SOFC,in}\right) - \dot{E}_{SOFC,out}\left(T_{SOFC,out}\right) + - JA_{SOFC}V_{SOFC} \qquad (2.1)$$

where $T_{SOFC,out}$ is the temperature at the stack outlet, K_{SOFC} is the stack

heat capacity, $T_{SOFC,in}$ is the temperature at the stack inlet, $\dot{E}_{SOFC,in}(T_{SOFC,in})$ and $\dot{E}_{SOFC,out}(T_{SOFC,out})$ are the inlet and outlet energy rates respectively (depending on the stack temperatures), J is the stack current density, A_{SOFC} is the electro-active area and V_{SOFC} is the stack voltage, evaluated through the following regression [2]:

$$V_{SOFC} = n_{cells}\left(0.1844 - 0.0819U_f - 1.2352J - 0.0041\lambda\frac{T_{SOFC,out}}{1000} + \right. \\ \left. + 0.8594J\frac{T_{SOFC,out}}{1000} + 0.7153\frac{T_{SOFC,in}}{1000}\right) \tag{2.2}$$

where n_{cells} is the number of cells, U_f is the fuel utilization and λ is the excess of air. The inlet and outlet energy rates are computed as follows:

$$\dot{E}_{SOFC,k} = \sum_i \dot{n}_{i,k} h_i\left(T_{SOFC,k}\right) \\ i = [H_2, H_2O, CH_4, CO, CO_2, O_2, N_2] \quad k = [in, out] \tag{2.3}$$

In equation (2.3), the enthalpy of each species is computed as function of the stack temperature [2]. Furthermore, the inlet molar flows derives from the operating behavior of the BOP components (as described in the following), whereas the outlet flows are evaluated as function of current and temperature and their composition is consistent with the WGS reaction equilibrium assumption [2]. Finally, the stack heat capacity is computed with the following expression:

$$K_{SOFC} = \rho_{cer} c_{cer} VOL_{SOFC} \tag{2.4}$$

in which the term VOL_{SOFC} represents the volume of the solid parts (i.e. electrolyte, electrodes and interconnections), ρ_{cer} is the ceramic density (6600 kg m^{-3}) and c_{cer} is the ceramic specific heat (400 J kg^{-1} K^{-1}). The evaluation of the stack heat capacity through equation (2.4) is motivated by the simplifying assumptions made for the development of the model (i.e. neglecting the gases heat capacity) and by the limited availability in the literature of experimental data for its direct identification [2].

2.1.2 Air blower

The air blower represents the main moving part of the entire SOFC system and it can be considered the most energy consuming device [4]. Its main function is to provide the stack with the necessary amount of air, in order to guarantee the electrochemical reaction to take place and to ensure the stack cooling. The processed air mass flow is computed as function of current density J and excess of air λ as follows [2]:

$$\dot{m}_{AIR} = \lambda \frac{JA_{SOFC}}{4F} \frac{M_{O_2}}{0.233} n_{cells} \tag{2.5}$$

where F is the Faraday constant (96,487 C mol^{-1}) and M_{O_2} is the oxygen molar mass. The temperature at the blower outlet is evaluated as a function of the temperature at the blower inlet, the blower efficiency and the pressure ratio:

$$T_{B,out} = T_{AIR,in}\left[1 + \frac{1}{\eta_B}\left(\beta^{\frac{\gamma-1}{\gamma}} - 1\right)\right] \tag{2.6}$$

The required power is evaluated as:

$$P_B = \dot{m}_{AIR} \frac{c_{p,AIR} T_{AIR,in}}{\eta_B \eta_{EM}}\left(\beta^{\frac{\gamma-1}{\gamma}} - 1\right) \tag{2.7}$$

in which β is the pressure ratio, $T_{AIR,in}$ is the temperature at the blower inlet, $c_{p,AIR}$ is the air specific heat at constant pressure, γ is the polytropic coefficient, η_{EM} and η_B are the electric motor efficiency and the blower efficiency respectively. For the purpose of the diagnostic algorithm design, a volumetric blower has been considered, whose efficiency and speed are evaluated through the maps represented in Figure 2.4 and Figure 2.5, respectively [55]. The efficiency is estimated through the efficiency map presented in Figure 2.4 function of the electric motor speed and the blower pressure ratio.

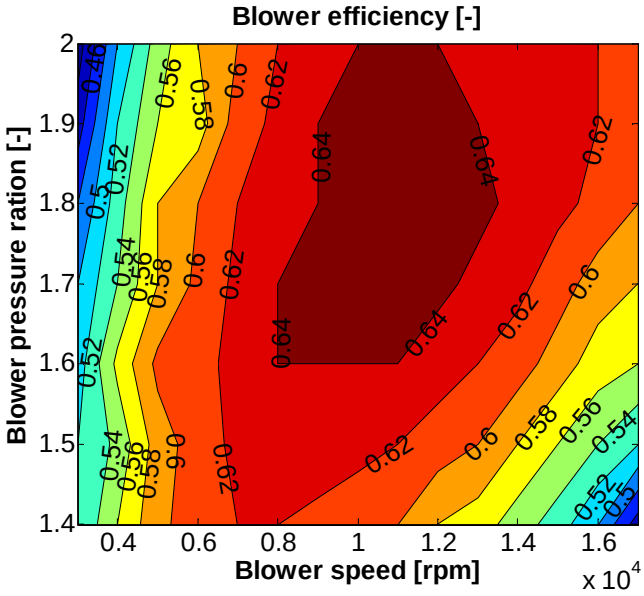

Figure 2.4 Blower efficiency map [55].

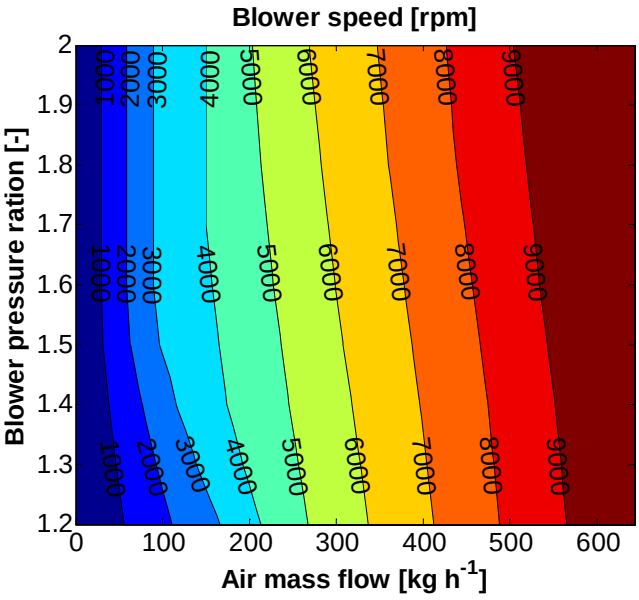

Figure 2.5 Feed-forward blower speed map [55].

Moreover, the speed of the electric motor is evaluated trough a feed-forward control map, in which the speed depends on the required air flow, evaluated through equation (2.5) and the blower pressure ratio.

As a final point, since the blower can be considered the main parasitic loss [2], the whole ancillary power request is represented by its absorbed electric power, and the evaluation of the net output power can be performed as follows:

$$P_{NET} = V_{SOFC} JA_{SOFC} - P_B \tag{2.8}$$

through which the whole SOFC efficiency can be calculated:

$$\eta_{NET} = \frac{P_{NET}}{\dot{m}_{CH_4} HHV} \tag{2.9}$$

The denominator of equation (2.9) represents the inlet fuel power evaluated considering the inlet methane mass flow $\dot{m}_{CH_4}$ and its higher heating value (HHV).

2.1.3 Air pre-heater

Following the Zero-Capacity Approach (ZCA), presented by Ataer et al. [29] and exploited by Sorrentino et al. [1][2], the air pre-heater is modeled assuming a cross-flow configuration. The energy balances for the hot fluid and cold fluid sides lead to equation (2.10) and equation (2.11) respectively, in which the hot fluid is the pre-reformer hot exhaust, whereas the cold fluid is the cathode inlet flow:

$$\begin{aligned}\left(K_{HE} + C_{h,HE}\right)\frac{dT_{h,HE}}{dt} = \dot{E}_{h,HE,in}\left(T_{h,HE,in}\right) - \dot{E}_{h,HE,out}\left(T_{h,HE,out}\right) + \\ - U_{HE} A_{HE}\left(T_{h,HE} - T_{c,HE}\right)\end{aligned} \tag{2.10}$$

$$C_{c,HE}\frac{dT_{c,HE}}{dt} = \dot{E}_{c,HE,in}\left(T_{c,HE,in}\right) - \dot{E}_{c,HE,out}\left(T_{c,HE,out}\right) + \\ + U_{HE}A_{HE}\left(T_{h,HE} - T_{c,HE}\right) \tag{2.11}$$

In these equations, the terms $T_{h,HE}$ and $T_{c,HE}$ represent the average hot and cold temperatures respectively, evaluated as the arithmetic average of the inlet and outlet temperatures of the two fluids:

$$T_{k,HE} = \frac{T_{k,HE,in} + T_{k,HE,out}}{2} \quad k = [h,c] \tag{2.12}$$

Differently from the work of Sorrentino et al. [2], the gas heat capacities of both hot and cold fluids are considered in addition to the solid heat capacity for the evaluation of the heat exchanger dynamic response. The energy flow terms are evaluated considering the mathematical product between the fluid heat capacity and the related temperature, whereas the last term of both the equations represents the heat flow exchanged between the hot and cold fluids. It is worth observing that equations (2.10) and (2.11) represent a system of coupled ordinary differential equations. The behaviors of both the hot and cold temperatures affect one another through the exchanged heat flow term.

Following what done by Sorrentino et al. [2], the product between the heat transfer coefficient U_{HE} and the heat exchange surface A_{HE} has been identified as a function of the fluid heat capacities and exchanger efficiency (i.e. estimated inlet and outlet temperatures) by means of the Kays and London efficiency maps [56]. Furthermore, the solid heat capacity K_{HE} is also evaluated through equation (2.4), appraising the heat exchanger volume through a surface to volume ratio of 2500 m^{-1}, once the exchange surface is defined considering as reference a gas to gas heat exchange coefficient of 200 W m^{-2} K^{-1} [2].

Finally, the outlet temperatures are regulated exploiting a by-pass valve ($V_{pre\text{-}heater}$ in Figure 2.2), to guarantee the stack thermal set-points and proper temperatures at the stack inlet [1]. This valve is controlled in feed-forward mode through a look-up table function of the SOFC stack current density, as shown in Figure 2.6. Observing the plant scheme in Figure 2.2, this valve directly regulates the hot fluid flow coming from

the fuel pre-reformer and passing through the air heat exchanger.

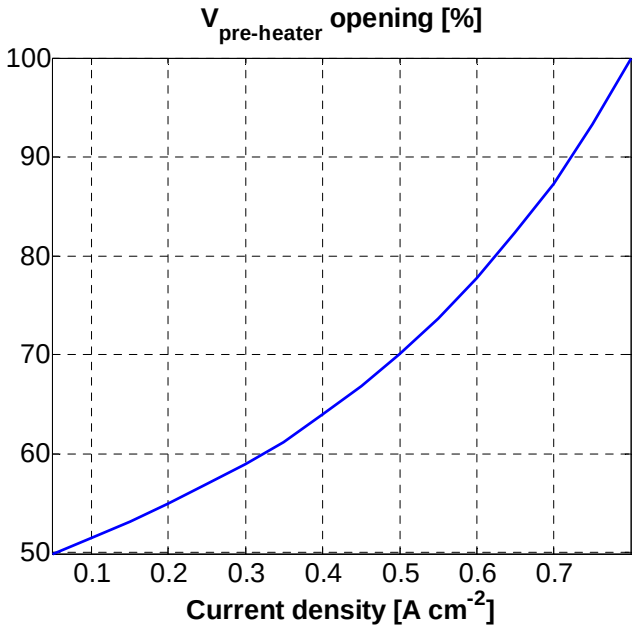

Figure 2.6 Feed-forward control map for the air pre-heater by-pass valve, located at the hot fluid line, as function of the current density.

Moreover, in accordance to the statements made by Sorrentino et al. [1], the maximum valve opening is achieved at a current density of 0.8 $A \cdot cm^{-2}$, corresponding to the operating point where the maximum gross electric power is generated. The same observation can be also referred to the control map for the fuel pre-reformer by-pass valve, depicted in Figure 2.8, presented in the next paragraph.

2.1.4 Fuel pre-reformer

The fuel pre-reformer modeled in this work is only characterized by an evaporator and a reactor, as assumed by Sorrentino et al. [2]. On one hand, the heat required for the complete reforming reaction is taken from the post-burner exhaust gases and the inlet fuel flow, which is a mixture

of methane and vapor, is evaluated considering a steam to carbon ratio equal to 2.5 and exploiting the following equations:

$$\dot{m}_{CH_4} = \frac{JA_{SOFC}}{8F}\frac{M_{CH_4}}{U_f}n_{cells} \tag{2.13}$$

$$\dot{m}_{H_2O} = 2.5\frac{M_{H_2O}}{M_{CH_4}}\dot{m}_{CH_4} \tag{2.14}$$

On the other hand, the mass flow leaving the pre-reformer is evaluated through equation (2.15), considering the outlet molar fraction of each species after the complete reaction as function of the pre-reformer temperature (as shown in Figure 2.7), in agreement with the statements made by Sorrentino et al. [2].

$$\dot{m}_{ref,out} = \sum_i \left[\left(\frac{\dot{m}_{CH_4} + \dot{m}_{H_2O}}{\sum_i M_i x_{i,ref,out}\left(T_{c,ref,out}\right)} \right) M_i x_{i,ref,out}\left(T_{c,ref,out}\right) \right] \tag{2.15}$$
$$i = [H_2, H_2O, CH_4, CO, CO_2]$$

The pre-reformer temperature considered for the molar fraction evaluation is estimated following the same approach exploited for the air pre-heater. Indeed, applying the energy conservation equation to two control volumes, one for the post burner exhaust line (hot fluid) and one containing the reactor and the evaporator (cold fluid), the thermal dynamics of both hot and cold sides can be described as:

$$\begin{aligned}\left(K_{ref} + C_{h,ref}\right)\frac{dT_{h,ref}}{dt} = {} & \dot{E}_{h,ref,in}\left(T_{h,ref,in}\right) - \dot{E}_{h,ref,out}\left(T_{h,ref,out}\right) + \\ & - U_{ref}A_{ref}\left(T_{h,ref} - T_{c,ref}\right)\end{aligned} \tag{2.16}$$

$$C_{c,ref}\frac{dT_{c,ref}}{dt}=\dot{E}_{c,ref,in}\left(T_{c,ref,in}\right)-\dot{E}_{c,ref,out}\left(T_{c,ref,out}\right)+ \\ +U_{ref}A_{ref}\left(T_{h,ref}-T_{c,ref}\right) \tag{2.17}$$

Concerning the design parameters, i.e. the solid heat capacity and the heat transfer coefficient, similar criteria as those discussed in paragraph 2.1.3 have been used. Moreover, even in this case the average hot and cold temperatures have been calculated by means of an arithmetic average (see equation 2.12).

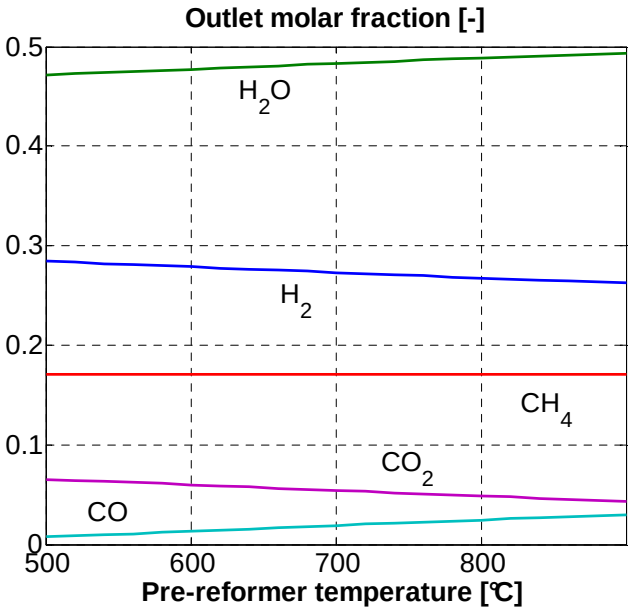

Figure 2.7 Pre-reformer outlet molar fractions of each outlet species (i.e. H_2, H_2O, CH_4, CO and CO_2) expressed as a function of the pre-reformer temperature.

In conclusion, the temperature regulation of the pre-reformer is achieved with a by-pass valve ($V_{pre\text{-}reformer}$ in Figure 2.2) similar to the one used for the pre-heater hot fluid line. This valve regulates the post-burner exhausts flow entering the pre-reformer to control the temperatures of the reformer reaction, the outlet cold fluid and the one entering the air pre-

heater. As done for the air pre-heater, the valve control is achieved with a feed-forward control map, showed in Figure 2.8, in which the valve opening is defined as function of the current density.

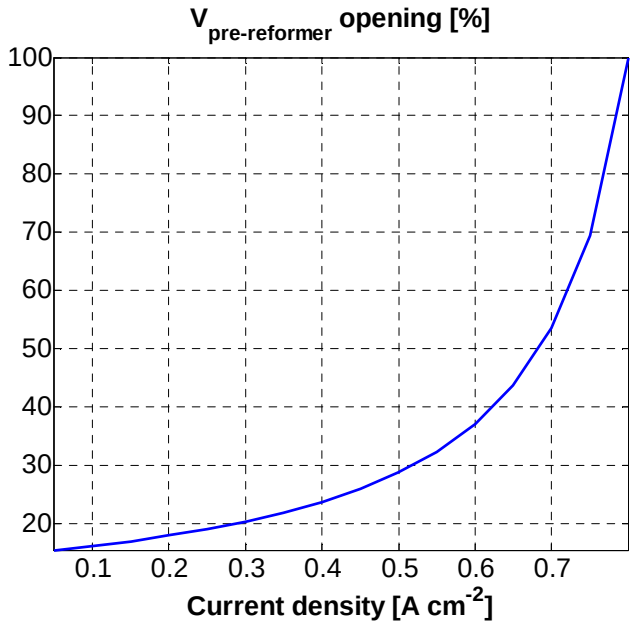

Figure 2.8 Feed-forward control map for the air pre-reformer by-pass valve, located at the hot fluid line, as function of the current density.

2.1.5 Post-burner

As explained in the previous paragraphs, the heat required to achieve the complete reformer reaction, taking place at the anode side, and to warm up the inlet air flow at the cathode side is obtained driving the anode and cathode outlet flows into the post-burner. The incoming flows are mixed together and a combustion (assumed complete and adiabatic) of the residual molecules of H_2, CO and CH_4 takes place [1][2]. This reaction produces the aforementioned required heat, which is further exploited to provide also an additional amount of thermal energy for the

final users. From the previous assumption of a complete combustion of the residuals H_2, CO and CH_4, the outlet molar flows can be estimated as function of the inlet ones [2]:

$$\dot{n}_{H_2,out} = \dot{n}_{CO_2,out} = \dot{n}_{CH_4,out} = 0 \tag{2.18a}$$

$$\dot{n}_{CO_2,out} = \dot{n}_{CO_2,in} + \dot{n}_{CO,in} + \dot{n}_{CH_4,in} \tag{2.18b}$$

$$\dot{n}_{H_2O,out} = \dot{n}_{H_2O,in} + \dot{n}_{H_2,in} + 2\dot{n}_{CH_4,in} \tag{2.18c}$$

$$\dot{n}_{O_2,out} = \dot{n}_{O_2,in} - \frac{1}{2}\dot{n}_{H_2,in} - \frac{1}{2}\dot{n}_{CO,in} - 2\dot{n}_{CH_4,in} \tag{2.18d}$$

$$\dot{n}_{N_2,out} = \dot{n}_{N_2,in} \tag{2.18e}$$

Once all the species outlet molar flows are computed, the temperature at the post-burner outlet $T_{PB,out}$ is evaluated iteratively solving the following energy balance, which holds only under the adiabatic combustion assumption [1][2]:

$$\dot{E}_{PB,in}\left(T_{SOFC,out}\right) = \dot{E}_{PB,out}\left(T_{PB,out}\right) \tag{2.19}$$

The inlet and outlet energy flows of equation (2.19) are estimated through equation (2.3) with respect to the temperatures at the stack and the post-burner outlet, respectively.

2.1.6 Pipes

The supply of the inlet gases through the auxiliary components located at the SOFC stack inlet (i.e. air blower, air pre-heater and fuel pre-reformer) is modeled introducing three distribution pipes, as can be seen in Figure 2.2. In the present work the attention has been focused only on the inlet side, neglecting the flue gas pipes at the stack and post-burner

outlet. This choice is mainly motivated by the need for the introduction of a fault sub-model at the inlet side, whereas at the outlet side no fault is considered. A deeper explanation on this point and on the reasons leading to the fault sub-models is given in Chapter 3.

The connection between two system components, for example the air blower and the air pre-heater, is guaranteed through a pipe, which is assumed horizontal and with constant section. A schematic representation of the pipe is given in Figure 2.9, in which D is the pipe diameter, L is the pipe length and $\dot{m}_{in}$ and $\dot{m}_{out}$ are the inlet and outlet pipe flows respectively.

To design the characteristic equations of the pipe model, two main assumptions are made: i) the gas is assumed ideal; ii) the gas flow is assumed isentropic with friction acting only between the gas and the inner pipe surface; ii) no heat exchange among the pipe, the gas and the ambient is considered (i.e. the pipe control volume is assumed adiabatic and isothermal). These assumptions guarantee a limited computational burden of the model.

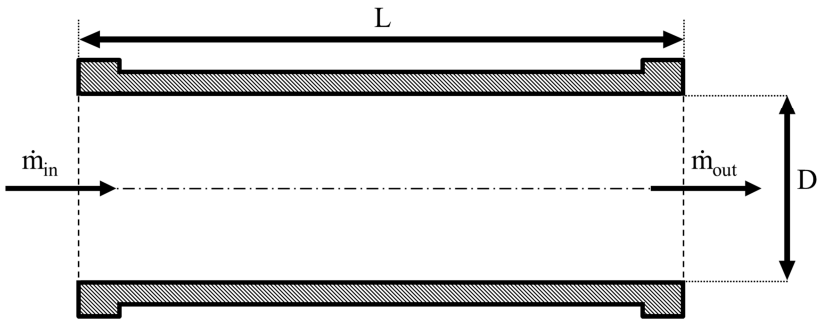

Figure 2.9 Schematic representation of a straight pipe.

Considering the scheme of Figure 2.9, the mass conservation equation can be written as follows:

$$\dot{m}_{in} = \dot{m}_{out} \tag{2.20}$$

Assuming a straight pipe (i.e. no curves or flow direction changes) with a constant section, equation (2.20) becomes:

$$\rho_{in} v_{in} = \rho_{out} v_{out} \tag{2.21}$$

where v is the component of the velocity vector in the stream direction (i.e. normal to the pipe section). Differentiating both equation (2.21) and the ideal gas law in isothermal conditions and combining them together, the following equation is obtained:

$$v dv = -v^2 \frac{dp}{p} \tag{2.22}$$

Substituting equation (2.22) into the mechanical energy equation expressed in differential form neglecting the height difference between pipe inlet and outlet, and taking into account the ideal gas law, the following differential equation is obtained [63]:

$$\frac{1}{RTv^2\rho^2} p dp - \frac{dp}{p} + \frac{f}{2D} dz = 0 \tag{2.23}$$

where f is the friction factor and z represents the generic distance from the pipe inlet, with assumption of turbulent flow [63]. Integrating equation (2.23) between pipe inlet and outlet and rearranging it, the following relationship is obtained:

$$R\frac{\pi^2}{32}\left(\frac{\rho_{in}^2 T D^4}{\dot{m}_{in}^2}\right)\left[\left(\frac{p_{out}}{p_{in}}\right)^2 - 1\right] - \ln\left(\frac{p_{out}}{p_{in}}\right) + \frac{f}{2}\left(\frac{L}{D}\right) = 0 \tag{2.24}$$

through which the outlet pressure can be calculated, upon the knowledge of the pipe length and diameter and the gas input conditions (i.e. density ρ_{in}, mass flow $\dot{m}_{in}$ and pressure p_{in}). It is important to remark that equation (2.24) applies to any gas flow (both air or fuel mixture) and to any pipe location, i.e. between the air blower and the air pre-heater, between the air pre-heater and the SOFC stack at cathode side and between the fuel pre-reformer and the SOFC stack at anode side. Moreover, the pipe temperature required in equation (2.24) is assumed constant and equal to the gas inlet temperature.

2.2 Fault sub-models

In this section the main equations developed to simulate specific faulty states are presented. The faults chosen in this work derive from the ones listed in the Fault Signature Matrix developed by Arsie et al. [4], which has been considered as a reference for the development of an improved one to be used for the inference process. Further details about the improvement process of the considered FSM via faulty states simulation is given in Chapter 3. The considered faults are:

- air blower fault induced by an increase in its mechanical losses;
- air leakage between the air blower and the air pre-heater;
- temperature controller failure;
- pre-reformer fault produced by its heat exchange surface corrosion;
- stack fault caused by an increase in its ohmic resistance;

It is worth stating that in this chapter only the fault sub-models features are described, whereas the results of each fault simulation are presented in the next chapter in conjunction with the description of the FSM improvement process.

2.2.1 Air blower fault

The first fault considered in this work entails the increase in the air blower mechanical losses. As explained more in details in paragraph 3.1.1, this fault can be ascribed to different causes. The blower performance decrease is mainly due to its rotating components degradation. For instance, bearings and surfaces could be contaminated by dirt, dust and oils, leading to motor windings overheating and failure [13]. However, other causes could be an increase in the blower motor friction, due to the wear, as well as an excessive overheating, corresponding to lack of lubrication oil [4][13]. As a consequence, the increase in blower mechanical losses results in the growth of the required

electric power, provided by the SOFC stack, and of the air outlet temperature.

To model these effects, when the fault occurs in the system, a decrease in the electric motor mechanical efficiency is introduced according to the following law:

$$\eta_{EM,F} = \eta_{EM}(1-\xi) \tag{2.25}$$

where ξ is a coefficient restricted to the range [0,1] and it is related to the fault magnitude. If the system is behaving normally (i.e. no fault is occurring into the system) the coefficient ξ is equal to 0, whereas, if the fault occurs, ξ is higher than 0, with a maximum value equal to 1, which corresponds to a complete failure of the system. Thus, the fault magnitude can be expressed as a percentage, as $\xi \cdot 100$. Substituting the faulty electric motor efficiency (equation (2.25)) into equation (2.7), the blower power in faulty condition can be evaluated as:

$$P_{B,F} = \dot{m}_{AIR} \frac{c_{p,AIR} T_{AIR,in}}{\eta_B \eta_{EM}(1-\xi)} \left(\beta^{\frac{\gamma-1}{\gamma}} - 1 \right) = \frac{P_B}{1-\xi} \tag{2.26}$$

The increase in the blower power can be caused by electric motor friction, resulting in energy dissipation as a thermal loss. This latter can be computed as the difference between the blower power in normal and faulty state, as follows:

$$Q = P_{B,F} - P_B = P_B \frac{\xi}{(1-\xi)} \tag{2.27}$$

To define the outlet temperature in faulty condition, the following assumption is made: a fraction of the thermal loss, computed with equation (2.27), is transferred to the gas flowing through the blower as thermal energy. Thus, assuming that half of the thermal loss is transmitted (i.e. 50% of Q), it is possible to write:

$$\frac{Q}{2} = \dot{m}_{AIR} c_{p,AIR} \left(T_{B,out,F} - T_{B,out} \right) \tag{2.28}$$

Reorganizing equation (2.28) and considering equation (2.6), equation (2.7) and equation (2.27), the outlet temperature in faulty condition can be defined as:

$$T_{B,out,F} = T_{AIR,in} \left[1 + \frac{1}{\eta_B} \left(\beta^{\frac{\gamma-1}{\gamma}} - 1 \right) \left(1 + \frac{\xi}{2(1-\xi)\eta_{EM}} \right) \right] \tag{2.29}$$

Observing equation (2.26) and equation (2.29), if ξ is equal to 1 the variables diverge (i.e. become infinite), meaning that a failure occurs and the system must be shut down.

2.2.2 Air leakage between air blower and air pre-heater

The second considered fault consists in an air leakage between the air blower and the air pre-heater. The causes leading to this fault are mostly related to the mechanical degradation of the seals and junctions or of the pipe surface.

To simulate this fault, a model of gas release through a hole is implemented. Starting from the pipe scheme of Figure 2.9, a representation of the pipe configuration in faulty condition is given in Figure 2.10. In this scheme it is possible to identify three main control volumes: the volumes 1 and 2, which represent the parts of the pipe not affected by leakage, and the volume in between, characterized by a length D_H representing the diameter of the hole through which the leaked gas is released.

The outlet properties of the volumes 1 and 2 can be easily evaluated through equation (2.20) and equation (2.24), upon identifying the inlet properties. On the other hand, the intermediate volume of length D_H, where the hole is located, is characterized by the following mass balance:

$$\dot{m}_{2,in} = \dot{m}_{1,out} - \dot{m}_H \tag{2.30}$$

where $\dot{m}_H$ is the hole outlet flow, which can be evaluated with the nozzle equations for compressible flow either in subsonic or sonic conditions (i.e. un-choked or choked) [14][15].

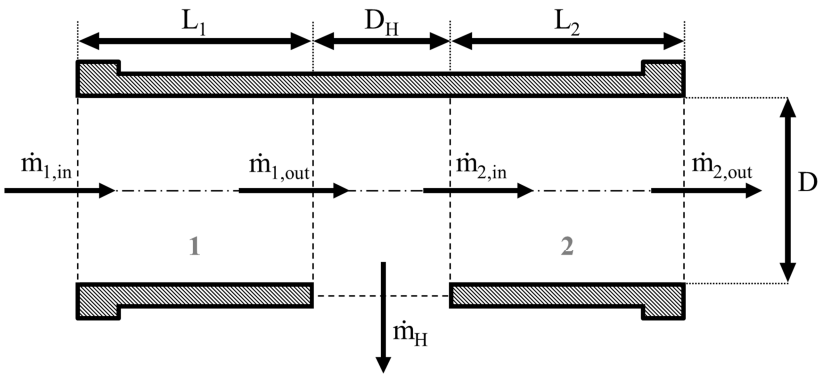

Figure 2.10 Schematic representation of a gas leakage from a straight pipe: the leakage is modeled as a gas flow $\dot{m}_H$ through a hole of diameter D_H.

To distinguish between these two different conditions, the Critical Pressure Ratio (CPR) must be considered:

$$CPR = \left(\frac{2\gamma}{\gamma+1} \right)^{\frac{\gamma}{\gamma-1}} \tag{2.31}$$

This parameter is taken as reference for the ratio between the pressure outside the pipe p_H and the pressure at the volume inlet $p_{1,out}$. Consequently, if this ratio is higher than the CPR the flow is subsonic and the flow through the hole can be modeled as:

$$\dot{m}_H = C_D \frac{\pi D_H^2}{4\sqrt{TR}} p_{1,out} \left(\frac{p_H}{p_{1,out}} \right)^{\frac{1}{\gamma}} \sqrt{\frac{2\gamma}{\gamma-1} \left[1 - \left(\frac{p_H}{p_{1,out}} \right)^{\frac{\gamma-1}{\gamma}} \right]} \tag{2.32a}$$

whereas, if the considered ratio is equal or less than the CPR, the flow is sonic (choked condition) and the flow through the pipe is computed as:

$$\dot{m}_H = C_D \frac{\pi D_H^2}{4\sqrt{TR}} \sqrt{\gamma} p_{1,out} \left(\frac{2}{\gamma+1} \right)^{\frac{\gamma+1}{2(\gamma-1)}} \tag{2.32b}$$

Once the leaked gas flow is computed, the residual flow can be evaluated through equation (2.30). To compute the other inlet gas properties for the volume 2, the assumption of a constant velocity is made (i.e. $v_{1,out} = v_{2,in}$).

2.2.3 Temperature controller failure

The third fault considered in this work is related to the failure of the temperature controller installed on the system. As mentioned in the paragraph 2.1, the stack temperature is controlled through a feedback PI controller, which reads the stack temperature signal and acts on the regulation of the air blower outlet mass flow to keep the stack temperature within the desired set-point range. A possible cause of the controller failure can be ascribed to an electronic malfunction or to an improper sensor behavior.

In this work, the controller fault is not modeled by means of a fault sub-model. To simulate this occurrence the PI controller is disabled, upon reaching a steady state condition. Afterwards, a standard load change maneuver is imposed. The idea is to study the system reaction to a current step-change when it is in uncontrolled condition. Indeed, the PI controller removal prevents the system from correctly adapting to the new operating condition.

2.2.4 Pre-reformer heat exchange surface corrosion

The fourth modeled fault consists in the pre-reformer heat exchange surface corrosion/erosion. This fault can be mainly caused by the

occurrence of operating temperatures higher than those related to the design point and the presence of sulfur [4][13]. More in details, the generation of corrosion products may foul the heat exchange surface, changing its thermal features [61]. For example, the products adhesion on the surface can induce an increase in the heat transfer resistance [61]. To simulate this event, the heat exchanger surface area A_{ref} is reduced according to the following equation:

$$A_{ref,F} = A_{ref}\left(1-\chi\right) \tag{2.33}$$

where the coefficient χ is a coefficient limited within the range [0,1] and it is related to the fault magnitude, as seen for the coefficient ξ. The reduction of this surface through equation (2.33) directly affects the outlet hot and cold fluid temperature, according to equation (2.16) and equation (2.17). Moreover, the induction of a variation in the pre-reformer temperature also affects the outlet fuel composition (see Figure 2.7).

2.2.5 Increase in cell ohmic resistance

While the former modeled faults take place at specific BOP components, the fifth and last fault analyzed in this work is related to the SOFC stack. In more detail, this fault concerns the increase in the stack ohmic resistance, which can be ascribed to many causes, for instance the growth at cathode side of an electrically less conductive oxide layer between the electrode and the interconnection plates, or chromium deposition on the interconnection surfaces [4]. Other causes can be identified in cell components deformation (e.g. rib detachment), leading to contact degradation between the interconnect and the electrodes, and in undesired thermal cycling and gradients [4][13]. In the current work, the exploitation of a *black-box* regression (see equation (2.2)) for modeling the SOFC stack voltage, instead of a detailed electrochemical model, hinders the possibility to model this fault in detail. However, an increase in the stack ohmic resistance corresponds to a decrease in the stack voltage at constant current, due to the growth of the related ohmic losses [5]. For this reason, the specific fault is modeled directly as a stack

voltage reduction, according to the following relationship:

$$V_{SOFC,F} = V_{SOFC}(1-\varepsilon) \tag{2.34}$$

where ε, as in the case of ξ and χ, is a coefficient varying in the range [0,1] and it is related to the fault magnitude. It is worth emphasizing that the choice of using a *black-box* relationship to describe the SOFC voltage behavior reduces the model generalizability and its physical coherence. However, it allows the exploitation of the model for those applications in which the computational time has to be kept low, e.g. for control strategies and diagnostic applications both for online and real time uses, without a sensible reduction of the accuracy and robustness.

2.3 Model simulation in normal operating conditions

As a final point, the results of the methane-fueled SOFC system model simulation in normal operating conditions are herein presented. In Figure 2.11 the same plant scheme of Figure 2.2 is again depicted, but with the representation of the values associated to the main monitored variables, referring to a current request of 25 A. These results refer to the parameters listed in Table 2.1.

The representation given in Figure 2.11 has been adapted from the illustration provided by Sorrentino et al. in their papers [1][2]. Considering the values conveyed in [1] and [2] (not listed here for the sake of conciseness), the present model suitably reproduces the same behavior of the model of Sorrentino et al. [1][2]. For further details the reader is addresses to the aforementioned works [1][2]. Clearly, the values depicted in Figure 2.11 refer to the steady state condition for a current request of 25 A. To ensure the desired stack temperature level, here set equal to 825°C, the PI controller acts on the blower speed to regulate the inlet air flow, changing in this way the excess of air value. At steady state, for this specific operating point, the reached excess of air corresponds to 4.81. Furthermore, it is possible to compute the net electric system efficiency through equation (2.9) obtaining a value of 0.39 for a methane HHV of 55,530 J kg^{-1}.

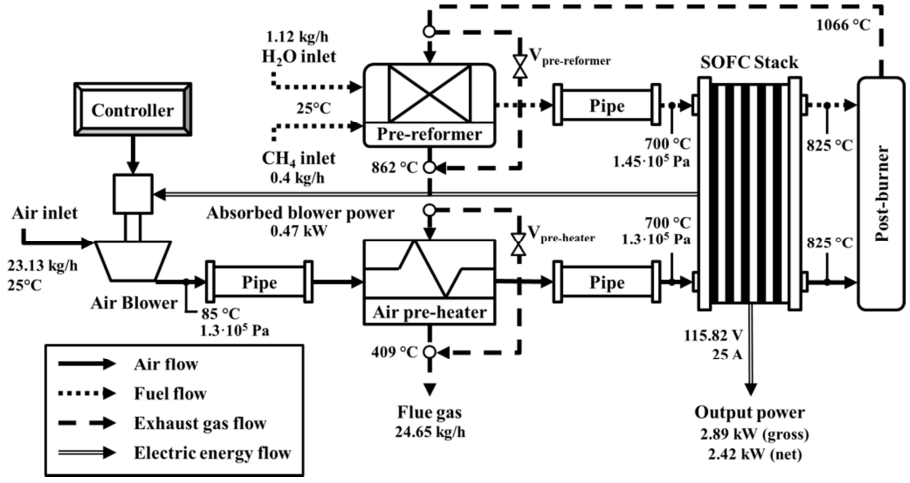

Figure 2.11 Methane-fueled SOFC plant scheme with description of the main monitored variables values related to a current request of 25 A.

Table 2.1 Methane-fueled SOFC system model specifications [2].

Parameter	Description	Value	Unit
A_{SOFC}	electroactive area	100	cm^2
n_{cells}	cells number	150	-
K_{SOFC}	stack solid heat capacity	8234	$J\ K^{-1}$
U_f	fuel utilization	0.7	-
$T_{Air,in}$	inlet air temperature	25	°C
$p_{AIR,in}$	inlet air pressure	10^5	Pa
β	blower pressure ratio	1.3	-
η_{EM}	electric motor efficiency	0.9	-
U_{HE}	pre-heater coefficient	200	$W\ m^{-2}\ K^{-1}$
A_{HE}	pre-heater surface	0.3	m^2
K_{HE}	pre-heater heat capacity	316	$J\ K^{-1}$
U_{ref}	pre-reformer coefficient	200	$W\ m^{-2}\ K^{-1}$
A_{ref}	pre-reformer surface	0.06	m^2
K_{ref}	pre-reformer heat capacity	59	$J\ K^{-1}$

The simulation results presented in this paragraph are exploited in the next chapter as reference for the analysis of the monitored variables behavior during the system simulation in faulty conditions.

As a final point, examples of the dynamic responses to a current step change of the single cell voltage, the stack temperature and the excess of air are given in Figure 2.12, Figure 2.13 and Figure 2.14 respectively. In these pictures the variables behaviors in both uncontrolled (i.e PI disabled) and controlled (i.e. PI enabled) conditions are represented. The step change corresponds to an increase of the drained current from 25 A to 40 A.

In Figure 2.12 it can be observed that, in controlled conditions (red dashed line), the voltage drops from 0.772 V to almost 0.718 V. On the other hand, in uncontrolled condition (blue straight line), it decreases only to 0.747 V, but with a larger undershoot and a longer dynamics. The higher voltage level reached in uncontrolled condition strictly depends on the stack temperature behavior.

As can be seen in Figure 2.13, in uncontrolled condition (blue straight line), the stack temperature increases, inducing the observed less reduction in the cell voltage.

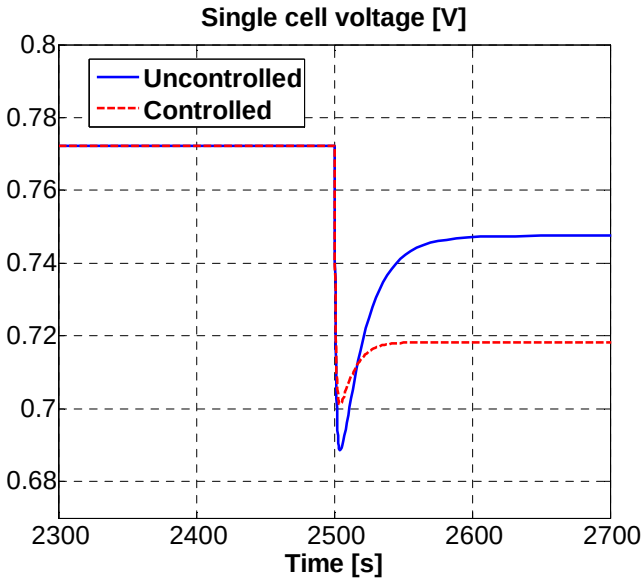

Figure 2.12 Comparison between uncontrolled and controlled single cell voltage response to a current step change from 25 A to 40 A.

The initial temperature undershoot is caused by the sudden increment in

the air and fuel flows, which are algebraically related to the current through equation (2.5) and equation (2.13) respectively. This instantaneous variation of the cold gas flows (i.e. no mass transport dynamics has been implemented in this model) directly impacts on the cold fluid outlet temperatures of both the air pre-heater and the fuel pre-reformer (mainly at the valves outlet mixing point), which in turn affect the stack temperature. Nevertheless, the fuel amount increase leads to a growth in the inlet energy flow, with a consequent rise of the temperature at the stack outlet, driven by the stack thermal dynamics.

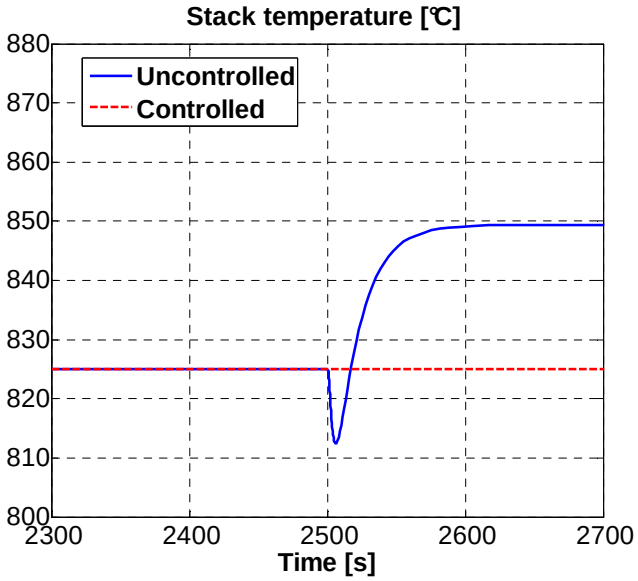

Figure 2.13 Comparison between uncontrolled and controlled stack temperature response to a current step change from 25 A to 40 A.

Concerning the stack temperature behavior in controlled condition (red dashed line), it does not diverge from the desired set-point value, as expected. In such a case, the excess of air, which is regulated by the PI controller, changes to adapt the air flow so as to keep the stack temperature near the set-point. Indeed, in Figure 2.14 it can be seen that the excess of air initially decreases (controlled condition – red dashed line), to contrast the stack temperature drop (blue straight line in Figure 2.13), which is induced by the sudden increase of the air and the fuel

flows. Afterwards, it rises to ensure the stack cooling in order to prevent the following temperature increase.

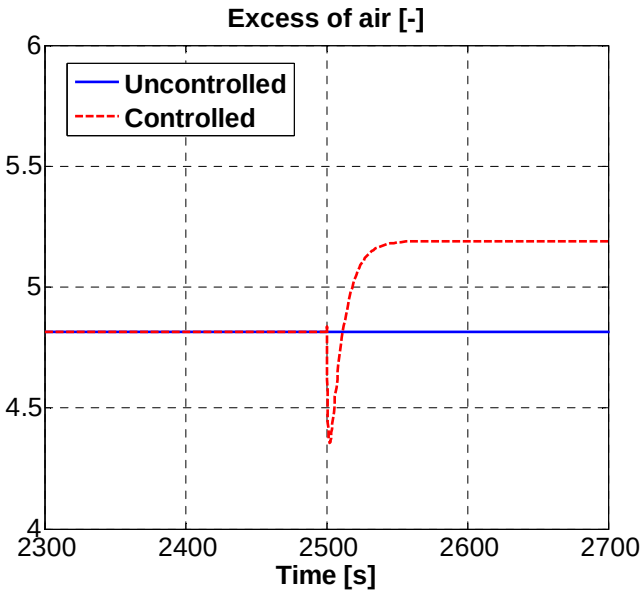

Figure 2.14 Comparison between uncontrolled and controlled excess of air response to a current step change from 25 A to 40 A.

On the other hand, in uncontrolled condition (blue straight line) the excess of air remains constant.

CHAPTER 3 Improved FSM

The mathematical model developed in the previous chapter can be considered the core element of the model-based diagnosis algorithm. Without a proper designed model no residual can be computed, the related monitoring process cannot be accomplished and so the whole diagnosis procedure cannot begin. However, as explained in details in Chapter 1, even though the mathematical model is suitably developed, but an accurate inference procedure is not designed, the diagnosis procedure cannot be completed.

In this work the Fault Signature Matrix (FSM) developed by Arsie at al. [4], following a Fault Tree Analysis (FTA), is considered as a starting reference to develop an improved FSM by means of faults simulation through the methane-fueled SOFC system model (based on the work of Sorrentino et al. [1][2]) herein developed. As showed in the following paragraphs, this model is exploited to simulate the system in normal operating conditions, so as to define the values of the monitored variables in normal state, and in faulty operating conditions, in order to compute the variables values in faulty state.

The comparison of the variables values in these states leads to the computation of residuals, which are later analyzed introducing specific thresholds to generate analytical symptoms. Then, the symptoms vector obtained for each simulated fault is compared to the one included in the FSM of Arsie et al. [4]. In this way, it is possible to appreciate the differences between the FSM developed through a heuristic approach (i.e. the FTA) and the one obtained considering also the system sensitivity to the faults magnitude. The former accounts only for qualitative relationships among the faults and the symptoms, whereas the latter takes into account both the direct and indirect correlations among the system variables.

As emphasized in paragraph 1.3, the direct use of the FSM as developed only through the FTA may lead to a non-optimized isolation process, and its enhancement can be achieved via quantitative model-

based simulations [27]. A schematic representation of the guidelines of this approach is given in Figure 3.1.

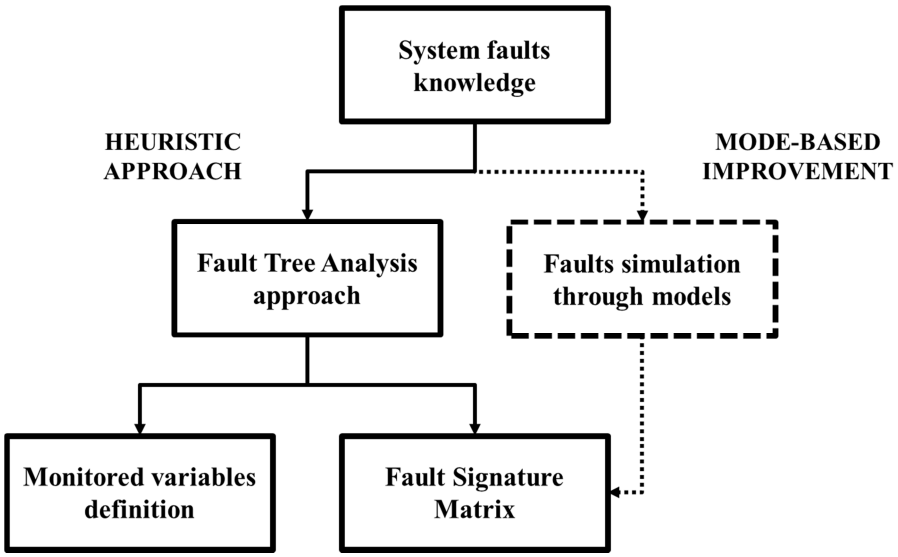

Figure 3.1 Integration of heuristic and model-based approaches for FSM development, by means of Fault Tree Analysis approach and specific faults simulation through mathematical models.

The idea of using a model to simulate a system also during faulty states is exploited by several authors. As an example, Escobet et al. [17] improved a PEM fuel cell system simulator model by including sub-models, simulating an increase in the compressor motor friction, the compressor overheating, a leakage in the air supply manifold and the temperature controller failure. Ingimundarson et al. [18] developed an hydrogen leakage model for a PEM fuel cell stack, whereas Simani et al. [21] proposed a turbine prototype model, which includes sub-models simulating the compressor blades failure, a reduction in the turbine efficiency and a fault in the thermocouple sensor and in the controller actuator.

In the following, a brief description of the main characteristics concerning the FTA approach is given, with an example of the development procedure of a fault tree for an air blower. Then, the FSM developed by Arsie et al. [4] is presented, followed by the aforementioned

improvement process by means of faults simulation through the SOFC system model presented in Chapter 2. It is worth remarking that the main issue discussed in this chapter concerns only the theoretical development of a FSM through the exploitation of faults models and simulations, whereas in the next chapters the application of the developed FSM, embedded into a comprehensive diagnostic algorithm, and the experimental induction of controlled faulty state in a real SOFC system is presented.

3.1 Fault Tree Analysis approach

The FTA is an analytical deductive technique that can outline all the possible ways in which a malfunction or undesired behavior can occur in the system [4][12]. This methodology allows the understanding of how a sudden fault can occur in a system and how it can influence the system devices [13]. The main outcome of the FTA is a fault tree, which consists in a graphic representation of the logical connections linking precise events to a specific undesired fault. It is worth noting that a fault tree does not represent all possible system faults and their causes, but only those assessed by the analysts [12].

The design process of a fault tree starts from a specific fault (which is the top event) and investigates all the possible causes (which are the basic events, or symptoms), from which the considered fault can result [4]. This process is based on the physical knowledge of the system and follows a top-down approach, going from the fault to the symptoms through intermediate events. The higher level of the fault tree is the top event (i.e. the fault or malfunction under study), while the other levels are represented by intermediate events, which are other minor faults that occur due to the previous causes. The bottom level is represented by the basic events (the symptoms), which may also correspond to specific faults that are not further developable [12]. A schematic representation of a generic fault tree is given in Figure 3.2, where each aforementioned element is depicted. In this picture it is also possible to distinguish between the design and the diagnosis procedures: the first one, required for the fault tree development, starts from the top level (the considered fault) and goes through the lower levels (intermediate events and

symptoms), identifying each correlation leading to the basic symptoms; on the other hand, the diagnosis process follows a bottom-up approach, gathering symptoms and observing which fault is linked to them. The connections among all the considered events are expressed through Boolean operators (i.e. gates), which allow or prevent the flow through the fault tree from one level to another. In Figure 3.2 an example of an AND gate is given, which connects the two symptoms to the upper intermediate event. This gate means that the specific event occurs only if all the related symptoms arise.

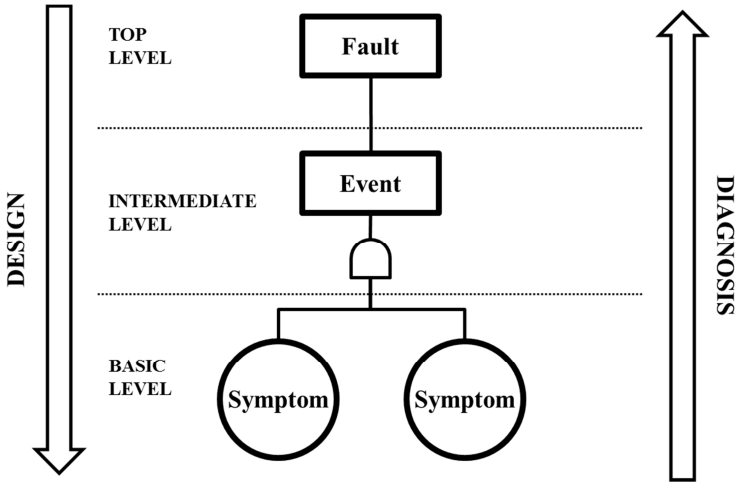

Figure 3.2 Schematic representation of a generic fault tree: the design process follows a top-down approach – from the top level (fault) to the basic level (symptoms) – whereas the diagnosis process follows a bottom-up approach – from the symptoms to the fault.

It is worth noting that in a complex system the same symptoms can be related to different faults, consequently proper symptoms redundancy is required [13]. Furthermore, it must be recalled that this methodology gives only qualitative correlations among the faults and the symptoms [12]. For this reasons, the major drawback of the FTA can be identified in the inability to detect faults that are not considered into the analysis and to distinguish between incipient and severe faults [23]. To overcome these limitations, an exhaustive and deep knowledge of the system components and their most probable undesired behavior, in combination with

improved diagnostic methodologies, is required.

The drawing of fault trees for undesired events, which can occur into a complex system, is particularly significant for the selection of the variables that must be measured or estimated (e.g. when a specific measurement device is not available or the variable is not physically measurable). This methodology leads to the selection of the monitored variables through a balance among their significance (the number and type of faults whom is related to) and measurement costs and feasibility. Once all the considered fault trees for a specific system are developed, a complete list of the variables to be monitored (i.e. symptoms) during the diagnosis process is defined. Afterward, the correlations among these symptoms and the considered faults can be merged into a matrix, known as Fault Signature Matrix (FSM).

The FSM is a two-dimensional matrix, in whose rows the considered faults are listed, whereas the columns list all the collected symptoms, each one referring to a specific monitored system variable. The FSM herein introduced denotes the FTA approach final outcome and can be directly exploited as a reference for the isolation procedure of a diagnostic algorithm. Concerning the methane fueled SOFC system described in paragraph 2.1, the application of the FTA approach to this system had been already performed by Arsie et al. [4] and Di Filippi [13]. Their results are herein exploited to develop the improved FSM, starting from the one obtained from an FTA approach and exploiting the mathematical model introduced in the previous chapter. As already explained, this model simulates specific faulty states to evaluate the sensitivity of the monitored variables to the specific faults and their magnitude through the introduction of several threshold levels.

In the following paragraphs an example of fault tree development for the air blower dedicated to the aforementioned SOFC system is given. Then, the FSM developed by Arsie et al. [4], by means of an FTA approach is presented, followed by the improvement procedure, performed via faulty states simulation. This allows to identify the quantitative correlations among faults and symptoms and to obtain a more robust and reliable FSM.

3.1.1 Air blower fault tree example

The application of the FTA to the aforementioned SOFC system requires a deep knowledge of the interaction among the main components (i.e. stack and BOP). Furthermore, the complexity of these correlations suggests analyzing the faults at the component level [4]. An example of fault tree for the air blower is depicted in Figure 3.3. As previously stated, the air blower feeds the stack with the required amount of air at ambient conditions (i.e. pressure, temperature and humidity), to ensure the oxygen amount needed for the electrochemical reaction and the stack cooling. Due to the high volume flow, the blower can be identified as the most energy consuming device and it is usually prone to several types of faults and malfunctions. As specified in paragraph 2.2.1, the blower performance decrease is mainly caused by its rotating components degradation. As an example, bearings and surfaces can be contaminated by dirt, dust and oils, leading to motor windings overheating and failure.

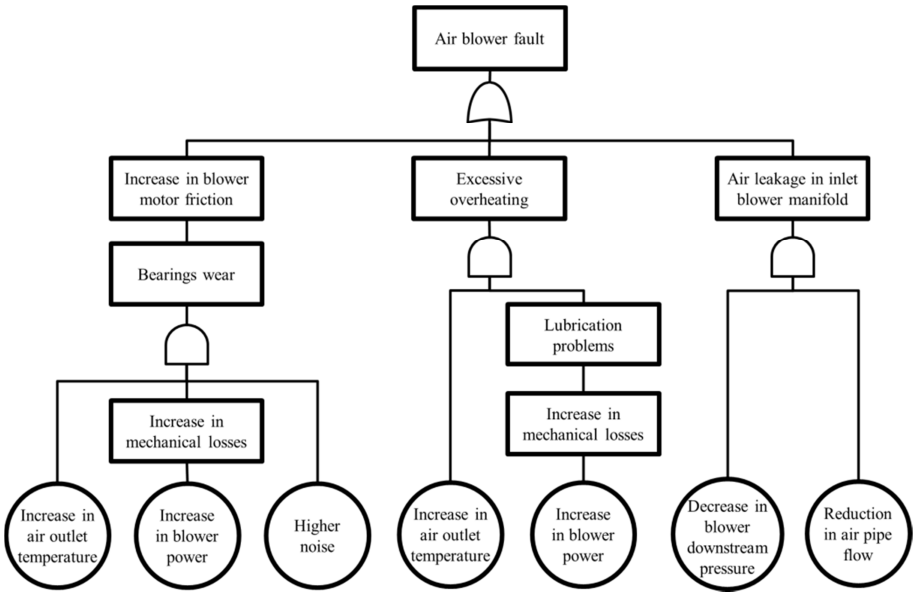

Figure 3.3 Example of a fault tree for an air blower dedicated to an SOFC system, adapted from [4] and [13].

Moreover, an increase in the system pressure drop can induce a rise in the blower absorbed power at the same flow amount [13]. Other possible faults can be associated to an increase in the electric motor friction, due to the wear, as well as an excessive overheating induced by the lack of lubrication oil [4][13]. Observing the fault tree sketched in Figure 3.3, the specific faults considered in this study consists in: i) the increase in the blower motor friction, ii) an excessive overheating and iii) an air leakage in the inlet blower manifold. Neglecting the noise intensification, it is clear that both the motor friction increase and the excessive overheating induce a growth in the air outlet temperature and in the blower absorbed power, whereas the leakage in the inlet manifold leads to the decrease in the downstream pressure and the pipe flow.

From Figure 3.3, the monitoring variables required for the detection of the considered blower faults can be identified as: i) the temperature at the blower outlet, ii) the absorbed power, iii) the downstream pressure and iv) the outlet gas flow. With the definition of these variables, the description of the fault tree design procedure is completed.

3.1.2 Fault Signature Matrix

Following the same procedure explained in the previous section, Arsie et al. [4] developed several fault trees for all the components of the aforementioned SOFC system, accounting for the interactions among each device. Subsequently, the correlations among the considered faults and the collected symptoms have been merged into a Fault Signature Matrix, presented with some adaptations in Table 3.1.

As previously explained, an FSM is a two-dimensional matrix, in which the considered faults are listed on the rows and the collected symptoms on the columns. When a symptom is related to a fault, the corresponding element in the matrix is equal to 1, otherwise is 0. Further details about the build-up process of the FSM developed by Arsie et al. can be found in the work listed in the references [4].

From this initial FSM, the one presented in Table 3.1 has been obtained by mean of several modifications, necessary to meet the specifications required for the experimental validation of the diagnostic algorithm. The first accomplished modification resides in the association

of the pre-reformer fault (i.e. fault f_4 in Table 3.1) to an undesired event caused by heat exchange surface corrosion rather than catalyst degradation. According to the pre-reformer fault tree presented by Arsie et al. [4], the variables (i.e. the symptoms) affected by these faults are the same except for a possible increase in the pressure drop. However, since this last variable is not monitored, the symptoms vector proposed in [4] can be used as a reference for both the catalyst degradation and the heat exchanger surface corrosion. The second modification consists in the association of the stack fault to an increase in the stack ohmic resistance instead of a reduction in the electrochemical active area. Again, according to the related fault tree, presented in [4], the only variation in the symptoms vector is showed by the current density symptom, which turns from 1 to 0.

Table 3.1 Fault Signature Matrix developed following only an FTA approach, adapted from the work of Arsie et al. [4].

	Symptoms	Stack power	Blower power	Net power	Stack temperature	Excess of air	Fuel temperature at anode inlet	Post burner exhaust temperature	Air temperature at blower outlet	Hot fluid temperature at air pre-heater inlet	Air temperature at cathode inlet	Current density	Stack voltage	Air mass at cathode inlet	Temperature at anode outlet	Air temperature at cathode outlet
Faults		s_1	s_2	s_3	s_4	s_5	s_6	s_7	s_8	s_9	s_{10}	s_{11}	s_{12}	s_{13}	s_{14}	s_{15}
Air blower fault	f_1	0	1	1	0	0	0	0	1	0	1	0	0	0	0	0
Air leakage between air blower and pre-heater	f_2	0	1	1	0	0	0	0	0	0	0	0	0	0	0	0
Temperature controller failure	f_3	1	0	1	1	0	1	1	0	1	1	0	1	0	1	1
Pre-reformer fault	f_4	1	1	1	0	1	1	1	0	1	1	0	1	1	0	0
Stack fault	f_5	1	1	1	0	1	1	1	0	1	1	0	1	1	0	0

It is worth recalling that all the rows in the FSM must be different from one another, to allow the correct isolation of the considered faults in the system. In other words, the number of symptoms must be chosen also considering that each fault must be univocally identified by its corresponding symptoms vector. However, observing the two last symptoms vectors of the FSM presented in Table 3.1, they show the same pattern. For this reason, the FSM as here presented cannot be directly

implemented into a comprehensive diagnostic algorithm. Therefore, the choice of further variables to be monitored in the system can overcome this problem. Nevertheless a quantitative study of the correlations among faults and symptoms through a fault simulation process can be effective in the same way. This statement is proved in the following where the complete improvement procedure is described. Moreover, it is worth noting that the current density column in Table 3.1 has all zeroes, but this symptom is not deleted in order to prove that the simulation results are in accordance with what expected. According to the FSM of Table 3.1, the faults taken into account in this work, and already presented in paragraph 2.2, consist of:

- *Fault* f_1: air blower fault induced by an increase in its mechanical losses;
- *Fault* f_2: air leakage between the air blower and the air pre-heater;
- *Fault* f_3: temperature controller failure;
- *Fault* f_4: pre-reformer fault produced by its heat exchange surface corrosion;
- *Fault* f_5: stack fault caused by an increase in its ohmic resistance;

whereas the monitored variables to which the symptoms are related are:

- *Symptom* s_1: stack gross power;
- *Symptom* s_2: blower absorbed power;
- *Symptom* s_3: net electric power;
- *Symptom* s_4: stack temperature;
- *Symptom* s_5: excess of air;
- *Symptom* s_6: fuel temperature at anode inlet;
- *Symptom* s_7: post burner exhaust temperature;
- *Symptom* s_8: air temperature at blower outlet;
- *Symptom* s_9: hot fluid temperature at air pre-heater inlet;
- *Symptom* s_{10}: air temperature at cathode inlet;
- *Symptom* s_{11}: current density;
- *Symptom* s_{12}: stack voltage;
- *Symptom* s_{13}: air mass flow at cathode inlet;
- *Symptom* s_{14}: temperature at anode outlet;

- *Symptom* s_{15}: air temperature at cathode outlet.

From the faults listed into this FSM it is now possible to justify the choice of the fault sub-models described in paragraph 2.2. Each sub-model must reproduce the same effects induced by the related fault on the real system. On the other hand, the list of the monitored variables has given a reference on the properties from which the symptoms must be generated. In the following section, the results of the simulation of faulty states through the SOFC model of Chapter 2 is presented. By means of this simulation the quantitative correlations among the considered faults and the monitored variables is evaluated, taking into account both the direct and indirect links among the variables, which cannot be completely identified through only a heuristic approach.

3.2 FSM improvement via faults simulation

The simulation of the aforementioned faults allows deriving a quantitative relationship linking the monitored variables variation and the faults magnitude. In this context, the model presented in Chapter 2 is used to simulate both the normal and the faulty behavior of the system.

The process starts with the generation of the values of the monitored variables (i.e. the symptoms listed in the FSM of Table 3.1) in normal operating condition. The same operating condition defined for the model simulation results presented in paragraph 2.3 is considered: the current request is set to 25 A and the other parameters values are those presented in Table 2.1. The values obtained for this specific operating condition have already been presented in Figure 2.11 and here proposed in Table 3.2 for all the monitored variables. It must be remarked that these values are meaningful not only for the residuals computation but also for the definition of the reference threshold values required for the analytical symptoms generation.

As showed in the following, the threshold level associated to each symptom is chosen proportional to the value of the related monitored variable in normal condition (i.e. equal to a specific percentage of this value).

The main advantage of this choice is the definition of variable thresholds (instead of fixed ones), defined as a function of the current operating condition. Moreover, in this way it is possible to set the same value (i.e. the same percentage) for each threshold level, to allow a uniform interpretation of the results.

Table 3.2 Monitored variables values for the reference operating condition: the current request is set to 25 A and the other model parameters values are chosen according to those of Table 2.1.

No.	Variable	Value	Unit
s_1	stack gross power	2.8955	kW
s_2	blower absorbed power	0.4692	kW
s_3	net electric power	2.4263	kW
s_4	stack temperature	825.00	°C
s_5	excess of air	4.8124	-
s_6	fuel temperature at anode inlet	700.01	°C
s_7	post burner exhaust temperature	1065.6	°C
s_8	air temperature at blower outlet	85.68	°C
s_9	hot fluid temperature at air pre-heater inlet	862.32	°C
s_{10}	air temperature at cathode inlet	700.22	°C
s_{11}	current density	0.25	A cm^{-2}
s_{12}	stack voltage	115.82	V
s_{13}	air mass flow at cathode inlet	23.126	kg h^{-1}
s_{14}	temperature at anode outlet	825.00	°C
s_{15}	air temperature at cathode outlet	825.00	°C

This choice motivates the calculation of the residuals as a relative difference, not as an absolute one as described in equation (1.1), as follows:

$$r = \frac{Y - \hat{Y}}{\hat{Y}} \tag{3.1}$$

where the term Y corresponds to the monitored variables simulated in faulty state, whereas the term $\hat{Y}$ corresponds to the monitored variables simulated in normal state. This approach gives for each monitored

variable a uniform evaluation of the deviation from the normal conditions and the same choice of the thresholds values, as previously suggested. Furthermore, due to the binary coding of the generated symptoms (see equation (1.2)), the residuals evaluation is performed neglecting their sign and observing only if they overcome or not the defined thresholds.

For a suitable fault simulation process, the SOFC system model, whose block diagram developed in the MATLAB/Simulink® environment is presented in Figure 3.4, is provided with a dedicated block (*fault generation* block) allowing the induction of the chosen faults at the desired time.

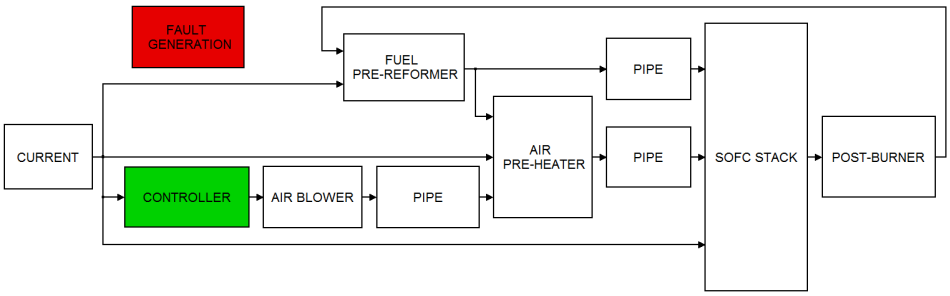

Figure 3.4 Block diagram of the SOFC system model developed in MATLAB/Simulink® environment.

From Figure 3.4 it is also possible to appreciate that the block diagram has been designed to reproduce the same structure of the plant scheme of Figure 2.2, so as to preserve the correspondence of the model blocks to the real system components. All the simulations are performed considering the assumption that only one fault at a time can occur in the system.

3.2.1 Fault f_1: air blower fault simulation

The increase in the air blower mechanical losses is simulated inducing a reduction in the electric motor mechanical efficiency, according to the equations presented in paragraph 2.2.1. In this simulation, the fault magnitude is set equal to 10%, which means that the fault coefficient ξ is

raised from 0 to 0.1. This value may correspond to an incipient fault. The effects which can be immediately identified when the fault takes place consist in the increase in the blower power and in the temperature at the blower outlet, as expected from equation (2.26) and equation (2.29), herein presented in Figure 3.5.

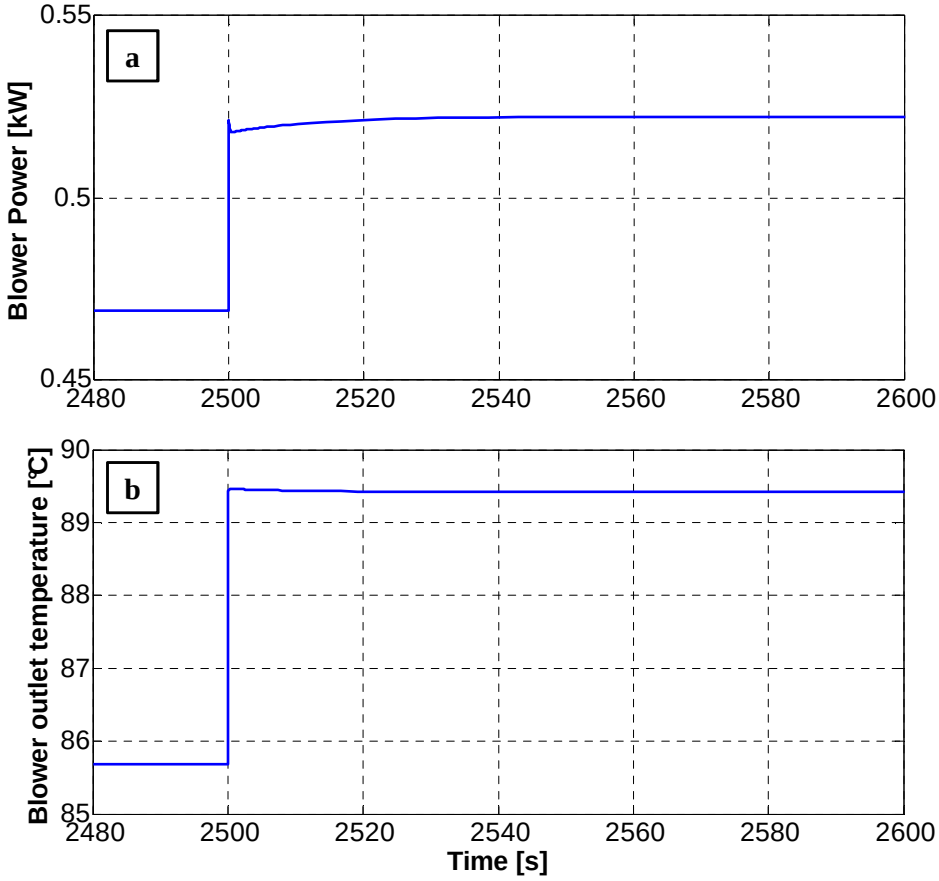

Figure 3.5 Increase in the blower absorbed power (a) and in the outlet temperature (b) due to the occurrence of a reduction of about 10% of the mechanical efficiency.

From Figure 3.5-a it is possible to notice that, when the fault occurs at 2500 s, the blower power suddenly diverges from 0.4692 kW, reaching at steady state a value of 0.5223 kW. This increase of 53.1 W represents a

variation of about 11.3% of the value in normal condition. On the other hand, the outlet temperature variation, reported in Figure 3.5-b, consists in a rapid growth from 85.68°C to 89.42°C, corresponding to a variation of around 1% (evaluated in Kelvin) at steady state. By gathering all the steady state values of the monitored variables once the fault has occurred, the residuals are calculated taking into account the values in normal condition listed in Table 3.2. In particular, it is worth noting that all the residuals related to the temperatures are evaluated considering these last expressed in Kelvin.

The results of this simulation in terms of residuals are summarized in Figure 3.6, where the blue bars represent the percent residuals computed with equation (3.1), once every monitored value have reached the steady state. On the x-axis the number of each monitored variable, and thus its related symptom, is listed with reference to the order followed in Table 3.2. In this picture two threshold values are also sketched, set respectively to ±1% (red straight-dot line) and ±5% (green dashed line).

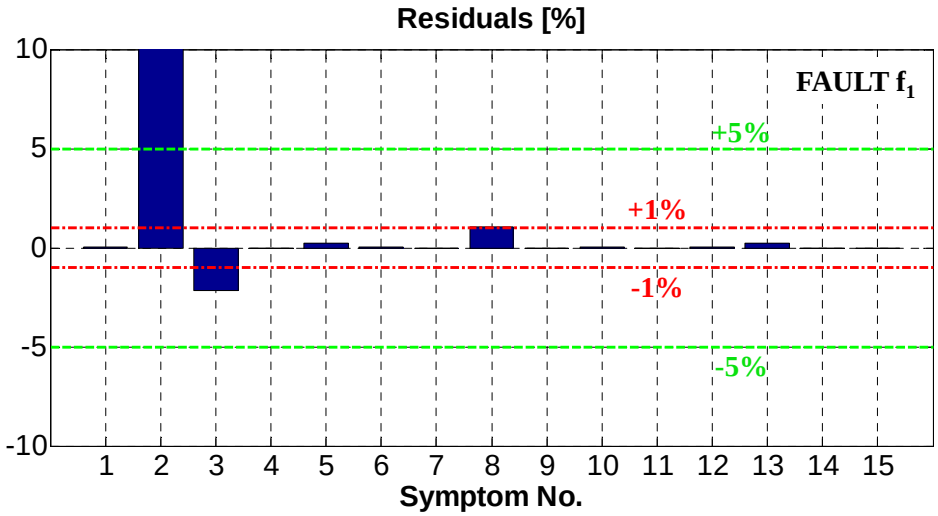

Figure 3.6 Air blower fault simulation results: comparison among the residuals and the defined thresholds at ±1% (red straight-dot line) and at ±5% (green dashed line) of the monitored variables obtained for a fault magnitude of 10%.

Apart from the two threshold levels, in Figure 3.6 it is possible to observe

that a sensible variation is showed only for the blower power (symptom s_2), the net electric power (symptom s_3) and the temperature at the blower outlet (symptom s_8), all exceeding the ±1% threshold, whereas the other variables exhibit a really small deviation, if any. However, from the three aforementioned symptoms, only the blower power overcomes the ±5% threshold. For this reason, the assumption of two threshold levels leads to the definition of two different symptoms vectors, as represented in Table 3.3, which are both compared to the symptom vector of the starting FSM of Table 3.1 (first row – FSM). The differences among the two symptoms vectors obtained through the fault simulation with respect to the initial FSM are highlighted using a grey background color for the cells of the vectors.

Table 3.3 Symptoms vectors related to an air blower fault of 10% of magnitude obtained for two threshold levels of ±1% and ±5%.

Fault f_1	s_1	s_2	s_3	s_4	s_5	s_6	s_7	s_8	s_9	s_{10}	s_{11}	s_{12}	s_{13}	s_{14}	s_{15}
FSM	0	1	1	0	0	0	0	1	0	1	0	0	0	0	0
τ = 1%	0	1	1	0	0	0	0	1	0	0	0	0	0	0	0
τ = 5%	0	1	0	0	0	0	0	0	0	0	0	0	0	0	0

From Table 3.3 it is possible to point out that the symptoms vector related to a threshold level of ±1% shows only the variation of the symptom related to the air temperature at cathode inlet (s_{10}), which changes from 1 to 0. This means that this symptom is no more involved into the isolation of the specific fault.

The motivation for this discrepancy resides in the small increment in the air flow (about 0.048 $kg \cdot h^{-1}$, barely visible in Figure 3.6 – symptom s_{13}) induced by the controller to keep the stack temperature near the set-point. This increment leads to the compensation of the temperature at the blower outlet, which could induce, in uncontrolled condition, an increase in the stack temperature. This latter comment underlines the needs for a deep knowledge of the system under study, including the controlled behavior.

Observing the symptoms vector related to a threshold level of ±5%, it differs from the one of the starting FSM not only in the air temperature at

cathode inlet (symptom s_{10}), as for the previous one, but also in the temperature at the blower outlet (symptom s_8) and the net electric power (symptom s_3), which all change from 1 to 0. However, this variation is motivated by the small residuals values of the aforementioned variables, which are all lower than 5%.

3.2.2 Fault f_2: air leakage simulation

The air leakage between the air blower and the air pre-heater is simulated through the fault sub-model described in paragraph 2.2.2. The fault induction is achieved imposing at a specific time a value for the hole diameter D_H, required for the evaluation of the released mass flow by means of equation (2.32a) – un-chocked condition – or equation (2.32b) – chocked condition. Moreover, the pressure outside the pipe p_H is assumed equal to the ambient pressure.

The results presented in the following refer to a hole diameter of 2.5 mm, which induces a mass release of 2.526 kg h^{-1}. Considering that the air mass flow rate in normal condition corresponds to 23.126 kg h^{-1}, the leaked mass is 10% of the normal amount, thus the fault magnitude can be assumed as that of an incipient fault. The abrupt effect of the gas release entails the reduction in the excess of air (measured at the stack inlet) as showed in Figure 3.7-a at 2500 s. In this picture it is possible to identify an immediate decrease in the excess of air due to the air flow reduction at the cathode inlet induced by the leakage. However, this variation results in the stack temperature sudden increase, which induces the PI controller to act on the blower speed to increase the outlet air mass flow (Figure 3.7-b) and, as a consequence, to bring the stack temperature back to the desired set-point. Thus, the inlet air mass flow at cathode side rises again to the normal operating value, as can be checked from the excess of air behavior (Figure 3.7-a).

The residuals computed through this simulation are presented in Figure 3.8. As previously described in Figure 3.6, the blue bars are the residuals values computed with equation (3.1) after the whole system reached the steady state. The threshold values have been chosen equal to the previous ones, that are ±1% (red straight-dot line) and ±5% (green dashed line) of the monitored variables values at normal condition. From

Figure 3.8 it can be observed that the only variables clearly affected by this fault are the blower power (symptom s_2), due to the temperature controlled counteraction, and, consequently, the net electric power (symptom s_3).

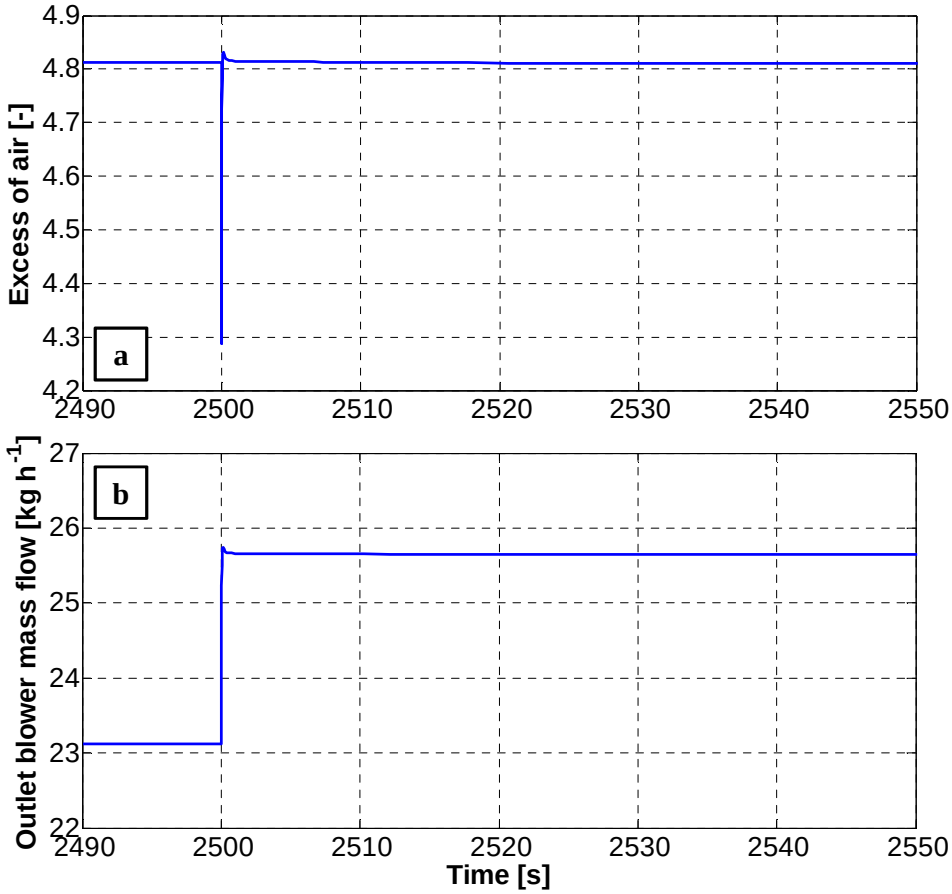

Figure 3.7 Transient variation of the excess of air (a) and increase in the outlet blower mass flow (b) induced by an air leakage between the air blower and the air pre-heater of about 10% of the air mass flow at normal condition.

However, the latter shows a smaller variation compared to that of the blower power, which rises from 0.4629 kW to 0.5163 kW (an increment of about 12%). The comparison of the obtained residuals with the defined

thresholds led to the generation of the two symptoms vectors presented in Table 3.4, where the differences among them and the symptoms vector of the FSM of Table 3.1 are highlighted. It can be observed that the only discrepancy can be found in the symptom vector related to a threshold value of ±5%. Indeed, the percent variation of the net electric power is about -1.9%, thus triggering a symptom only for the ±1% threshold value. This difference is highlighted in Table 3.4 with a gray background for the symptom s_3.

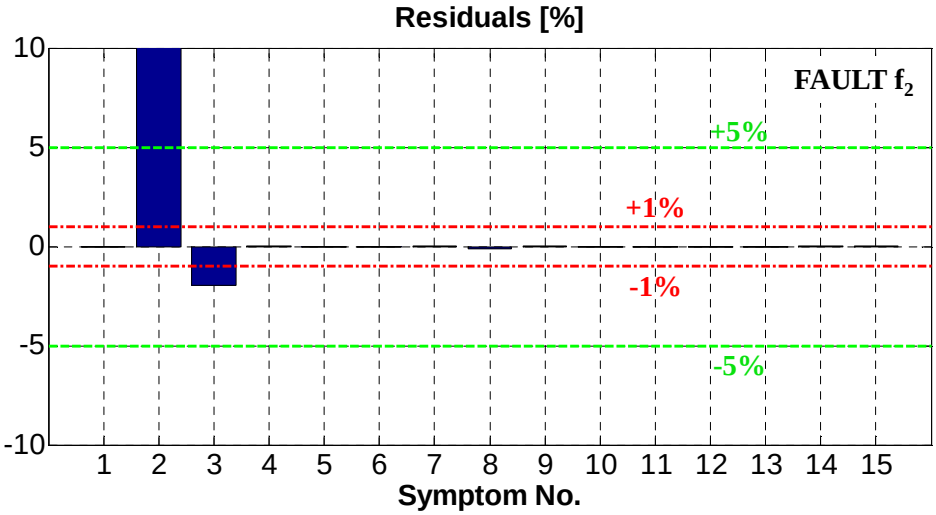

Figure 3.8 Air leakage simulation results: comparison among the residuals and the defined thresholds at ±1% (red straight-dot line) and at ±5% (green dashed line) of the monitored variables obtained for a fault magnitude of 10%.

Table 3.4 Symptoms vectors related to an air leakage of 10% of magnitude obtained for two threshold levels of ±1% and ±5%.

Fault f_2	s_1	s_2	s_3	s_4	s_5	s_6	s_7	s_8	s_9	s_{10}	s_{11}	s_{12}	s_{13}	s_{14}	s_{15}
FSM	0	1	1	0	0	0	0	0	0	0	0	0	0	0	0
τ = 1%	0	1	1	0	0	0	0	0	0	0	0	0	0	0	0
τ = 5%	0	1	0	0	0	0	0	0	0	0	0	0	0	0	0

This result supports the statement that the exploitation of an FSM developed only with a heuristic approach can lead to a non-optimal isolation procedure. Indeed, as explained in the previous paragraphs, the FTA approach considers only qualitative relationships among the variables and the fault. It must be stressed again that if a fault affects a variable, a symptom arises. To achieve a proper isolation on a real system the need for specific threshold levels and the knowledge of a quantitative relationship among faults and symptoms become essential. Moreover, to improve the diagnostic capabilities of the fault detection, especially for incipient faults, the knowledge of measurements noise and model uncertainty is also required.

3.2.3 Fault f_3: temperature controller failure simulation

Differently from the other faults simulated in this work, the temperature controller failure does not require a specific sub-model, as explained in paragraph 2.2.3, but it is induced by switching off the controller block (see Figure 3.4) at a certain time and changing afterwards the required current. In this case, the detection of the fault is performed comparing the variables values obtained after the controller switch off to their expected values (i.e. obtained with the controller switched on) at the new operating condition. In this way, the controller failure can be identified considering the different adaptation of the monitored values. In the specific, the load is changed from 25 A to 40 A. The list of the expected values of the monitored variables at this new operating condition is given in Table 3.5.

The results presented in the following cannot be related to a specific fault magnitude because of its binary nature, i.e. the controller can be either on or off. The amplification of the effects can only be affected by the current step change. The simulation procedure consists in the controller switch off at 2500 s and in the following current increase from 25 A to 40 A. According to what observed in Figure 2.13 and Figure 2.14, the system reaction to a current variation in uncontrolled condition consists in the stack temperature sudden increase, whereas the excess of air remains constant. The same results are here obtained and presented in Figure 3.9. Specifically, in Figure 3.9-a it is possible to appreciate that, as

expected, even though the current request is increased from 25 A to 40 A, the excess of air measured at the stack inlet does not change. Since the air mass flow is evaluated through equation (2.5), the excess of air measured at the stack inlet remains the one imposed for the previous operating condition. On the other hand, the stack temperature increases from 825°C to 849.4°C (Figure 3.9-b), which corresponds to a variation of 2.2%. Additionally, from the same picture we can observe that the stack temperature exhibits the same dynamic transient as the one showed in Figure 2.13, further confirming that the whole system behaves in uncontrolled condition.

Table 3.5 Monitored variables values for the second reference operating condition: the current request is set to 40 A and the other model parameters values are chosen according to those of Table 2.1.

No.	Variable	Value	Unit
s_1	stack gross power	4.3095	kW
s_2	blower absorbed power	0.7696	kW
s_3	net electric power	3.5399	kW
s_4	stack temperature	825.00	°C
s_5	excess of air	5.1908	-
s_6	fuel temperature at anode inlet	707.64	°C
s_7	post burner exhaust temperature	1050.2	°C
s_8	air temperature at blower outlet	82.68	°C
s_9	hot fluid temperature at air pre-heater inlet	856.28	°C
s_{10}	air temperature at cathode inlet	683.63	°C
s_{11}	current density	0.4	A cm^{-2}
s_{12}	stack voltage	107.74	V
s_{13}	air mass flow at cathode inlet	39.911	kg h^{-1}
s_{14}	temperature at anode outlet	825.00	°C
s_{15}	air temperature at cathode outlet	825.00	°C

In Figure 3.10 the comparison of the computed residuals with two threshold levels of ±1% (red straight-dot line) and ±5% (green dashed line) of the monitored variables values of Table 3.5 is presented. From this representation, we can straightway observe that all the residuals but two diverge from zero. The excess of air (symptom s_5) is lower than its

expected value, because it remains equal to 4.812 instead of rising to 5.1908, leading to a residual of -7.3%. As previously observed, the stack temperature residual (symptom s_4) grows, reaching a steady state value of +2.2%. In line with the statements done in reference to Figure 2.12, the stack voltage value in uncontrolled condition is higher than that in controlled condition. For this reason, the related residual (symptom s_{12}) shows a drift of +4%.

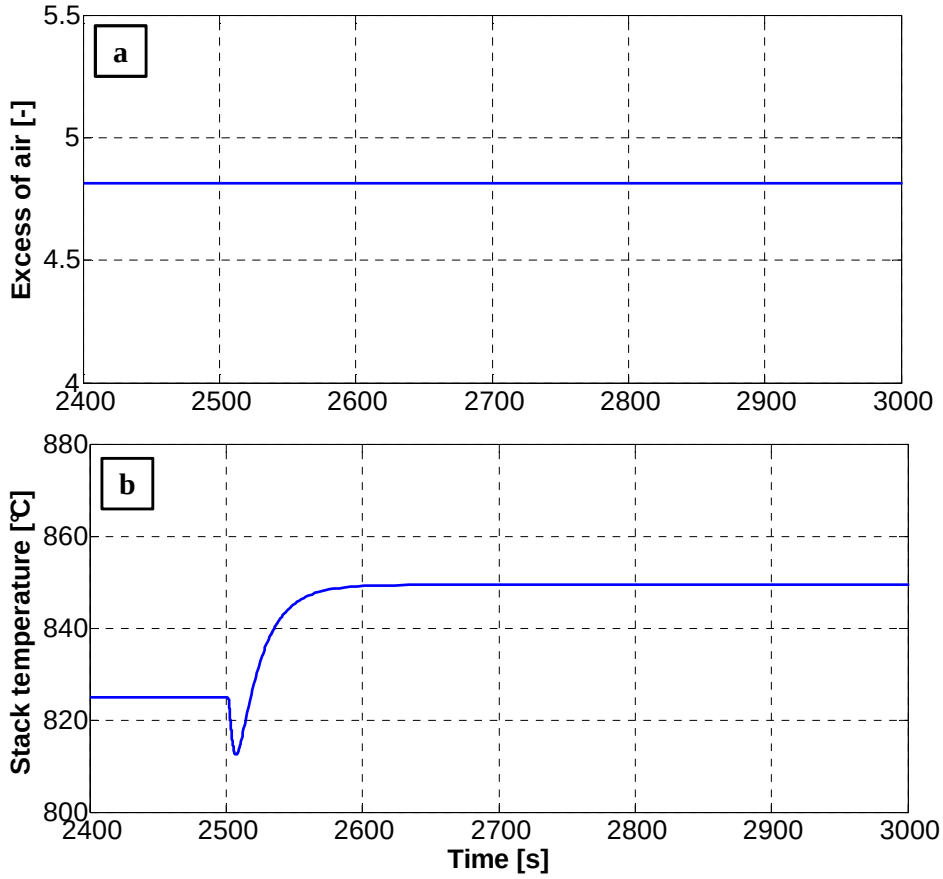

Figure 3.9 Excess of air (a) and stack temperature (b) responses to a current variation from 25 A to 40 A: their behavior clearly prove that the system is operating in uncontrolled conditions, as it can be seen from the results in Figure 2.13 and Figure 2.14.

Another relevant effect consists in the blower power reduction compared

to that expected for a current request of 40 A. In controlled condition, the blower power is almost 0.77 kW (see Table 3.5), whereas in uncontrolled condition it reaches only 0.72 kW, with a difference of nearly -6.5% (symptom s_2 in Figure 3.10). This variation is induced by the lower excess of air, which directly affects the air mass flow through equation (2.5), as done by the current request $J \cdot A_{SOFC}$, and thus the blower power with equation (2.7). Moreover, the air mass flow reduction with respect to that expected for a current of 40 A is represented by the related residual (symptom s_{13}), which exhibits a value of -7.3%.

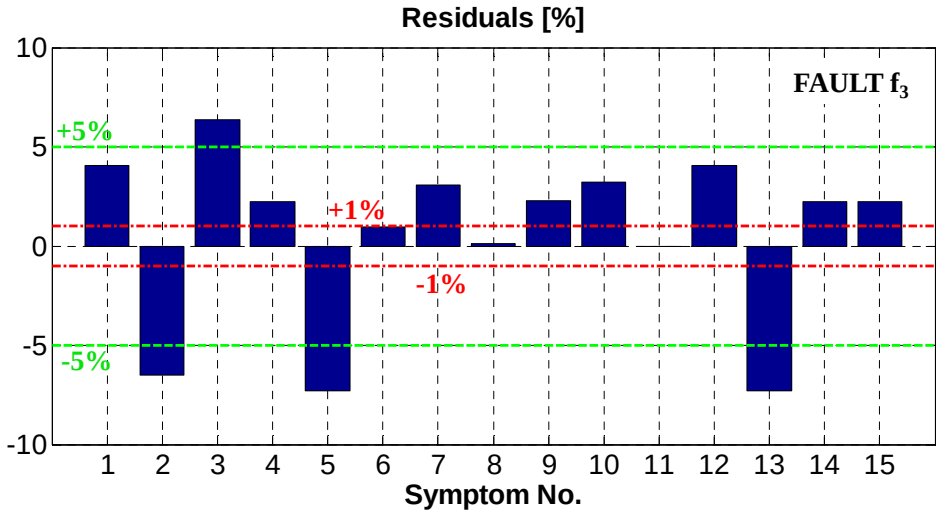

Figure 3.10 Temperature controller failure simulation results: comparison among the residuals and the defined thresholds at ±1% (red straight-dot line) and at ±5% (green dashed line) of the monitored variables referred to a load request of 40 A and to the steady state reference values of Table 3.5.

The symptoms vectors related to the residuals of Figure 3.10 are showed in Table 3.6 referring to two thresholds levels of ±1% and ±5%. Even in this case, the differences among them and the symptoms vector of the FSM of Table 3.1 are represented with a gray cell background color.

Table 3.6 Symptoms vectors related to a temperature controller failure obtained for two threshold levels of ±1% and ±5%.

Fault f_3	s_1	s_2	s_3	s_4	s_5	s_6	s_7	s_8	s_9	s_{10}	s_{11}	s_{12}	s_{13}	s_{14}	s_{15}
FSM	1	0	1	1	0	1	1	0	1	1	0	1	0	1	1
τ = 1%	1	1	1	1	1	0	1	0	1	1	0	1	1	1	1
τ = 5%	0	1	1	0	1	0	0	0	0	0	0	0	1	0	0

What emerges from this comparison is that both the two new symptoms vectors show several discrepancies. First of all, the fuel temperature at anode inlet (symptom s_6) becomes 0 in both cases. This difference is due to its residual value lower than 1%. However, the substantial differences belong to the blower absorbed power (symptom s_2), the excess of air (symptom s_5) and the air mass flow at cathode inlet (symptom s_{13}), which become all 1. The explanation could reside in the controller fault simulation process. Compared to the detection based on the FTA of Arsie et al. [4], the simulation entails a current demand variation, which is not considered by the FTA in [4]. The other differences, showed only by the symptoms vector for $\tau = \pm 5\%$, are due to the related low residuals values.

3.2.4 Fault f_4: fuel pre-reformer fault simulation

The pre-reformer heat exchange surface corrosion is simulated reducing the characteristic pre-reformer surface A_{ref} according to equation (2.33). As explained in paragraph 2.2.4, this event directly affects the pre-reformer outlet cold fluid temperature (see equation (2.17)), used as the reference pre-reformer temperature for the computation of the outlet fuel composition through equation (2.15). Differently from the other simulations, the fault magnitude is chosen equal to 50%, due to the small impact of this specific event on the obtained residuals values, as showed in the following. The fault coefficient χ is risen from 0 to 0.5 at 2500 s, causing a reduction in A_{ref} from 0.06 m^2 to 0.03 m^2.

As a result, the pre-reformer temperature (i.e. outlet cold fluid temperature) instantly decreases at a steady state value of 604.41°C,

which is about 9.8% less than the reference temperature (Figure 3.11-a). This reduction causes a variation into the outlet fuel composition, as showed in Figure 3.11-b, where the hydrogen molar flow variation is depicted.

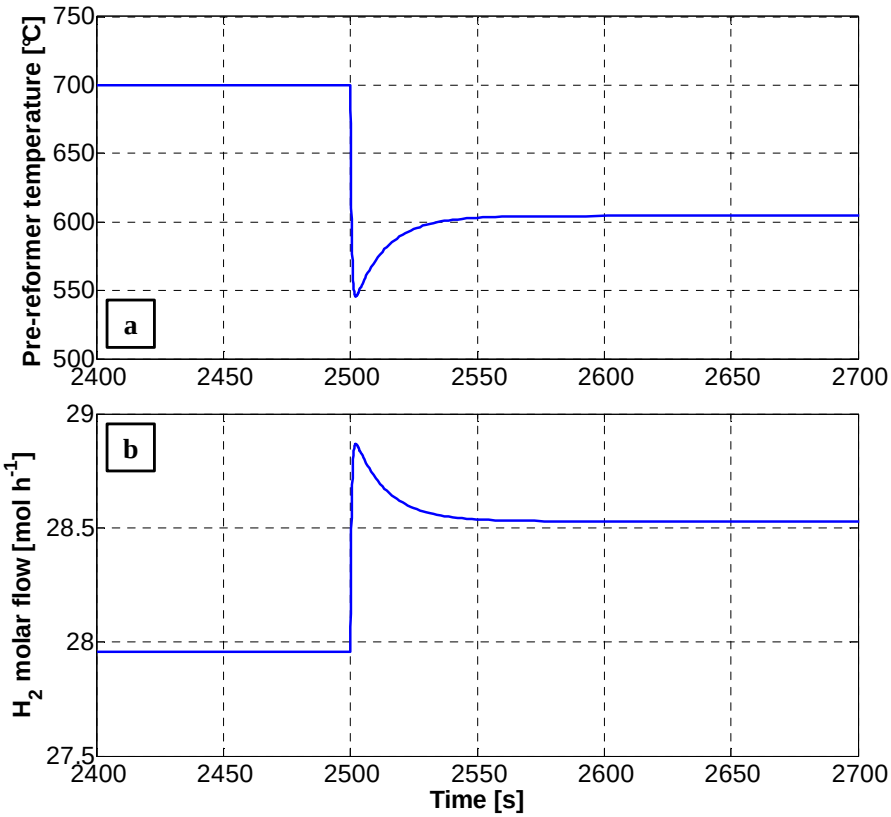

Figure 3.11 Pre-reformer reference temperature decrease (a) and hydrogen molar fraction variation (b) induced by a reduction in the pre-reformer surface of about 50%.

The resulting residuals for this simulation are represented as blue bars in Figure 3.12. As already stated, only the fuel temperature at anode inlet (symptoms s_6) is substantially affected by this fault, whereas all the other residuals are quite small, even though the fault magnitude is 50% (which can be barely considered related to an incipient fault).

The reduction in the temperature at the anode inlet causes a drop in the stack temperature (symptom s_4), which is compensated by the decrease of the inlet air mass flow (symptom s_{13}) imposed by the controller, with a consequent variation of the blower power (symptoms s_2) and the increase in the air temperature at cathode inlet (symptom s_8).

In Table 3.7 the two symptoms vectors obtained comparing the residuals values to two threshold levels of ±1% and ±5%, represented in Figure 3.12 with a pair of red straight-dot lines and a pair of green dashed lines respectively, are presented.

Concerning the symptom vector for a threshold level of ±1%, four symptoms change from 1 to 0: the blower power (symptom s_2), the excess of air (symptom s_5), the post-burner exhaust temperature (symptom s_7) and the air mass at cathode inlet (symptom s_{13}).

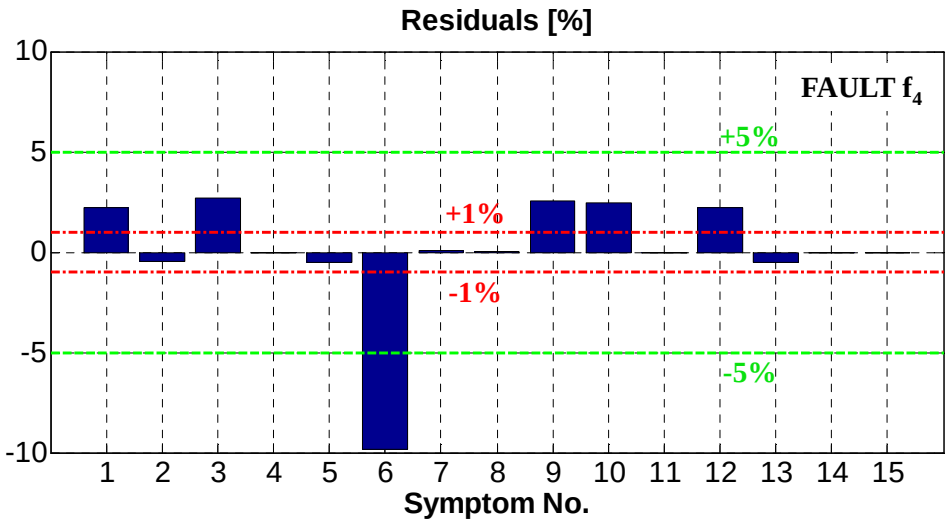

Figure 3.12 Fuel pre-reformer fault simulation results: comparison among the residuals and the defined thresholds at ±1% (red straight-dot line) and at ±5% (green dashed line) of the monitored variables obtained for a fault magnitude of 50%.

Nonetheless, the only significant difference resides in the post-burner exhaust temperature, which seems not to be affected by this fault, whereas all the other differences are due to the low residuals values. Actually, the post-burner exhaust temperature increases only by less than 1°C, resulting

in a residual near zero. This effect can be justified by the fact that the stack temperature is kept constant and the variation in the fuel composition has a negligible influence on the post-burner inlet molar flow.

Table 3.7 Symptoms vectors related to a pre-reformer fault of 50% of magnitude obtained for two threshold levels of ±1% and ±5%.

Fault f_4	s_1	s_2	s_3	s_4	s_5	s_6	s_7	s_8	s_9	s_{10}	s_{11}	s_{12}	s_{13}	s_{14}	s_{15}
FSM	1	1	1	0	1	1	1	0	1	1	0	1	1	0	0
τ = 1%	1	0	1	0	0	1	0	0	1	1	0	1	0	0	0
τ = 5%	0	0	0	0	0	1	0	0	0	0	0	0	0	0	0

The same conclusions can be extended also to the other symptoms vector (i.e. ±5% threshold level), which shows five more symptoms being zeroed. These results help again remarking the importance of a quantitative study for the development of a diagnostic algorithm to be applied to a real system.

3.2.5 Fault f_5: stack fault simulation

The last fault considered in this study involves the SOFC stack in terms of increase in its ohmic resistance. As exposed in section 2.2.5, to simulate this undesired event the stack voltage evaluated through equation (2.2) is reduced according to the coefficient ε (see equation (2.34)), which represents the fault magnitude. Even for this fault the considered magnitude level is 10%, which means that the ε is set equal to 0.1, so as to observe the system response to an incipient fault.

The direct effect of this fault is the sudden drift of the stack voltage from 115.82 V, reaching at steady state a value of 102.14 V, as presented in Figure 3.13-a. This reduction exceeds the 10%, which is the fault magnitude level, and the motivation can be found in the strong interaction among each system component. Indeed, the stack voltage decrease affects the stack temperature through equation (2.1), reducing the electric power

generation and, thus, leading to a temperature increase. To restrain the temperature drift, the controller reacts increasing the excess of air demand, as showed in Figure 3.13-b. This latter rises from 4.8124 to 5.5031 at steady state, with a variation of more than 14%. The related effects comprise the increase in the air mass flow and in the blower power.

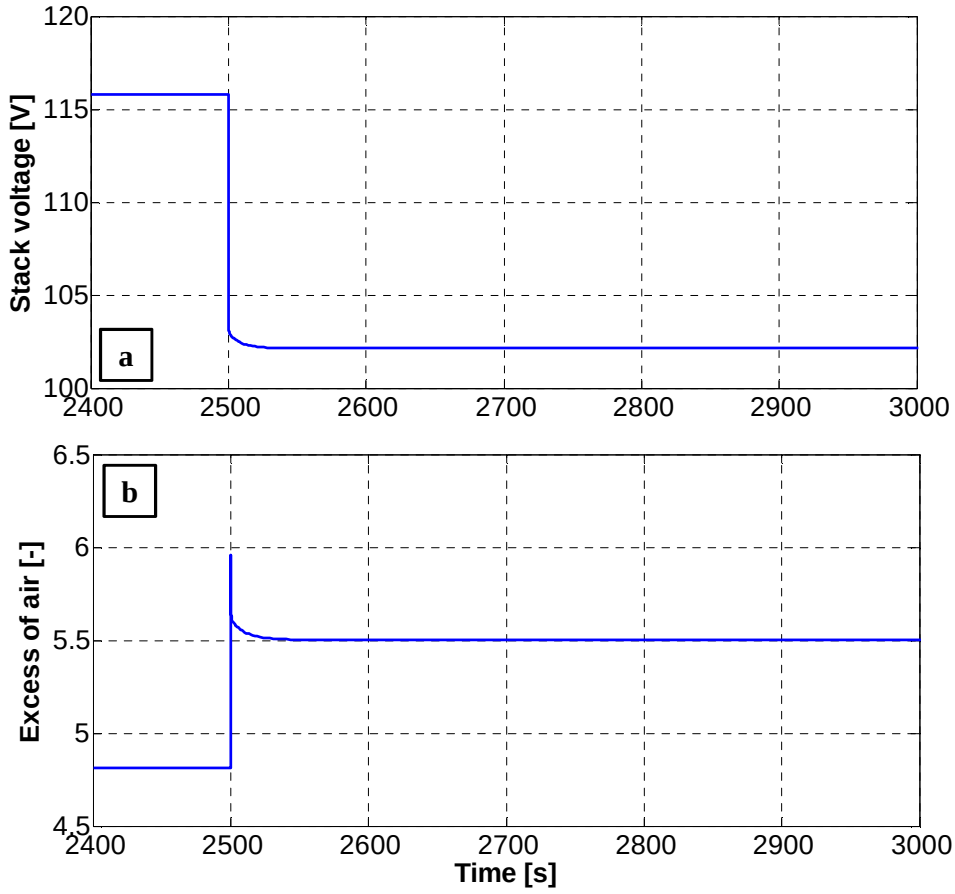

Figure 3.13 Stack voltage reduction (a) and increase in the excess of air (b) caused by a growth in the stack ohmic resistance by 10%.

The residuals associated to this fault are presented in Figure 3.14 as blue bars, in comparison with two threshold levels of ±1% (red straight-dot line) and at ±5% (green dashed line). The effects previously described are

here highlighted. The most evident variations are related to the stack power (symptom s_1), the blower absorbed power (symptom s_2), the net electric power (symptom s_3), the excess of air (symptom s_5), the stack voltage (symptom s_{12}) and the air mass flow at cathode inlet (symptom s_{13}). Only the stack temperature (symptom s_4), the temperatures at the cathode and anode outlet (symptoms s_{14} and s_{15} respectively) are not affected by the occurrence of this fault. Moreover, also the stack current density (symptom s_{11}) shows a residual equal to zero, as expected, because the stack voltage fault does not involve the electrochemical active area and the current request is kept constant.

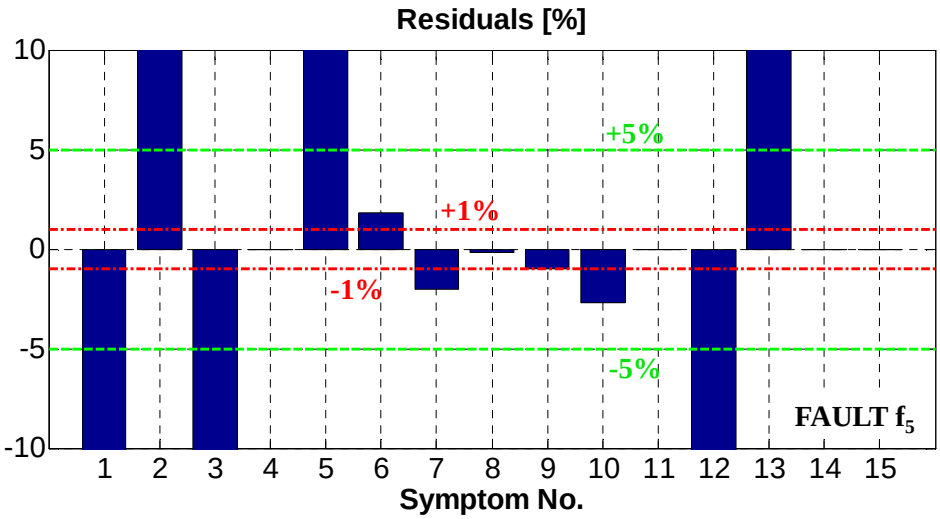

Figure 3.14 Stack fault simulation results: comparison among the residuals and the defined thresholds at ±1% (red straight-dot line) and at ±5% (green dashed line) of the monitored variables obtained for a fault magnitude of 10%.

The symptoms vectors generated from the previous residuals are exposed in Table 3.8. What immediately leaps out is that only the symptoms vector related to a threshold level of ±1% matches perfectly the one of the starting FSM. The symptoms vector related to a threshold level of ±5%, shows, instead, four symptoms being zeroed. However, this difference is only due to the small residuals values related to those monitored variables.

Table 3.8 Symptoms vectors related to a stack fault of 10% of magnitude obtained for two threshold levels of ±1% and ±5%.

Fault f_5	s_1	s_2	s_3	s_4	s_5	s_6	s_7	s_8	s_9	s_{10}	s_{11}	s_{12}	s_{13}	s_{14}	s_{15}
FSM	1	1	1	0	1	1	1	0	1	1	0	1	1	0	0
τ = 1%	1	1	1	0	1	1	1	0	1	1	0	1	1	0	0
τ = 5%	1	1	1	0	1	0	0	0	0	0	0	1	1	0	0

3.2.6 Summary of the faults simulation results

The faults simulation results described in the previous paragraphs can be summarized into two different FSMs, one related to the threshold level of ±1% and the other related to the threshold level of ±5%. These improved FSMs are presented in Table 3.9 and Table 3.10 respectively. In these matrixes, the differences with the starting FSM of Table 3.1 are again highlighted with a gray cell background.

Concerning the FSM of Table 3.9, the first observation which can be made is that all the rows are different from each other, allowing the univocal identification of the considered faults, which cannot be performed with the starting FSM. Furthermore, only two rows are rather modified (fault f_3 and fault f_4), whereas other two are kept unchanged (fault f_2 and fault f_5). The last comment concerns the current density (symptom s_{11}) column, which shows all zeroes. This result is motivated by two reasons: first, the current request is an input of the model and, second, all the considered faults do not affect the electro-active area A_{SOFC}. These two conditions imply a current density always equal to the one expected for each operating condition. For this reason, this variable can be cleared from the FSM because it is no more useful for the isolation process.

The FSM of Table 3.10 is instead quite different from the starting FSM. All the rows have been changed with respect to the FSM of Table 3.1. Only one row (fault f_2) has only one symptom changed, whereas all the others present at least three different symptoms values. Moreover, the rows associated to the faults f_1 and f_2 present the same pattern hindering

the possibility to exploit this FSM for an accurate isolation procedure.

Table 3.9 Improved FSM obtained for a threshold level of ±1%.

$\tau = 1\%$	s_1	s_2	s_3	s_4	s_5	s_6	s_7	s_8	s_9	s_{10}	s_{11}	s_{12}	s_{13}	s_{14}	s_{15}
f_1	0	1	1	0	0	0	0	1	0	0	0	0	0	0	0
f_2	0	1	1	0	0	0	0	0	0	0	0	0	0	0	0
f_3	1	1	1	1	1	0	1	0	1	1	0	1	1	1	1
f_4	1	0	1	0	0	1	0	0	1	1	0	1	0	0	0
f_5	1	1	1	0	1	1	1	0	1	1	0	1	1	0	0

Table 3.10 Improved FSM obtained for a threshold level of ±5%.

$\tau = 5\%$	s_1	s_2	s_3	s_4	s_5	s_6	s_7	s_8	s_9	s_{10}	s_{11}	s_{12}	s_{13}	s_{14}	s_{15}
f_1	0	1	0	0	0	0	0	0	0	0	0	0	0	0	0
f_2	0	1	0	0	0	0	0	0	0	0	0	0	0	0	0
f_3	0	1	1	0	1	0	0	0	0	0	0	0	1	0	0
f_4	0	0	0	0	0	1	0	0	0	0	0	0	0	0	0
f_5	1	1	1	0	1	0	0	0	0	0	0	1	1	0	0

In conclusion, the results here presented highlight the importance of the quantitative evaluation of the relationships among faults and symptoms, especially when facing real system applications. Indeed, the investigation of the real faults effects on the monitored variables allowed to overcome the redundancy problem in the FSM of Table 3.1 (see faults f_4 and f_5) imposing a threshold level of ±1%. It has been also proved that the isolation accuracy is strictly related to the assumed thresholds: the exploitation of measurement devices with high noise levels or the utilization of a low accuracy model drive the choice towards high threshold levels, hindering sometimes the univocal isolation of single faults. Moreover, according to [10] and [62], a statistical analysis can

improve the effectiveness of any diagnostic methodology when applied to real systems, coupled with measurement devices with low accuracy (i.e. high noise). For this reason, a statistical hypothesis test has been considered for the implementation of the algorithm on a real system, as will be presented in Chapter 5.

CHAPTER 4 Experimental Activity

The improved FSM development process described in the previous chapter closes the diagnostic algorithm design procedure. Clearly, once the whole algorithm is assembled, a dedicated experimental activity is required for the characterization and the validation of the diagnostic algorithm, before its application on the system. Indeed, a preliminary experimental characterization allows the understanding of which actions must be performed to adapt the algorithm (which still presents “generic” features) to the system under study.

As mentioned in Chapter 1, the experimental activity presented in this chapter and the validation procedure exposed in the next one have been performed within the framework of the European project GENIUS [49]. More in details, a pre-commercial micro Combined Heat and Power (μ-CHP) SOFC system, the Galielo 1000N, manufactured by the Swiss company HEXIS AG [52] (one of the industrial partners of the GENIUS project), has been experimentally characterized to understand which variables can be monitored, both offline and online, and which kind of faults can be induced in controlled mode. Therefore, the design of specific procedures to mimic experimentally controlled faults on the real system can be considered one of the main novelties of the presented work.

In the next paragraph a brief presentation of the Galileo 1000N and the test bench setup of the EIFER’s fuel cell laboratories is given. Then, the procedure and the hardware modifications, required for the experimental induction of the considered faults, are illustrated in details. It is worth noting that the presented activity has been part of a larger experimental plan, illustrated in more details in Chapter 7.

The entire experimental activity has been accomplished in a close collaboration among the University of Salerno, the European Institute for Energy Research (EIFER) and the HEXIS AG company.

4.1 The Galileo 1000N system and the experimental test bench

The Galileo 1000N system is a µ-CHP generation system, whose picture is presented in Figure 4.1-a. This system is based on an SOFC stack characterized by 65 cells with 100 cm^2 active area each [54]. A scheme of the main components, the mass and the energy flows is illustrated in Figure 4.1-b. On one hand, the inlet fuel flow (i.e. Natural Gas) is provided from an external grid and it flows through two desulphurizing units before entering the catalytic partial oxidizer (CPO) to obtain the hydrogen amount required for the cells electrochemical reaction. On the other hand, the air flow is regulated by a dedicated blower. The gas mixture leaving the CPO reaches directly the SOFC stack at anode side, whereas the air flow at the cathode side is regulated by the exhaust blower.

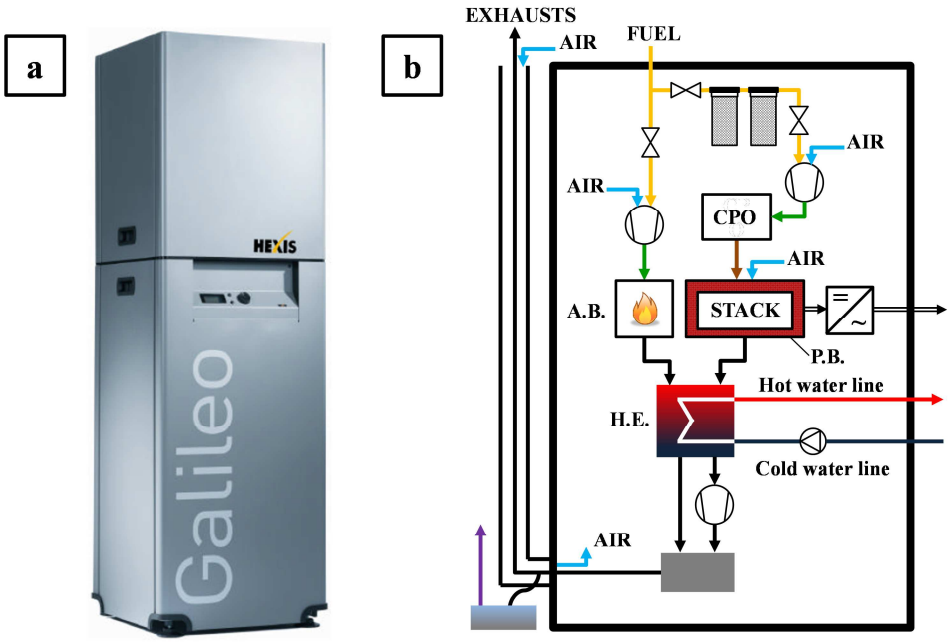

Figure 4.1 Galileo 1000N system picture (a) and scheme (b), adapted from [54].

The produced electric energy is converted by a DC/AC converter before reaching the electric grid. The reacted gases leave the stack before being mixed and burned into a post-burner chamber (P.B.), which surrounds the stack, to keep the stack at the required temperature. The burned gases are then driven into a gas-liquid heat exchanger (H.E.), which provides the required amount of heat to the external user. If the produced thermal power is less than the requested one, an additional burner (A.B.) can provide a further amount of hot gases. The total amount of hot fluid enters the heat exchanger and delivers the required thermal power to the cold liquid line (usually water). The flue gases are then sent to a condenser before leaving the system.

The Galileo 1000N stack is controlled in potentiostatic mode and under nominal operating conditions it delivers 1 kW (AC) electric and 2.5 kW thermal power, which can be increased to 23 kW with the additional burner [53][54]. A dedicated test bench has been setup at the EIFER fuel cell laboratories to ensure the correct fulfillment of the experimental characterization of the Galileo 1000N system. A flow chart of the EIFER test bench is provided in Figure 4.2. It has a natural gas supply line, whose flow is controlled with a solenoid and a shut-off valve, and sensors for energy and power monitoring. The inlet air is filtered and characterized through temperature and flow rate sensors. The only output gas is the flue gas released by the Galileo 1000N, which is sent through a water trap and then to a ventilation system. The thermal load is regulated by means of a heating loop, in order to dissipate the generated thermal power. It plays the role of the final user, through a liquid-liquid heat exchanger. The hot liquid coming from the Galileo 1000N is regulated by an internal intermitted pump, whereas the cold liquid, entering the heat exchanger on the other side with respect to the hot fluid, comes from a pressurized cooling water line and is regulated through a valve.

The output electric power generated by the Galileo 1000N is directly fed to the electric grid since the system has an integrated DC/AC converter. The net electric power is measured by a dedicated power monitoring system, as shown in Figure 4.3, where a picture of the test bench, with the Galileo 1000N and some of the other aforementioned components, is given.

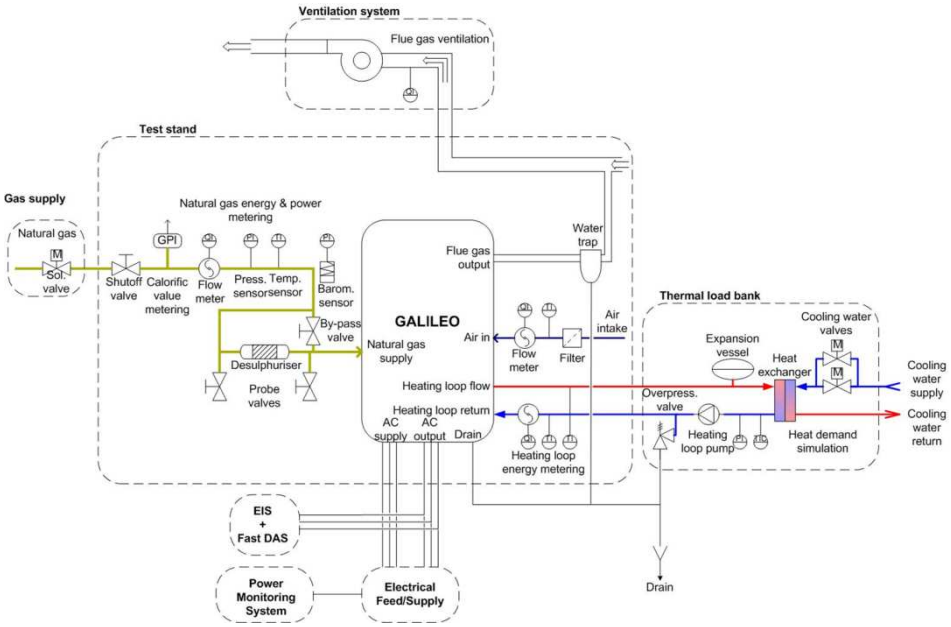

Figure 4.2 EIFER test bench flow chart dedicated to the Galileo 1000N system testing [53].

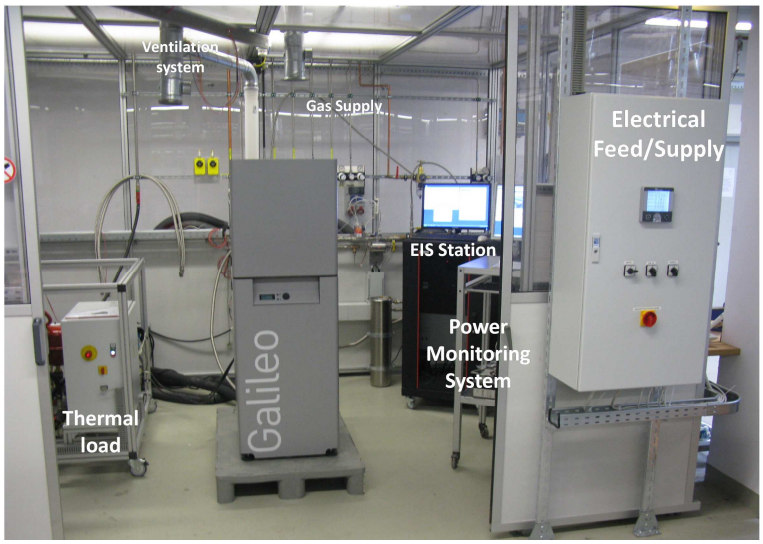

Figure 4.3 Picture of the EIFER test bench dedicated to the Galileo 1000N system testing [53].

The Galilo 1000N is controlled and regulated through a dedicated software, the HexisView, developed by the HEXIS AG company, installed on a standard PC directly connected to the system [54]. This software allows the regulation of the system set-points and other controlled variables and gives useful information about the system status. In addition, the EIFER test bench is provided with other dedicated measurement devices controlled by LabVIEW® [53].

4.2 Experimental faults design and system modifications

To validate the diagnostic algorithm developed in the present work, a set of controllable faulty states to be experimentally induced on the Galileo 1000N must be defined. According to those presented in the previous chapters, the following faults are considered:

- *Fault f_1*: increase in blower mechanical losses;
- *Fault f_2*: leakage;
- *Fault f_3*: temperature controller failure;
- *Fault f_4*: CPO surface degradation;
- *Fault f_5*: stack ohmic resistance increase;

It is worth noting that the faults listed above have been chosen with respect to those accounted for the diagnostic algorithm development and considering what was actually feasible on the system. Moreover, the induction of the aforementioned faults required also the understanding of the system controller behavior. As the PI controller described in Chapter 2, the Galileo 1000N controller keeps the stack temperature near the set-point value acting on the exhaust blower power to regulate the inlet cooling air flow. This information has been of primary importance for the diagnostic algorithm adaptation procedure, explained in the next chapter. Coming to the details of the fault induction process, two faults (the leakage – fault f_2 – and the ohmic resistance increase – fault f_5) required a modification of the system hardware, whereas the remaining three are mimicked by acting on the system via the HexisView software.

The increase in blower mechanical losses is mimicked switching on some electrical heaters surrounding the stack, located nearby the system air intakes, which allow to raise the inlet air temperature. The growth of the air temperature is one of the considered effects of this specific fault, as described in paragraph 2.2.1 and paragraph 3.2.1, and it induces the exhaust blower to adapt to the new condition.

The second fault consists in a gas leakage at the stack outlet. The fault location is chosen according to the system configuration and specific mechanical constrains. Indeed, for its implementation, some hardware modifications have been required: a valve between the stack and the gas-liquid heat exchanger has been installed, as shown in Figure 4.4. To install this valve, a hole has been drilled right after the stack exhausts

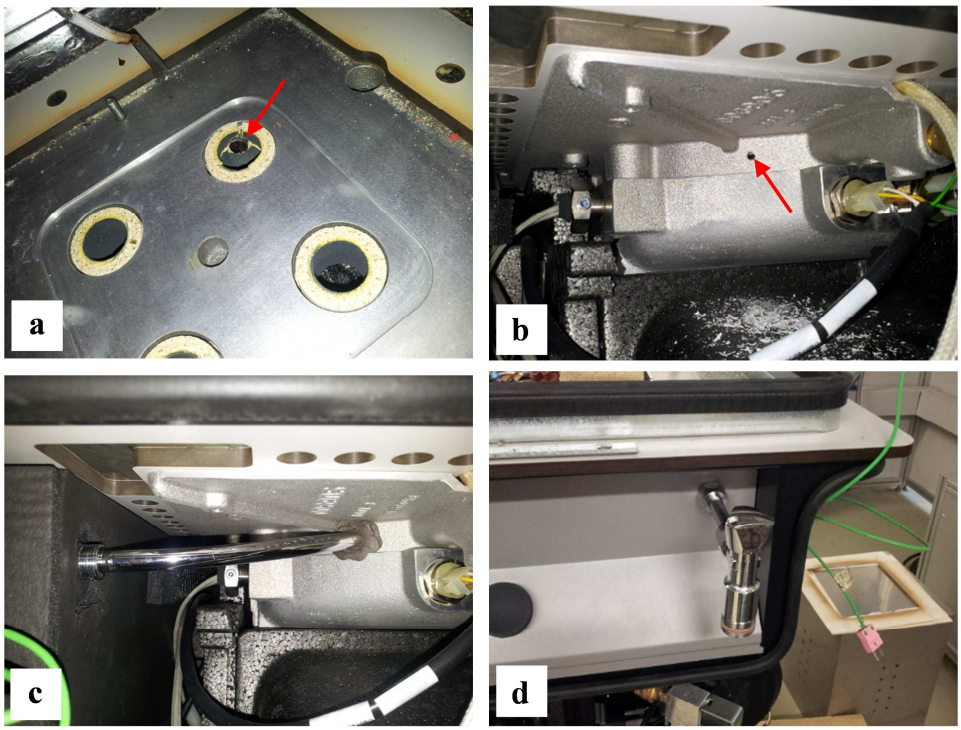

Figure 4.4 Installation phases of the leakage valve: drilled hole view from the inside exhaust duct (at stack outlet) (a) and from the outside (b); pipe connection (c) and faucet (d).

A clear view of the drilled hole is given in Figure 4.4-a and Figure 4.4-b. The first picture offers a top view of the exhaust duct inside, visible only upon removal of the stack and CPO block, whereas an external view is proposed in the second one. In both the pictures the hole is clearly visible and its location is highlighted with a red arrow. The hole has been then connected with a metallic pipe, showed in Figure 4.4-c, to the faucet (Figure 4.4-d), required for the control of the leakage amount.

The temperature controller failure is mimicked only through software maneuvers. In this case, the temperature controller is disabled switching the exhaust blower control logic from automatic to manual and changing its operating set-point in order to reach another operating condition. This procedure is along the lines of the one defined in paragraph 2.2.3 and 3.2.3, where the controlled failure is detected upon change in the system operating condition.

As the previous one, also the CPO fault is induced only through software maneuvers. To mimic the CPO surface degradation the characteristic oxygen to carbon ratio λ_{CPO} is varied with respect to its normal operating value. The direct consequence of this maneuver consists in the variation of the outlet fuel composition and thus in its energy content, as assumed in paragraph 2.2.4 and paragraph 3.2.4.

The last fault considered in this experimental activity concerns the ohmic resistance increase of the Galileo 1000N stack. Due to the several constrains which limited the technical actions for the fault design, some hardware modifications have been again required. These restrictions also drove the fault choice to this specific one, rather than the surface active area reduction, justifying the FSM changes presented in paragraph 3.1.2. Since the inside part of the SOFC stack is not accessible, a resistance box has been built in-house and inserted between the stack and the inverter on the positive terminal. The utilization of this box mimics the same effects considered for the fault simulation sub-model presented in paragraph 2.2.5. A simplified scheme of the box structure is sketched in Figure 4.5, whereas a picture of the external connections and the internal resistances are given in Figure 4.6-a and Figure 4.6-b respectively. More in details, the maximum resistance which can be added in series to the stack should not exceed 100 mΩ. Furthermore, to avoid abrupt changes, the electric box has been equipped with a manual switch so as to change the stepwise variation of the resistance by 20 mΩ each step. Indeed, this latter value represents the value of the single electric resistance, which allows the

utilization of a maximum of five resistances in series, as shown in Figure 4.5 and Figure 4.6-b. Moreover, a dedicated ventilation system has been sized in order to ensure the required heat dissipation.

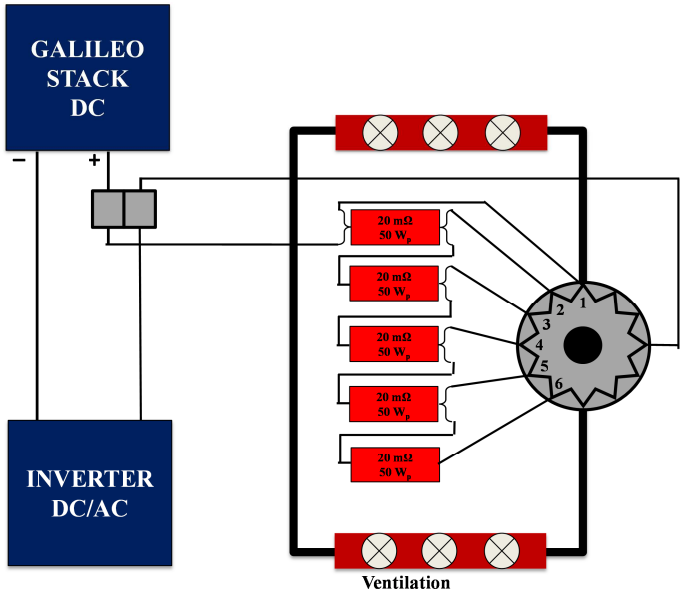

Figure 4.5 Electric resistance box scheme [53].

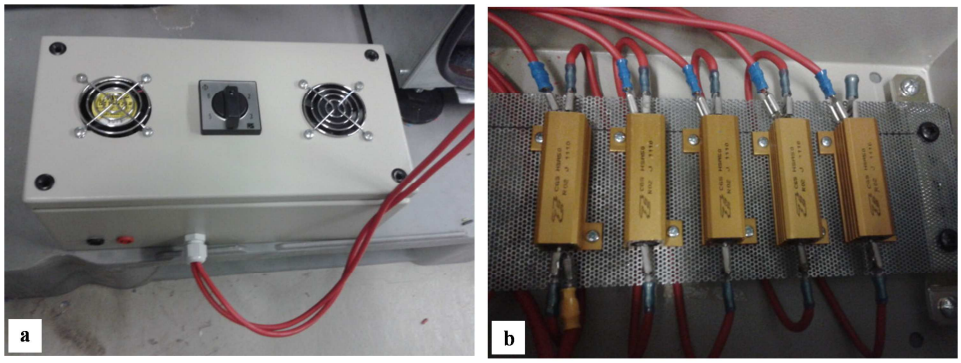

Figure 4.6 External connections (a) and internal resistances configuration (b) of the manufactured electric resistance box [53].

4.3 Experimental faults induction results

The faults described in the previous paragraph have been induced on the Galileo 1000N system in a controlled way, so as to understand the system response to specific faults magnitudes and to properly manage the system behavior to avoid its abrupt failure.

The results here presented are exploited in the next chapter for the validation procedure of the diagnostic algorithm developed in this work. In the following a brief description of the system response to the induced faults is given, with particular attention to the variables expected to be mainly affected by the undesired events. It is worth highlighting that the considered variables are chosen among those measured by the HexisView software. Indeed, this choice is motivated by the need for defining a set of monitored variables among those currently available on the system, to allow an effective on-line application of the diagnostic algorithm, as explained in the next chapter.

4.3.1 Blower fault induction results

The first fault consists in the induction of the effects related to an increase in the blower mechanical losses by turning on electrical heaters surrounding the stack and located at the cold air inlet. The aim of this approach was to reproduce the same theoretical effects of this fault, illustrated in paragraph 3.2.1, since no direct modification of the blower efficiency was achievable. The induction procedure basically consists of two steps: i) the heaters are manually switched on through the HexisView control panel and then ii) their power is gradually increased up to 20% of its maximum value.

An example of the effects of this maneuver on the two main influenced system variables is given in Figure 4.7. From this picture it is possible to observe that the exhaust blower power (expressed as a percentage of its maximum value) increases. This effect can be linked to the inlet air temperature growth, which leads to an increment in the stack temperature, regulated by the controller which, in turn, acts on the blower power.

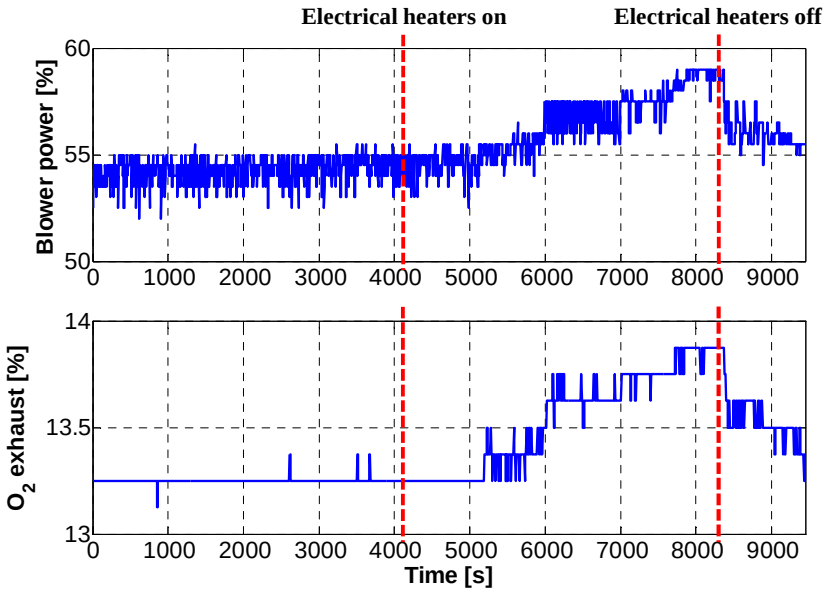

Figure 4.7 Exhaust blower power and O_2 exhaust concentration response to the blower fault induction: once the electrical heaters at the air inlet are switched on the exhaust blower power increases, inducing a small increment also in the O_2 exhaust concentration.

Moreover, the increase in the exhaust blower power induces also an increment in the O_2 exhaust concentration, meaning that also the air flow is affected by this fault. However, this effect is limited and in line with the results carried out in paragraph 3.2.1.

4.3.2 Leakage induction results

The second fault entails a leakage induced by means of the valve represented in Figure 4.4, which allows the control of the leakage amount to avoid system abrupt failure due to substantial variables drifts from the safe region. The induction procedure is quite simple: once the system is in steady state the faucet is gradually opened up to the maximum. The effects of this maneuver are depicted in Figure 4.8, where both the exhaust blower power and the O_2 exhaust concentration are analyzed.

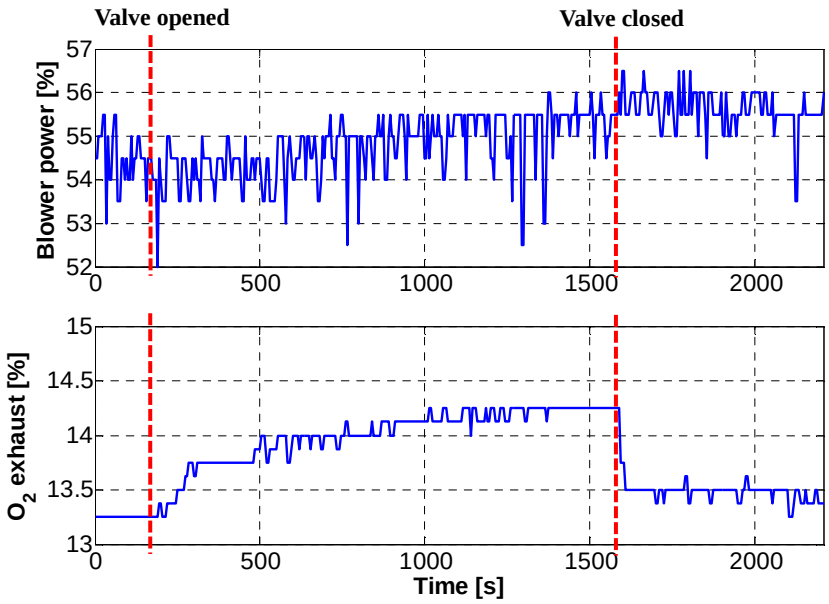

Figure 4.8 Exhaust blower power and O_2 exhaust concentration response to the leakage induction: the opening of the leakage valve induces a slow increase in the exhaust blower power, whereas the O_2 exhaust concentration reacts faster both at the valve opening and closing.

The faucet opening induces a reduction in the air flow at the stack inlet, with a consequent stack temperature increase. However, this increment is controlled through an increase in the blower power and a resulting growth in the air flow. Since the faucet is located at the stack outlet, a direct effect on the O_2 concentration measurement is visible.

It is clear from Figure 4.8 that both the exhaust blower power and the O_2 exhaust concentration rise once the faucet is opened. However, the exhaust blower power increment is slower and less evident than that of the O_2 exhaust concentration, and, due to the slow system thermal dynamics, the effects are still noticeable after a while due to the controller actions.

4.3.3 Controller failure induction results

The induction of the temperature controller failure is performed following a precise maneuver, made only through the HexisView control panel, which is characterized by two consecutive steps: i) first, the exhaust blower control logic is manually switched from automatic (i.e. temperature controller enabled) to manual (i.e. temperature controller disabled), and then ii) the exhaust blower power operating set-point is changed by increasing its speed, so as to reach another operating condition (following a similar approach to that described in paragraph 2.2.4). The main effects of this fault are represented in Figure 4.9, where the stack temperature and the stack power behaviors are sketched.

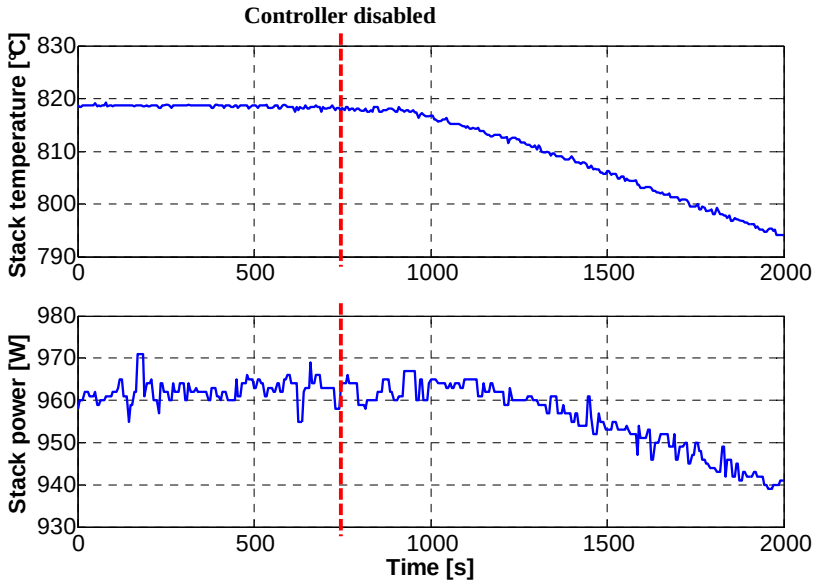

Figure 4.9 Stack temperature and stack power response to the controller failure induction: once the controller is disabled, both the stack temperature and the stack power clearly diverge.

Once the exhaust blower set-point is changed, the system controller cannot keep anymore the stack temperature within the defined boundaries, with a consequent cooling down of the SOFC stack and a sudden gross

power decrease. It is worth noting that, since the temperature controller is kept disabled, the system is not able to reach a steady state and its variables drift with a constant rate from the normal operating condition.

4.3.4 CPO fault induction results

As explained in paragraph 4.2, the induction of the CPO surface degradation is performed mimicking its effects through the stepwise variation of the oxygen to carbon ratio set-point. This choice is mainly motivated by the inability to access the CPO internal structure. Thus, the only way to reproduce the same effects of this fault resides in the variation of the λ_{CPO} set-point, which, in turn, affects the outlet fuel composition and its energy content. In Figure 4.10 it is possible to appreciate the response of the λ_{CPO} and the stack power measured values.

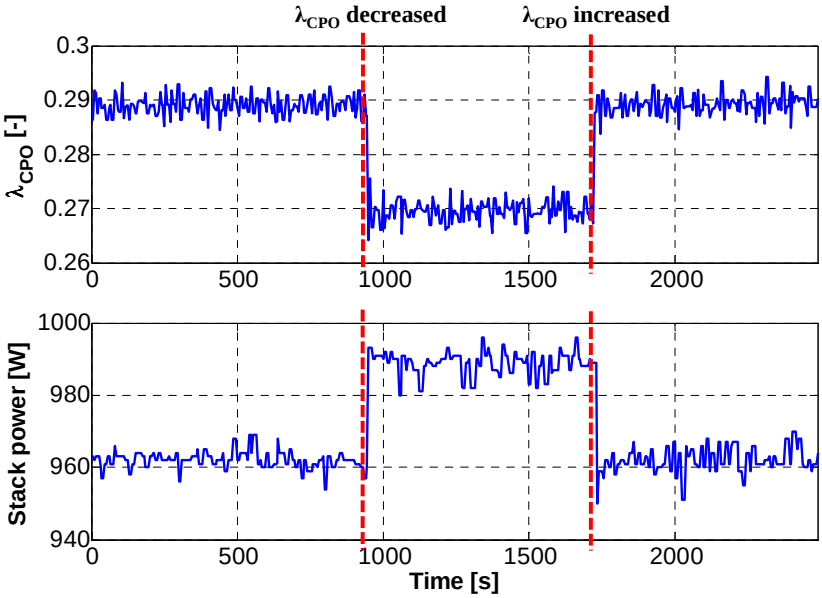

Figure 4.10 Response of the λ_{CPO} and the stack power to the CPO fault induction: as a direct effect of the λ_{CPO} set-point variation, its measured value changes as well, with a consequent increase in the stack power.

This value decreases from 0.29 to 0.27 and the stack power grows from 960 W (DC) to almost 990 W (DC), as expected from the results of the fault simulation presented in paragraph 3.2.4. These effects are in line with those described in paragraph 2.2.4.

4.3.5 Stack fault induction results

The last fault considered in this work concerns the increase in the stack ohmic resistance. The induction of this fault is performed through the exploitation of the electric resistance box, presented in Figure 4.5 and Figure 4.6, which is inserted between the stack and the inverter on the positive terminal.

Before describing the maneuver done for the fault induction, it is worth mentioning that during the entire faults induction activity performed at the EIFER laboratories, an accidental abrupt shut down of the Galileo 1000N system occurred, as mentioned in [53]. This event was caused by the system controller, which brought the system in a “safety mode” after reaching a certain stack temperature level, in order to avoid a severe system damage. This condition remained stable until the temperature controller was again enabled, followed by a complete recovery of the system.

Unfortunately, the effects of the system “safety mode” led to a small drift in the stack power value at normal operating condition. Indeed, as can be seen from Figure 4.9 and Figure 4.10, its value is almost 960 W (DC), whereas, after the system recovery, the stack power is lower than 950 W (DC). This last value can be observed in Figure 4.11, where the stack power and the exhaust blower power behavior during the stack fault induction are sketched.

This effect can be related to some degradation phenomena affecting the system, which had been subject to several tests required for the GENIUS project and described in Chapter 7, before being exploited for this experimental campaign.

The variation of the stack power at normal operating condition also affected the diagnostic algorithm adaptation process, as explained in paragraph 5.1.2.

Coming to the stack fault induction procedure, the followed maneuver

is characterized by a stepwise increase in the electric box resistance value, with a minimum step of 20 mΩ, as showed in Figure 4.11. In this picture it is possible to observe the effects of the resistance increase on the stack power and on the exhaust blower power.

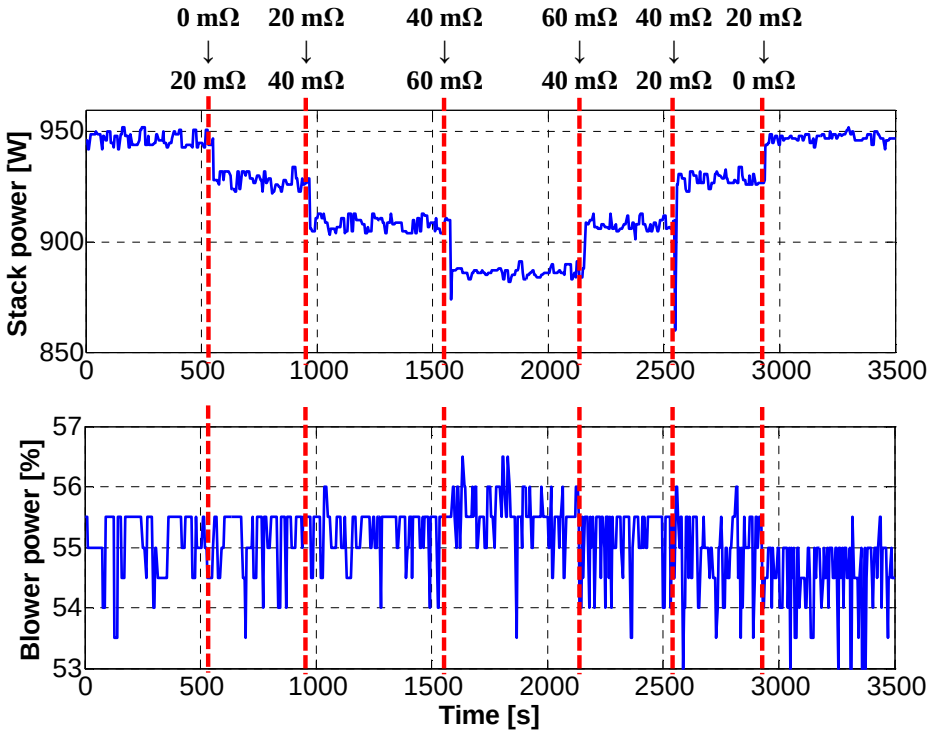

Figure 4.11 Stack power and blower power response to the stack fault induction: the resistance value of the electric box is switched stepwise from 0 mΩ to a maximum of 60 mΩ, with a step of 20 mΩ, inducing a decrease in the stack power and an increase in the blower power.

Moreover, the maximum resistance reached during this test is 60 mΩ, even though the maximum resistance value of the box is 100 mΩ. This choice is mainly due to the high influence of the current fault on the stack power, as observable from Figure 4.11. On the other hand, the blower power increase is less evident than the stack power reduction, especially for the high measurement noise level.

CHAPTER 5 Diagnostic Algorithm Application and Validation

The present chapter describes the validation procedure of the diagnostic algorithm developed in this work through its application to the Galileo 1000N system. It is again important to remark that the procedures and the results herein described have been carried out within the GENIUS project framework, in a close collaboration among the University of Salerno, the EIFER institute and the HEXIS AG company.

Before applying the diagnostic algorithm on the Galileo 1000N system, it is worth recalling that a specific adaptation process is required, in order to suit each part of the algorithm to the system under analysis. Indeed, the features related to the mathematical model and the FSM should be intended as "general", since they have been developed considering a generic SOFC system scheme, derived from heuristic knowledge and literature reviews, instead of referring to a real manufactured system.

5.1 Diagnostic algorithm tuning

According to the scheme sketched in Figure 1.9, the diagnostic algorithm design procedure is an offline process, which exploits the data gathered during the dedicated experimental activity on the Galileo 1000N. Such a procedure is described in the following paragraphs and its tasks are listed below. More in details, to perform the diagnostic algorithm tuning, several steps are taken into account. First of all, the communication protocol between the Galileo 1000N and the diagnostic algorithm is defined, in order to exploit online the data acquired on the system in real time. Then, the mathematical model required for the

residual calculation is specified, followed by the definition of the threshold levels, necessary for the symptoms generation. Finally, the FSM required for the isolation procedure is characterized starting from the approach described in Chapter 3. It must be recalled that, since all the measured data exhibit probabilistic features, a deterministic inference process should be coupled with a statistical one. The definition of this kind of procedure increases the robustness of the inference process, exploiting a formal algorithm to distinguish between normal and faulty status. Once all the tuned components of the diagnostic algorithm are presented, the validation process, based on the exploitation of the experimental results showed in the previous chapter, is discussed.

5.1.1 Communication protocol definition

The establishment of a proper communication protocol is an essential task, because this protocol allows the real-time data transfer to the diagnostic algorithm, in order to perform an online evaluation of the system state. As already mentioned in the previous chapter, the Galileo 1000N is controlled and regulated through the HexisView software, developed by HEXIS AG, which runs on a dedicated PC directly connected to the system. Through this software it is possible to regulate the system set-points and to retrieve information about the controlled and monitored variables. Moreover, an HexisView sub-function, called HexisViewLogger, allows gathering the monitored variables and saving them in a text file. For this reason, the HexisViewLogger is suitable for the development of a communication protocol based on the aforementioned text file, which can be read by the diagnostic algorithm to retrieve the required data. More in details, the HexisViewLogger reads the measured signals, related to specific monitored variables, and saves them in the text file, with a log frequency of 0.2 Hz [54]. This text file is periodically refreshed according to its maximum size, which cannot exceed 5 MB. The variables saved in the text file are read by the diagnostic algorithm and then treated to compute the residuals values during the monitoring process. A clear representation of the communication protocol scheme is presented in Figure 5.1.

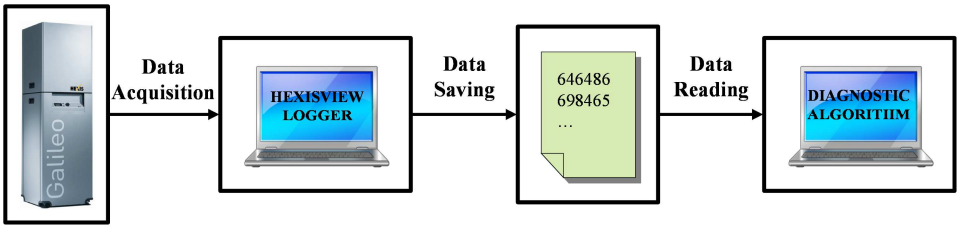

Figure 5.1 Communication protocol scheme, adapted from [54]**.**

To perform a proper diagnosis of the system status in real time, the data reading and the entire data treatment processes (i.e. residuals calculation, symptoms generation and fault isolation) should be completed within a time period lower or equal to that related to the HexisViewLogger data saving frequency. This condition can be fulfilled by means of a fast computational model, as the one presented in the following.

5.1.2 Mathematical model and threshold level definition

The mathematical model presented in Chapter 2 is not exploited for the validation process of the whole diagnostic algorithm. This choice has been mainly motivated by the need for a fast and handy model, which can be rapidly tuned by the algorithm user. Indeed, since the considered system is a pre-commercial one, the SOFC stack characteristics might promptly change due to further improvements on the production line, which can be mandatory for the market release of the final version of the system. For this reason, a model defined on a previous version of the system may not guarantee the required accuracy once implemented into the diagnostic algorithm for the on-field application. Therefore, to simulate the system in normal operating conditions, these considerations drove towards a model whose development does not require either a large number of experimental data (i.e. long term experiments) or the computation of specific parameters (sometimes based on information hard to retrieve).

This model exploits numerical maps, taking as input the values of the controlled set-points at a specific operating condition and returning as output the values of the monitored variables at that operating condition.

To build these maps, the monitored variables have been measured at a specific operating condition, and the acquired signals have been treated offline to calculate their average values, then gathered into numerical maps for each monitored variable.

In this work, only one operating condition has been considered, both for the experimental activity described in the previous chapter and the validation procedure herein illustrated. This operating condition, assumed from here on as the Galileo 1000N normal operating condition, can be represented by the set-points values of the controlled variables, listed in Table 5.1, which are regulated through the HexisView control panel. Once defined these values, the monitored variables have been measured and treated.

Table 5.1 Normal operating condition set-point values [54].

Set-point	**Value**	**Unit**
Stack temperature	820	°C
Single cell voltage	0.8	V
Gas input power	3300	W
λ_{CPO}	0.29	-

However, not all the system variables measured by the HexisView can be considered suitable for the model development, but only those matching the variables listed into the FSM exploited for the isolation process. Among those variables (see paragraph 3.1.2 and Table 3.2) only three are available in the HexisView, that are: i) the stack power, ii) the blower power and iii) the stack temperature. The stack voltage measurement is also available but it does not vary during the normal operation due to the potentiostatic control of the system.

The chosen monitored variables have been measured during steady state at normal operating condition and then they have been treated to evaluate their average values μ and their standard deviations σ, listed in Table 5.2. A representation of the raw signals of the measured variables (i.e. stack power, blower power and stack temperature) is given in Figure 5.2, whereas the *pdf* related to each raw dataset is sketched as a histogram in a separate window on the right side of each plot. Moreover, the average values μ and the standard deviation intervals $\mu \pm \sigma$ of each monitored value

are represented by a dashed red line and a couple of straight-dot green lines respectively. From the *pdf* shape it is possible to affirm that each monitored variable exhibits a normal distribution. This conclusion is supported by the *central limit theorem* (CLT), which states that the probability distribution of the averages of samples related to independent random variables can be well approximated by a normal distribution if the number of samples is sufficiently large [57]. According to Montgomery et al. [57], in many applications it has been observed that the normal distribution is quite suitable for datasets made up of more than 30 samples. The raw data plots presented in Figure 5.2 are related to a time space of 7000 s, which corresponds to a size of each dataset of about 1400 samples (i.e. acquisition frequency of 0.2 Hz). Consequently, a normal distribution can be assumed for each monitored variable.

Table 5.2 Average values μ and standard deviations σ of the monitored values referring to the set-point values of Table 5.1 (normal operating condition).

Variable	μ	σ
Stack power [W]	962.5	4.44
Blower power [%]	54.4	0.54
Stack temperature [°C]	820	0.25

The averages μ presented in Table 5.2 are essential for the definition of the map-based model, whereas the standard deviations σ can be exploited as guidelines for the definition of the optimal threshold levels for the symptoms generation. Another crucial aspect that must be taken into account for the thresholds setting is the quality of the measured signals. From the raw signals presented in Figure 5.2, it can be observed that the measured data, especially the blower power, are affected by quantization errors. In other words, the measured values have been automatically rounded according to the precision unit (i.e. quantization unit) of the measurement devices. According to the raw data distributions, the quantization units δ associated with the stack power, the blower power and the stack temperature are equal to 1 W, 0.5 W and 0.125°C respectively. Upon the knowledge of each quantization unit, the quantization error can be evaluated as half of the quantization unit [60].

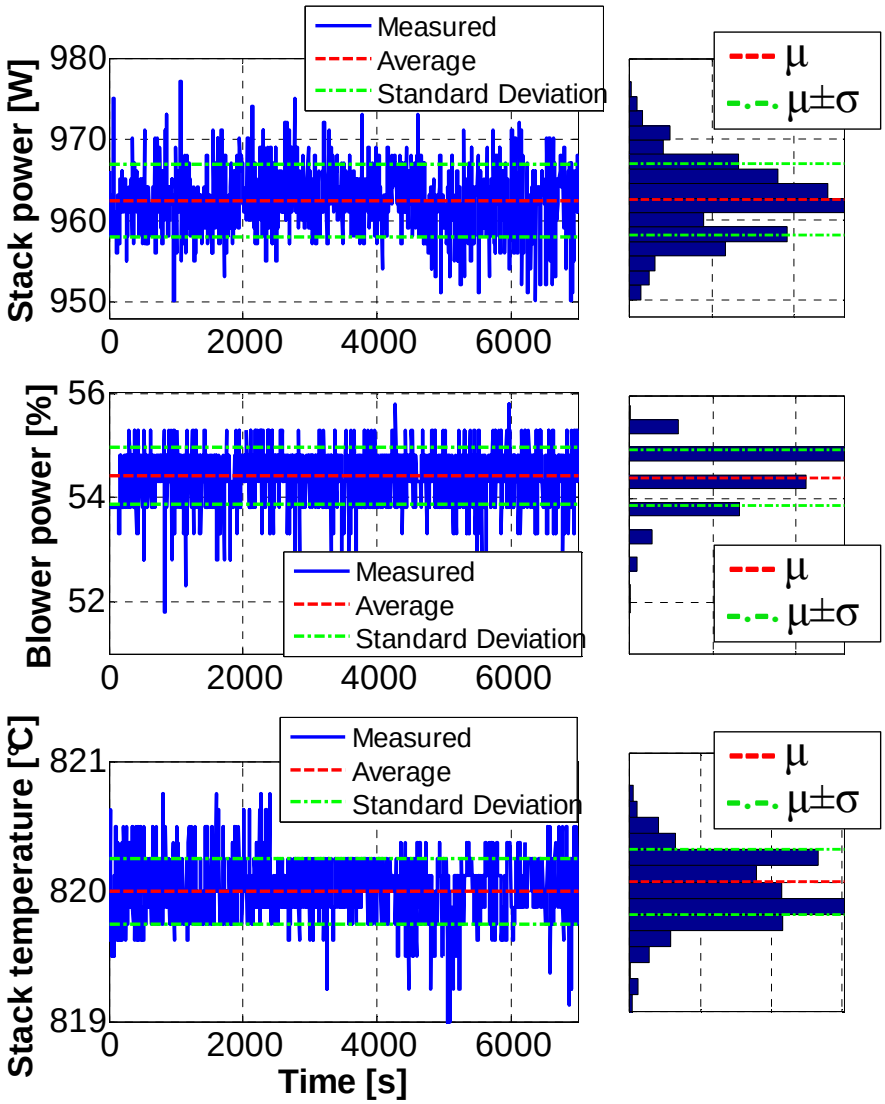

Figure 5.2 Raw signals, average values μ and standard deviation intervals $\mu \pm \sigma$ related to the measured monitored variables, with reference to the set-points of Table 5.1 (normal operating condition) for a time window of almost 2 hours.

It is worth highlighting that the stack power average value presented in Table 5.2 is used for the validation procedure with reference to the faults

induced before the system "safety mode recovery" occured, which are the temperature controller failure and the CPO surface degradation. For the other faults, a stack power average value equal to 945.8 W should be used, according to the comments expressed in paragraph 4.3.5. Considering this assumption, the average values of Table 5.2 are saved into a numerical map, becoming function of the operating condition set-points, as sketched in Figure 5.3. The values extracted from the map can be exploited, during the online monitoring task, to evaluate the residuals through equation (3.1). Also in this case, the residuals are evaluated as percent residuals, where Y is the monitored variable value acquired online, whereas $\hat{Y}$ is the average value of the considered variable extracted from the numerical maps.

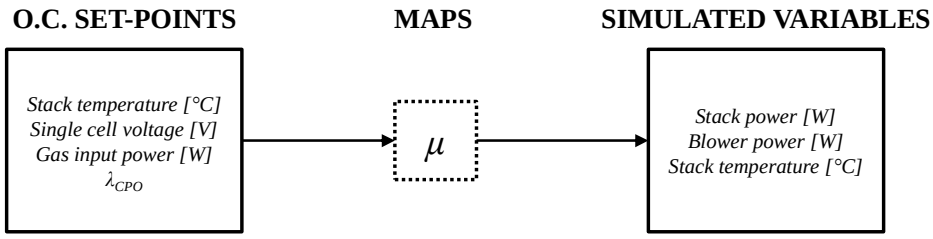

Figure 5.3 Map-based model scheme.

The choice of percent residuals allows the implementation of percent threshold levels as well. The standard deviation values of Table 5.2 and the quantization errors, evaluated for each monitored variable, are exploited to design the proper threshold required for the symptoms generation. As already mentioned, in the right side of Figure 5.2, the measured values distributions, with the average values (red dashed line) and the standard deviation interval related to a σ width (green straight-dot lines), are represented for each monitored variable. The $\mu \pm \sigma$ range includes the 68.27% of the measured samples [57].

A first useful indicator for the threshold level definition is the Coefficient of Variation (CV), which represents the normalized dispersion of a probability distribution and is expressed as σ/μ [65]. According to the values listed in Table 5.2, this coefficient is less than 0.5% for the stack power, less than 1% for the exhaust blower power and less than 0.05% for the stack temperature.

A second indicator can be obtained through the evaluation of the

quantization error. Considering a uniform scalar quantizer with a small step size δ and a negligible overload distortion, the mean-square error distortion can be approximated as $\delta^2/12$ and can be assumed limited into the range $[-\delta/2, \delta/2]$ [66]. For each monitored variable, the previous range limits of $\delta/2$ can be normalized with respect to the related variable average as $\delta/2\mu$. Considering the signals sketched in Figure 5.2, the previous expression leads to a value of 0.05% for the stack power, almost 0.5% for the exhaust blower power and a 0.008% for the stack temperature.

From the evaluation of the CV, the calculation of the quantization error limits and considering the interest in detecting incipient faults levels, a threshold range of ±1% can be assumed, ensuring that the standard deviation range $\mu\pm\sigma$ and the quantization error range $\mu\pm\delta/2$ are included within the threshold range [-1%, +1%]. Moreover, this range ensures the best FSM characterization process, as described in the following section.

5.1.3 FSM characterization

The characterization of an FSM suitable for the Galileo 1000N system is accomplished following the entire procedure described in Chapter 3 with reference to a threshold level of ±1%, defined in the previous paragraph. This procedure leads to the same FSM presented in Table 3.9, which is then updated recalling that the only available variables, which can be online monitored on the Galileo 1000N, are those listed in Table 5.2. As a result, the FSM of Table 5.3 is finally obtained.

As explained in Chapter 3, to perform a proper isolation procedure by means of an FSM, the fault patterns listed in the FSM rows should be independent from each other, so as to allow the univocal isolation of the occurring fault. However, the FSM of Table 5.3, characterized by five faults and only three symptoms, shows two rows with the same pattern (surrounded by bold edges in Table 5.3), that are the increase in blower mechanical losses and the leakage at stack outlet. For this reason, it is not possible with the available number of symptoms (i.e. monitored variables) to perform an univocal isolation procedure for these two faults. Consequently, the two aforementioned faults are grouped into a common fault cluster, represented with the symbol f_{12}.

Table 5.3 Improved FSM characterized for the Galileo 1000N system with reference to a threshold level of ±1%.

τ = 1%	**SYMPTOMS**	Stack power	Exhaust blower power	Stack temperature
FAULTS		s_1	s_2	s_4
Increase in blower mechanical losses	f_1	0	1	0
Leakage	f_2	0	1	0
Temperature controller failure	f_3	1	1	1
CPO surface degradation	f_4	1	0	0
Stack ohmic resistance increase	f_5	1	1	0

The FSM presented in Table 5.3 is the most suitable one attainable with the available measurements. The choice of a threshold level of ±1% limited the number of fault clusters to one, with only two faults within. Indeed, setting a higher threshold value, for example ±5%, would have led to an FSM characterized by one fault cluster (faults f_1 and f_2 grouped together) and the removal of the fault f_4, since the symptoms related to the monitored variables are all zero (see Table 3.10).

With the FSM defined in Table 5.3, the isolation procedure can be performed. However, before comparing any symptoms vector with those of the considered FSM, it is mandatory to understand if all the arising symptoms are generated by a faulty state or they are false alarms. The discrimination between these two events is achieved by means of a statistical hypothesis test, as described in the following.

5.1.4 Statistical hypothesis test

As mentioned in the previous sections, a deterministic interpretation of the results should be avoided in favor of a probabilistic analysis. As

explained in Chapter 1 (i.e. Figure 1.4), statistics allows to distinguish if any arisen symptom, related to a single measured point, has been determined by a faulty state or is just a false alarm. Moreover, it is also possible to confer a specific probability of missed fault to each system state inference.

For these reasons, to achieve a robust inference on the system status, a statistical hypothesis test on the averages of two samples is exploited [10][57][62]. This test infers on the unknown averages μ_1 and μ_2 of two independent populations, in order to verify a specific hypothesis on their difference μ_1-μ_2. This procedure uses the information obtained from two samples, extracted from the aforementioned populations. In this work, all the monitored variables (i.e. stack power, exhaust blower power and stack temperature), either in normal operating condition or in faulty state, are stochastic variables, whose measured values represent the populations of the observations.

Focusing on just one variable, the collection of its values both in normal operating condition and in faulty state sets up two independent populations. One sample is extracted from the population referring to the normal operating condition, whereas the other sample is extracted from the population referring to the faulty state.

Before applying the hypothesis test theory, two assumptions have to be made. The first one is on which kind of distribution the two populations refer to. In this case, the *central limit theorem* CLT can be used: if the sizes n_1 and n_2 of the samples extracted from the two populations are larger than 30 samples, the populations distribution can be considered normal [57]. The second assumption is on the populations variances σ_1^2 and σ_2^2, which are considered unknown but equal ($\sigma_1^2=\sigma_2^2=\sigma^2$). This last hypothesis is reasonably consistent with the characteristics of the measured signal. From the abovementioned assumptions, the *t-test* is considered [57].

Once the previous assumptions have been made, the complete test procedure can be defined. The first step consists in the statement of the relevant null hypothesis H_0 and alternative hypothesis H_1. By rejecting the null hypothesis H_0 it can be stated that the system is in faulty state, whereas by rejecting the alternative hypothesis H_1 it can be stated that the system is in normal conditions. Assuming that Δ_0 is the reference difference of the populations averages:

$$\begin{aligned} H_0 &: |\mu_1 - \mu_2| = \Delta_0 \\ H_1 &: |\mu_1 - \mu_2| > \Delta_0 \end{aligned} \tag{5.1}$$

The alternative hypothesis H_1 has been defined as an unilateral one and states that the average μ_1 lies out of the range $[\mu_2\text{-}\Delta_0,\mu_2\text{+}\Delta_0]$. This choice is justified considering that the aim of the test is to refuse the null hypothesis, so as to assert with a certain probability that the system is in faulty state. For this reason, the denial of the null hypothesis implies refusing that the average μ_1 lies within the range $[\mu_2\text{-}\Delta_0,\mu_2\text{+}\Delta_0]$.

Since two populations with equal unknown variances are analyzed, a *t* distribution statistic has to be taken into account. For this reason, to refuse the null hypothesis the statistic t_0 can be defined as [57]:

$$t_0 = \frac{\left|\mu_{samp,1} - \mu_{samp,2}\right| - \Delta_0}{S_p\sqrt{\frac{1}{n_1} + \frac{1}{n_2}}} \tag{5.2}$$

where the terms $\mu_{samp,1}$ and $\mu_{samp,2}$ are the averages of the samples extracted from the two populations and n_1 and n_2 their sizes. The term S_p is the pooled standard deviation estimated from the pooled variance [57]:

$$S_p^2 = \frac{(n_1 - 1)\sigma_{samp,1}^2 + (n_2 - 1)\sigma_{samp,2}^2}{n_1 + n_2 - 2} \tag{5.3}$$

The pooled variance provides an estimation of the populations variances, exploiting the standard deviations $\sigma_{samp,1}$ and $\sigma_{samp,2}$ of the two extracted samples.

In the frame of this work, the reference difference Δ_0 can be defined recalling that one sample refers to a normal operating condition, whereas the other refers to a faulty state. Defining as $\mu_{samp,2}$ the average of the normal operating condition sample, corresponding to each value listed in Table 5.2, Δ_0 can be expressed as:

$$\Delta_0 = \mu_{samp,2}\tau \tag{5.4}$$

where τ is the percent threshold value defined as ±1% in the previous paragraph. This choice ensures that the null hypothesis can be refused for all those $\mu_{samp,1}$ values laying outside the reference threshold range.

The statistic t_0 has a t probability distribution with n_1+n_2-2 degrees of freedom [57]. The rejection region of H_0 can be defined as [57]:

$$t_0 > t_{\alpha,n_1+n_2-2} \tag{5.5}$$

where α is the significance level of the test. This level corresponds to the probability of incorrectly rejecting the null hypothesis, which corresponds in this case to the probability of false alarm, and here set equal to 0.01 (i.e. a confidence interval of 99%).

The remaining parameters to be set are the samples sizes n_1 and n_2. To set these values, the *operating characteristics* (OC) curves can be used [57]. These curves are function of two parameters: i) the *false negative rate*, which represents the probability of erroneously failing in reject the null hypothesis when it is false (which can be also interpreted as the probability of missed fault), and ii) a scaling factor d defined as:

$$d = \frac{|\Delta_0|}{2\sigma} \tag{5.6}$$

According to equation (5.6), the scaling factor d is function of the reference populations averages difference Δ_0 and the population standard deviation σ. The former can be easily computed through equation (5.4), whereas the latter, because it is unknown, must be estimated. The standard deviations of Table 5.2 can be used as reference values to compute the scaling factor corresponding to each monitored variable.

From [57], a high scaling factor, associated to a low false negative rate, leads to a low sample size. Nevertheless, the minimum sample size should be greater than 30 to ensure that the populations present a normal probability distribution. For this reason, the lowest scaling factor, chosen among those computed with respect to all the monitored variables, is considered. According to a threshold level of ±1% and the values listed in Table 5.2, the lowest scaling factor is that referred to the exhaust blower power:

$$d = \frac{|\Delta_0|}{2\sigma} = \frac{|\mu\tau|}{2\sigma} = \frac{|54.4 \cdot 0.01|}{2 \cdot 0.54} \cong 0.5 \tag{5.7}$$

From the OC curves sketched in [57], the assumption of a false negative rate equal to 0.01, coupled with a 0.5 scaling factor, leads to a theoretical sample size of 90 samples. According to Montgomery et al. [57] and assuming that n_1=n_2, the evaluation of the real sample size is:

$$n_1 = n_2 = \frac{90+1}{2} = 45.5 \approx 46 \tag{5.8}$$

Considering the sample size computed through equation (5.8) and a significance level of 0.01, equation (5.5) becomes:

$$t_0 > t_{0.01,90} = 2.326 \tag{5.9}$$

The evaluation of the statistic t_0, and the consequent verification or refusal of the null hypothesis, allows the interpretation of the nature of each arisen symptom. With the definition of the test procedure, the tuning of the diagnostic algorithm is completed. In the following paragraph, the results of the experimental validation process are presented.

5.2 Diagnostic algorithm validation

The validation procedure of the diagnostic algorithm is performed exploiting the data gathered during the experimental activity presented in Chapter 4. For each considered fault, the acquired signals are treated to compute residuals and generate analytical symptoms. Each symptom is associated to the result of the hypothesis test to understand if it has been caused by a faulty state or it is only a false alarm.

If the test ensures that a fault is occurring, the complete symptoms vector is assembled and compared to the rows of the FSM presented in Table 5.3. In case of a complete match, the isolated fault type is compared to the one induced on the real system, to understand if a successful

detection and isolation has been obtained.

An example of the procedure followed for the generation and analysis of a symptom is sketched in Figure 5.4. It is important to remark that, although every generated symptom is related to a single measurement point, the hypothesis test is performed with a sample. Considering the generic residual time behavior drawn on the top of Figure 5.4, each dot represents a measured point. When a residual point exceeds the ±1% threshold, a symptom arises.

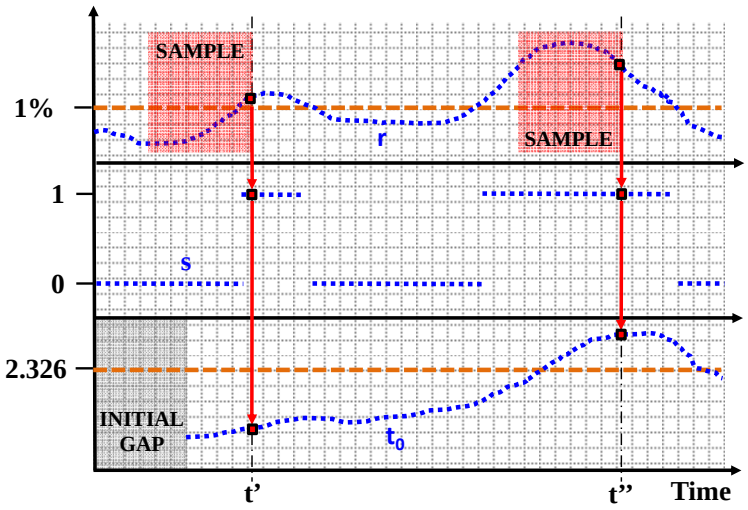

Figure 5.4 Example of symptom generation and analysis through hypothesis test.

Since the hypothesis test requires the extraction of a sample, this sample is defined selecting the point under analysis and all the 45 previous measured points, in accordance with the size defined through equation (5.8). This means that the inference on the symptom nature at a specific moment is influenced by all the previous measured points. The sample extraction induces an initial gap in the t_0 statistic evaluation. This gap is caused by the fact that the first 45 measured points cannot be analyzed with the hypothesis test since the lack of previous measured points hinders the extraction of significant samples.

In the example given in Figure 5.4, two residual points (one at *t'* and another at *t"*) have been chosen to explain how the hypothesis test works. Both points induce a symptom, but only the second one relates to a t_0

statistic higher than the H_0 rejection region ($t_0 > 2.326$), which allows the rejection of the null hypothesis. This means that the first considered symptom should be taken as a false alarm, whereas the second one as caused by a faulty state. This conclusion highlights that, to perform a reliable and efficient isolation task, both the symptoms and the related statistics should be considered. Indeed, a symptom being 1 is a necessary but not sufficient condition to state that a faulty state is occurring in the system. However, coupling this information with a statistic higher than the H_0 rejection region, a necessary and sufficient condition is obtained.

It is worth noting that every conclusion on the symptom nature is always associated to a significance level α of 0.01 and a false negative rate of 0.01, which represent the probability of false alarm and missed fault, respectively.

5.2.1 Blower fault validation results

The first fault considered for the validation process consists of an increase in the exhaust blower absorbed power. Some of the experimental data obtained during the fault induction have been presented in paragraph 4.3.1. The acquired signals are exploited for the calculation of the residuals, by means of equation (3.1) and the average values of Table 5.2, which are then compared to a ±1% threshold range for the generation of the related analytical symptoms. The symptoms nature is deduced through the hypothesis test results. The resulting symptoms vector is then compared to the rows of the FSM presented in Table 5.3.

The obtained residuals, analytical symptoms and t_0 statistics are presented in Figure 5.5, Figure 5.6 and Figure 5.7, for the stack power, the exhaust blower power and the stack temperature, respectively. The residual plots show two horizontal red dashed lines, which represent the threshold region of ±1%, whereas the t_0 statistic plots have a single horizontal red dashed line, which is the limit of the H_0 rejection region of 2.326.

About the stack power residual behavior in Figure 5.5, it is well included within the defined threshold range, leading the related symptoms to be zero in most cases, except for few points. However, taking a look at the t_0 statistic trend, it is always lower than the H_0 rejection limit. This

result allows to assert that the few arisen symptoms are false alarms.

Differently from the stack power, the blower power residual, shown in Figure 5.6, clearly exceeds the +1% limit after about 5000 s, with a maximum variation of almost +8.5%, in line with the fault simulation results exposed in paragraph 3.2.1. This trend induces all the related symptoms to be 1 after this time. Before 5000 s, the residual crosses repeatedly both the threshold boundaries, but with a small amplitude, with the related symptoms being alternatively 0 and 1. Nevertheless, the evaluation of the t_0 statistic gives a clearer interpretation of the results. Indeed, by perceiving its trend, it can be asserted that only the symptoms arisen after 5000 s can be related to a faulty state, whereas the previous ones can be assumed as false alarms. An interesting comment can be made on a symptom being 0 at around 8500 s in Figure 5.6. In this work, the requirements to state that a fault is occurring in a specific moment are both a symptom being 1 and the related t_0 statistic exceeding the H_0 rejection limit. For this reason, although the t_0 statistic related to the aforementioned symptom point is higher than 2.326, this point is not considered a fault. Thus, this event might be classified as a missed fault.

The last results to be evaluated are those concerning the stack temperature, presented in Figure 5.7. The analysis of all the displayed trends yields to the conclusion that the stack temperature remains in normal condition for the whole duration of the considered time window.

Summing up the obtained results, it can be concluded that, when the fault occurs, the only affected variable is the exhaust blower power, whereas both the stack power and the stack temperature remain unchanged. The evaluation of the symptoms trends, coupled with the t_0 statistics, lead to the univocal symptoms vector [0 1 0]. From this vector it is already possible to affirm that an unexpected behavior is occurring in the system, because at least one symptom is 1.

To infer which kind of fault corresponds to this behavior, the obtained symptoms vector is compared to each row of the FSM presented in Table 5.3, obtaining a perfect match with the one related to the fault cluster f_{12}. Since this fault cluster includes the induced fault, it is possible to assert that the diagnostic algorithm is capable of correctly detecting and isolating the expected fault cluster. This conclusion is quite satisfactory, although it is not possible to isolate the single fault with the current monitored variables.

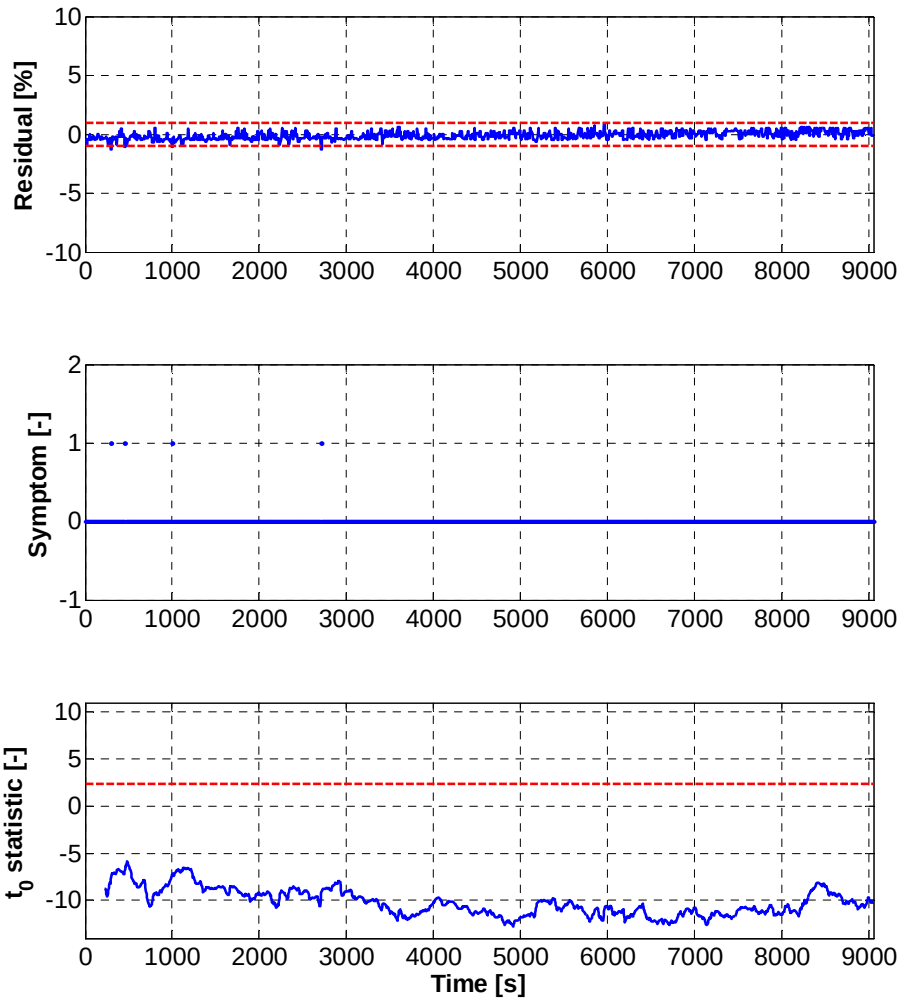

Figure 5.5 Stack power residual, analytical symptom and t_0 statistic related to an increase in the exhaust blower mechanical losses.

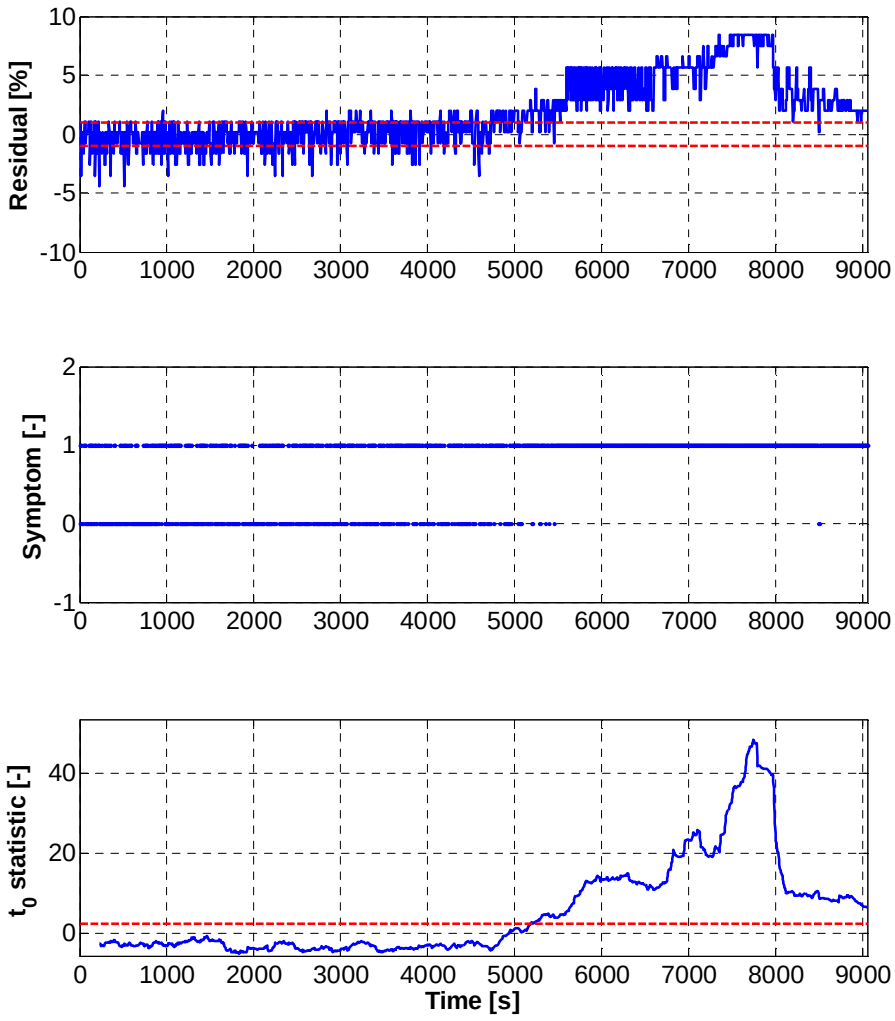

Figure 5.6 Exhaust blower power residual, analytical symptom and t_0 statistic related to an increase in the exhaust blower mechanical losses.

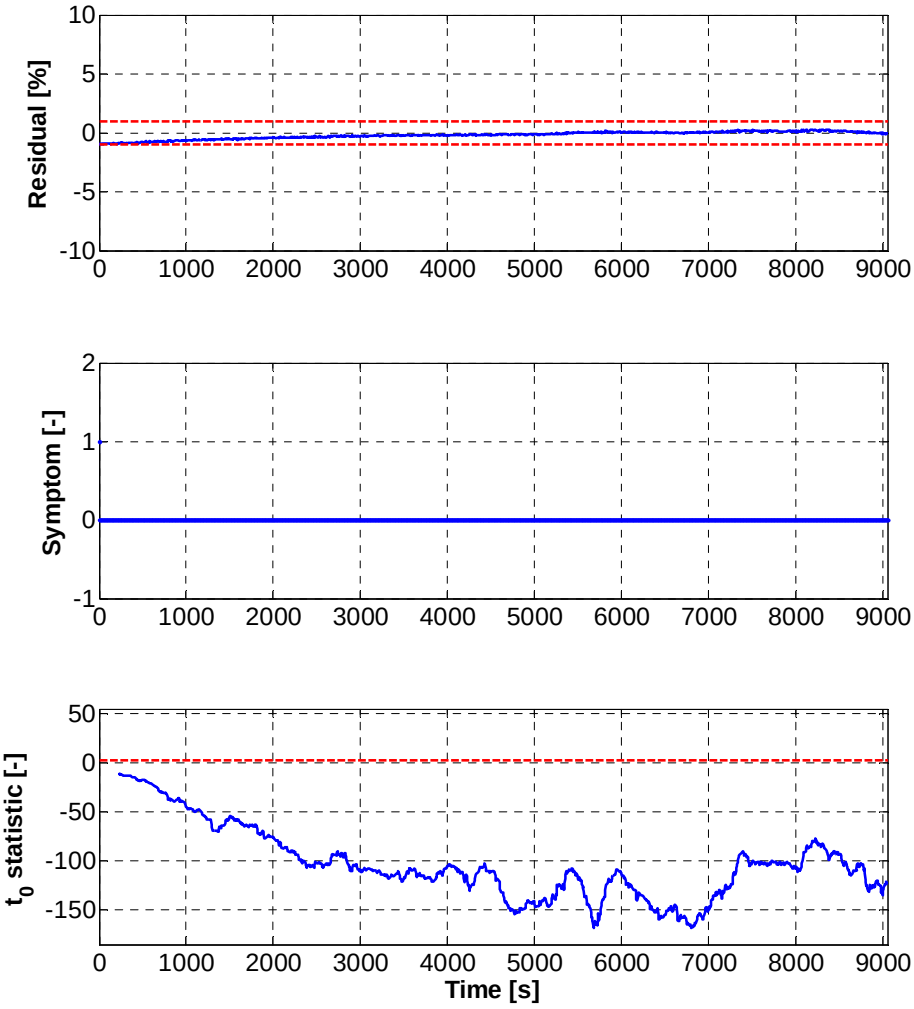

Figure 5.7 Stack temperature residual, analytical symptom and t_0 statistic related to an increase in the exhaust blower mechanical losses.

A last comment can be made on the time required to have a first detection. Looking at the t_0 statistic trend of Figure 5.6, it exceeds the limit of 2.326 at 5200 s. Considering that the fault started right after 4000 s (see Figure 4.7), it took around 20 minutes to detect the fault for the first time. Moreover, it is also possible to assert that, since all the symptoms arisen before this stage must be considered false alarms, the algorithm is

also capable of correctly categorizing the obtained symptoms. The only discrepancy occurs between 4000 s and 5200 s, where the system is actually in faulty state but the algorithm still identifies the symptoms as false alarms. This event is due to the detection delay of 20 minutes, but it can be considered acceptable since the fault has a low magnitude. On one hand, this delay could be reduced with a different tuning of the algorithm parameters, but this may lead to an accuracy reduction. On the other hand, the delay reduction could also be achieved by increasing the sampling rate of the measurement devices, so as to reduce the time window keeping the same samples number.

5.2.2 Leakage validation results

Concerning the leakage between the SOFC stack and the exhaust blower, the same validation procedure described in the previous paragraph is followed. The signals acquired during the experimental activity described in paragraph 4.3.2 are exploited for the calculation of the residuals, by means of equation (3.1) and the average values of Table 5.2. These residuals are then compared to a ±1% threshold range for the generation of the related analytical symptoms, whose nature is deduced through the hypothesis test. The resulting symptoms vector is then compared to the rows of the FSM of Table 5.3.

The attained residuals, analytical symptoms and t_0 statistics related to the stack power, the exhaust blower power and the stack temperature are presented in Figure 5.8, Figure 5.9 and Figure 5.10 respectively.

Concerning the stack power (Figure 5.8), its residual behavior lies within the ±1% threshold range for the whole duration of the considered timespan, except for one point around 1100 s, which shows a related symptom equal to 1. However, the t_0 statistic trend ensures that the aforementioned symptom is only a false alarm.

On the contrary, the blower power residual, presented in Figure 5.9, exceeds the threshold boundaries clearly after 1500 s, with almost all the related symptoms being 1. The maximum residual variation is around +3.9%, in line with the fault simulation results exposed in paragraph 3.2.2. It is interesting to observe that this maximum is reached right after the leakage valve closure at around 1600 s (see Figure 4.8).

This behavior highlights the slow response of the exhaust blower power to the current fault, due to the slow system thermal dynamics (see paragraph 4.3.2). Before 1500 s, the residual crosses several times the ±1% range, inducing a sequence of 0 and 1.

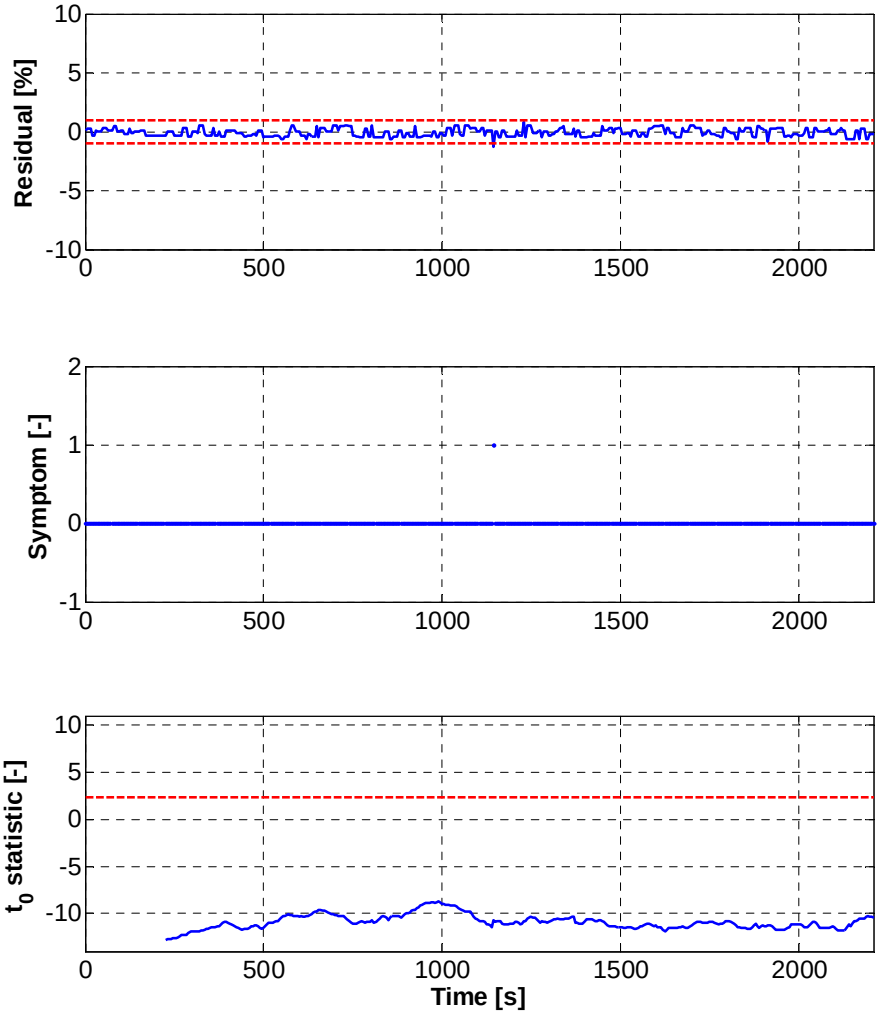

Figure 5.8 Stack power residual, analytical symptom and t_0 statistic related to a leakage between the SOFC stack and the exhaust blower.

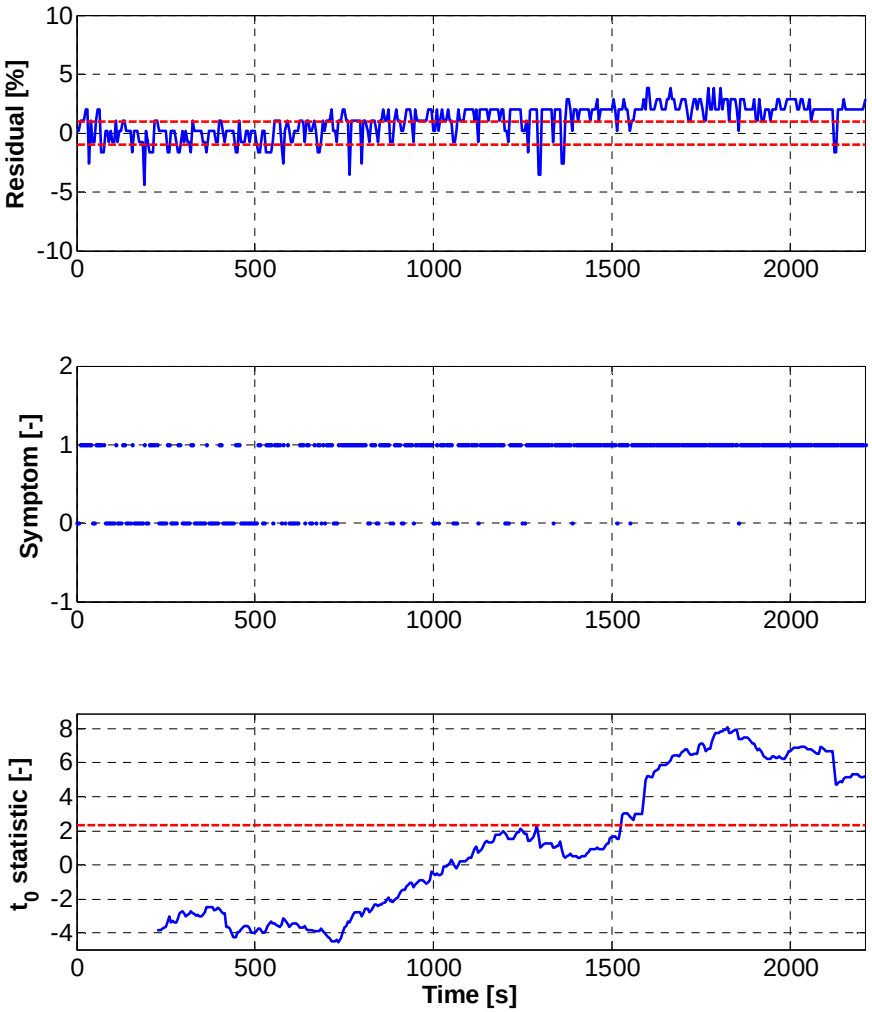

Figure 5.9 Exhaust blower power residual, analytical symptom and t_0 statistic related to a leakage between the SOFC stack and the exhaust blower.

Also in this case, the analysis of the related t_0 statistic trend can help to recognize the symptoms nature. The t_0 statistic exceeds the H_0 rejection limit right after 1500 s. This means that only the symptoms arisen after this time can be assumed as generated by a faulty state, whereas all the other should be classified as false alarms.

The results concerning the stack temperature are almost the same obtained for the stack power. Indeed, the residual showed in Figure 5.10 remains always within the ±1% threshold range. Thus, no symptom arises during the whole considered period. Also the related t_0 statistic trend remains much lower than the H_0 rejection limit.

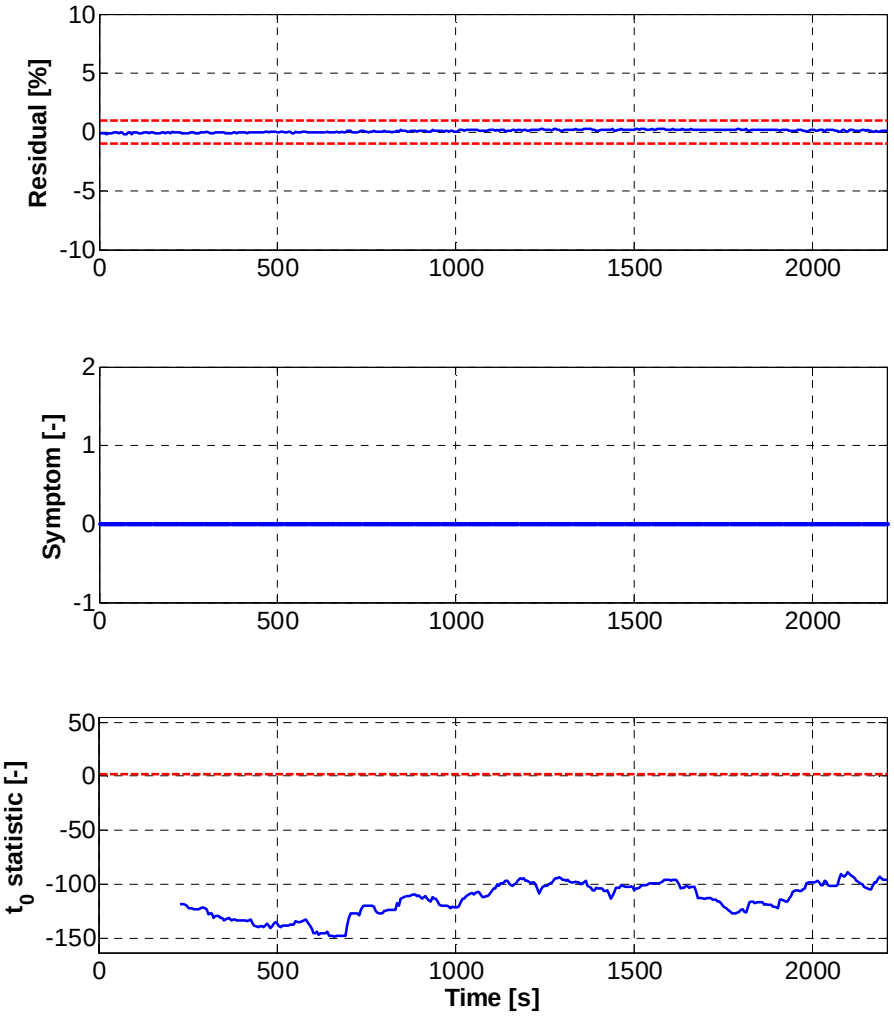

Figure 5.10 Stack temperature residual, analytical symptom and t_0 statistic related to a leakage between the SOFC stack and the exhaust blower.

From the presented results, it can be stated that the only monitored variable clearly affected by the current fault is the exhaust blower power. The evaluation of the symptoms trends during the considered time window, coupled with the t_0 statistics, leads to the univocal symptoms vector [0 1 0]. Since at least one symptom is equal to 1, the algorithm detects an abnormal state. The inference process involves the comparison of the obtained symptoms vector to each row of the FSM of Table 5.3, obtaining a perfect match with the fault cluster f_{12}. As explained in paragraph 5.1.3, due to the reduced number of monitorable variables, the leakage fault has been included into a fault cluster, specifically the cluster f_{12}. Thus, the isolation of the expected fault cluster confirms that the diagnostic algorithm is capable of performing a correct detection and fault cluster isolation. As asserted for the previous fault, this conclusion is quite acceptable, although it is not possible to univocally isolate the single fault due to the low number of monitored variables.

In conclusion, concerning the time required to have a first detection, the t_0 statistic trend in Figure 5.9 exceeds the limit of 2.326 right after 1500 s. This means that a first detection is performed almost 20 minutes after the valve opening (see Figure 4.8). What is interesting to observe is that the symptoms trend starts to become 1 more frequently after 750 s (Figure 5.9), and the t_0 statistic shows a monotone increase at that time, almost reaching the H_0 rejection limit at 1250 s, but without crossing it. On the other hand, it decreases right after this point, probably due to an increment in the exhaust blower power fluctuations, which might induce a growth in the samples variance. This event may have extended the real detection delay, but, as stated for the previous fault, a delay of 20 minutes can be considered satisfactory for a fault with low magnitude.

5.2.3 Controller failure validation results

The third fault entails the temperature controller failure, whose experimental induction and the related effects in terms of stack temperature and stack power have been described in paragraph 4.3.3. The obtained residuals, the symptoms and the t_0 statistics associated to the stack power, the exhaust blower power and the stack temperature are illustrated in Figure 5.11, Figure 5.12 and Figure 5.13 respectively. More

in details, the first variable to be analyzed is the stack power. Its residual behavior, presented in Figure 5.11, shows a slow but monotonous decrease after 1100 s, passing through the -1% threshold limit right before 1500 s.

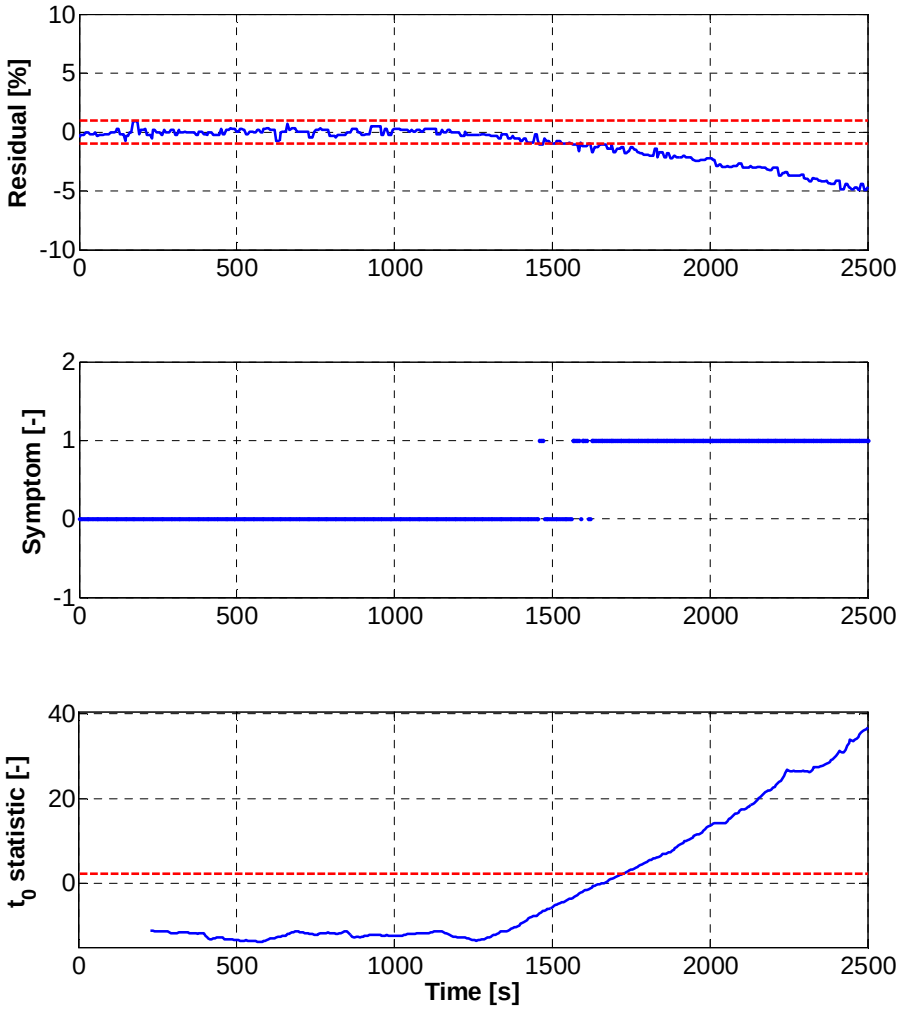

Figure 5.11 Stack power residual, analytical symptom and t_0 statistic related to a temperature controller failure.

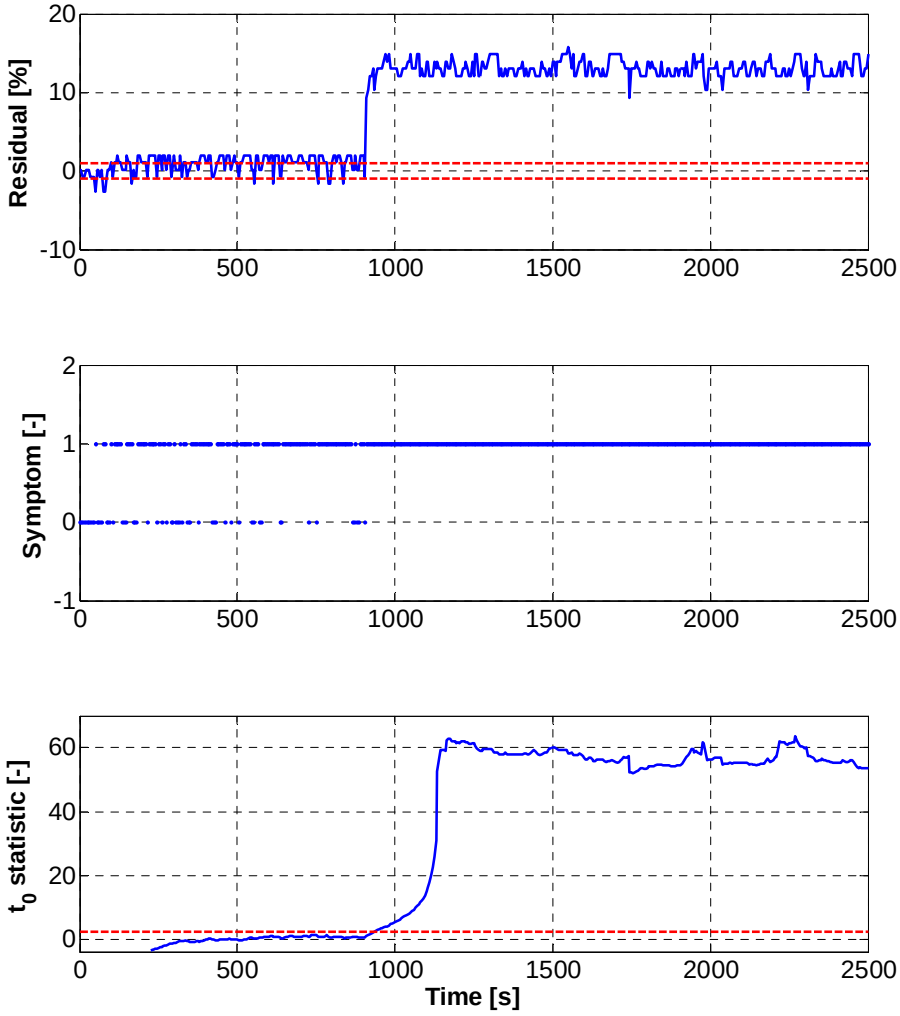

Figure 5.12 Exhaust blower power residual, analytical symptom and t_0 statistic related to a temperature controller failure.

At that time, as a direct consequence, the symptoms start to arise, stabilizing at 1 around 1600 s. Moreover, the t_0 statistic trend starts to monotonously increase around 1400 s, going beyond the H_0 rejection limit after 1700 s. From Figure 5.12 it is possible to observe that the exhaust blower power residual increases abruptly at 900 s, right after the

fault induction (see Figure 4.9), reaching a maximum value of +15% at steady state.

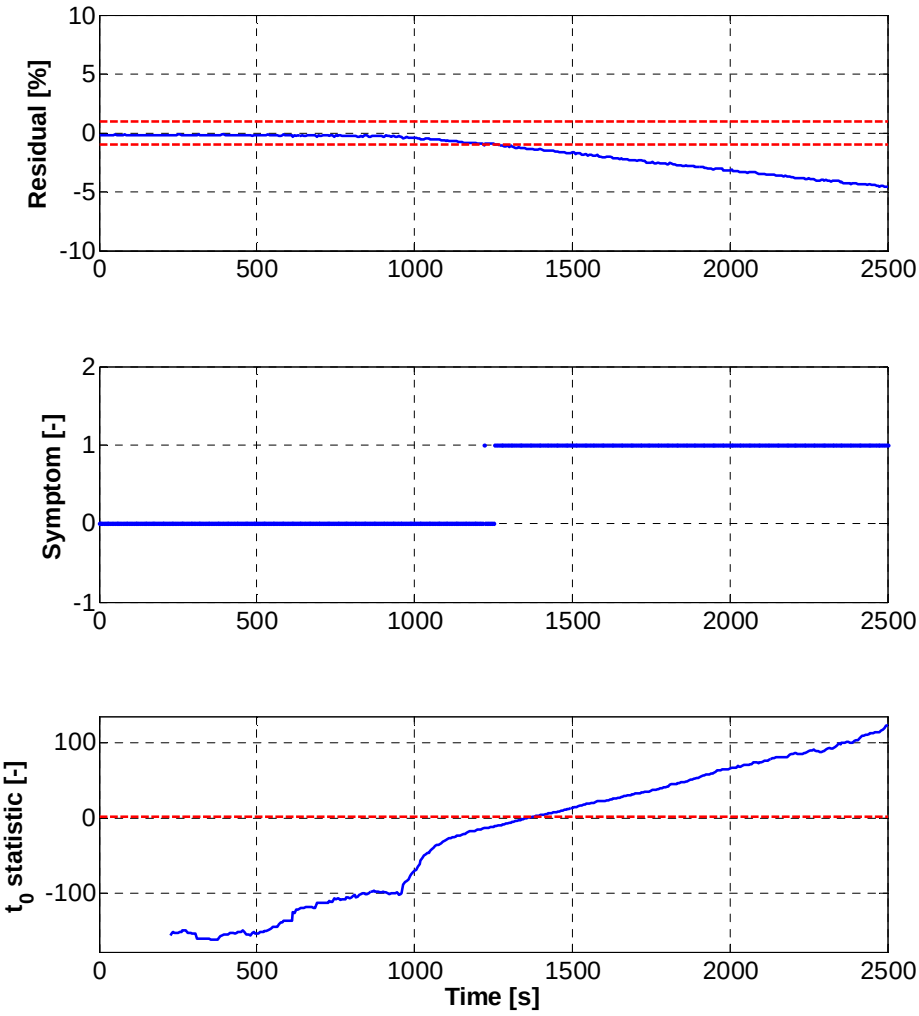

Figure 5.13 Stack temperature residual, analytical symptom and t_0 statistic related to a temperature controller failure.

This growth is a direct effect of the manual change of the exhaust blower operating set-point, done right after the controller being disabled. This

trend induces the related symptoms to be 1 from 750 s until the end of the considered time window (see Figure 5.12). However, before this stage, the symptoms trend is already 1 in most cases, due to a strong oscillation of the blower power signal, which frequently crosses the threshold limits in both the directions. Also in this case, the t_0 statistic should be used for the interpretation of the symptoms nature. Indeed, its trend shows an abrupt increase at 900 s, as the associated residual, going almost instantly beyond the H_0 rejection limit. According to this trend, all the symptoms arisen before 900 s should be classified as false alarms.

The same comments made for the stack power can be also extended to the stack temperature results, sketched in Figure 5.13. The stack temperature residual starts to decrease monotonously after 900 s, and goes through the -1% threshold limit at around 1200 s. At that time, the related symptoms behavior becomes 1 and remains at that value until the end of the considered timespan. Concerning the t_0 statistic, it shows an increasing monotonous trend, going beyond 2.326 at almost 1400 s.

Summing up the obtained results, it is possible to state that all the monitored variables are affected by this fault. From the symptoms behavior here illustrated, coupled with the related t_0 statistics trend, the obtained symptoms vector is [1 1 1]. Actually, it is worth highlighting that this pattern has been reached only after a certain period of time, because the symptoms related to each monitored variable have become 1 at different moments. Initially, the first obtained pattern is [0 1 0], at 920 s, followed by the pattern [0 1 1] at 1400s. The final pattern [1 1 1] is reached only at 1700 s. Comparing this final pattern with each row of the FSM of Table 5.3, a perfect match with the one related to the fault f_3 is obtained. Differently from the two previous validation procedures, since the third row of the considered FSM presents an unambiguous symptoms vector pattern, the fault is univocally isolated. This result ensures the correct detection and isolation of the expected fault. Another difference which can be identified with respect to the previous validation procedures is the time discrepancy between the detection of an unexpected event and the isolation of the correct faulty state. On one hand, the detection is obtained at 920 s, when a symptoms being 1 is associated to a faulty state through the related t_0 statistic, with a delay of about 3 minutes with respect to the fault induction at 700 s (see Figure 4.9).

On the other hand, the isolation of the correct fault is achieved only at 1700 s, with a further delay of about 13 minutes. Thus, the whole delay

between the fault induction and its isolation is around 16 minutes, comparable to the delays computed for the previous faults. This result highlights the importance of waiting a certain amount of time before performing a reliable inference on the system state, conclusion drawn also by Escobet et al. [17] in their work.

5.2.4 CPO fault validation results

Concerning the CPO surface degradation, the related experimental induction has been described in paragraph 4.3.4. The obtained results in terms of residuals, analytical symptoms and t_0 statistics are showed in Figure 5.14 for the stack power, in Figure 5.15 for the exhaust blower power, and in Figure 5.16 for the stack temperature.

As already illustrated in Figure 4.10, the direct consequence of the variation of the λ_{CPO} set-point consists in the increase in the stack power, whose related residual abruptly increases from 0 to around +2.8% (Figure 5.14), exceeding the +1% threshold limit at 950 s. Moreover, the residual shows a following abrupt return within the ±1% threshold range at 1730 s, in conjunction with the λ_{CPO} set-point decrease to the normal condition. The residual behavior induces the related symptoms to be equal to 1 in the time window between 950 s and 1730 s. However, observing the t_0 statistic trend, it is possible to associate only the events after 1070 s to a faulty state.

About the blower power results showed in Figure 5.15, the strong oscillations, measured during the fault induction, lead the associated residual to cross repeatedly the ±1% threshold range in both directions, with an alternation of 0 and 1. However, according to the related t_0 statistic trend, the arisen symptoms should be classified as false alarms.

Concerning the results presented in Figure 5.16, it can be clearly stated that the stack temperature is not affected by this fault.

According to the conclusions here drawn, the obtained univocal symptoms vector is [1 0 0], meaning that an abnormal state has been detected. Through the comparison of the attained symptoms vector with the rows of the FSM of Table 5.3, a perfect match with the one related to the fault f_4 is obtained. From this result it is possible to state that, also in this case, the diagnostic algorithm performed a successful detection and

isolation of the correct fault. Furthermore, the detection is delayed by only 2 minutes.

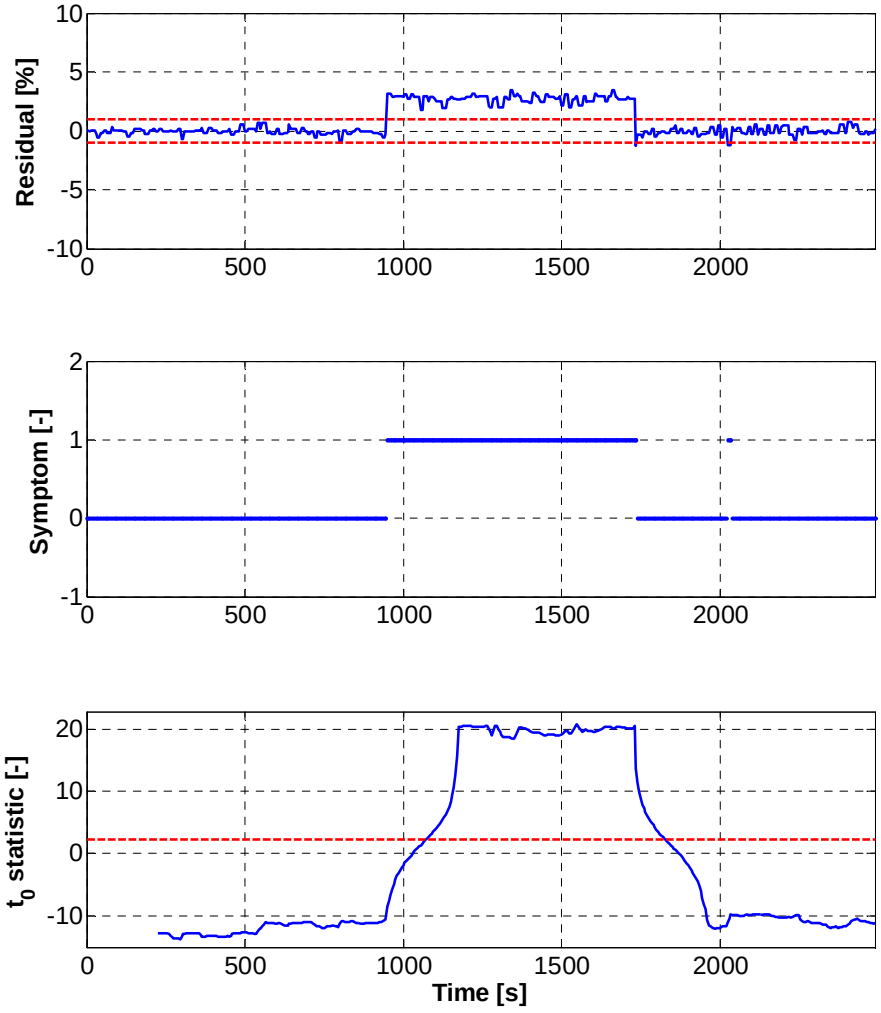

Figure 5.14 Stack power residual, analytical symptom and t_0 statistic related to a surface degradation of the CPO.

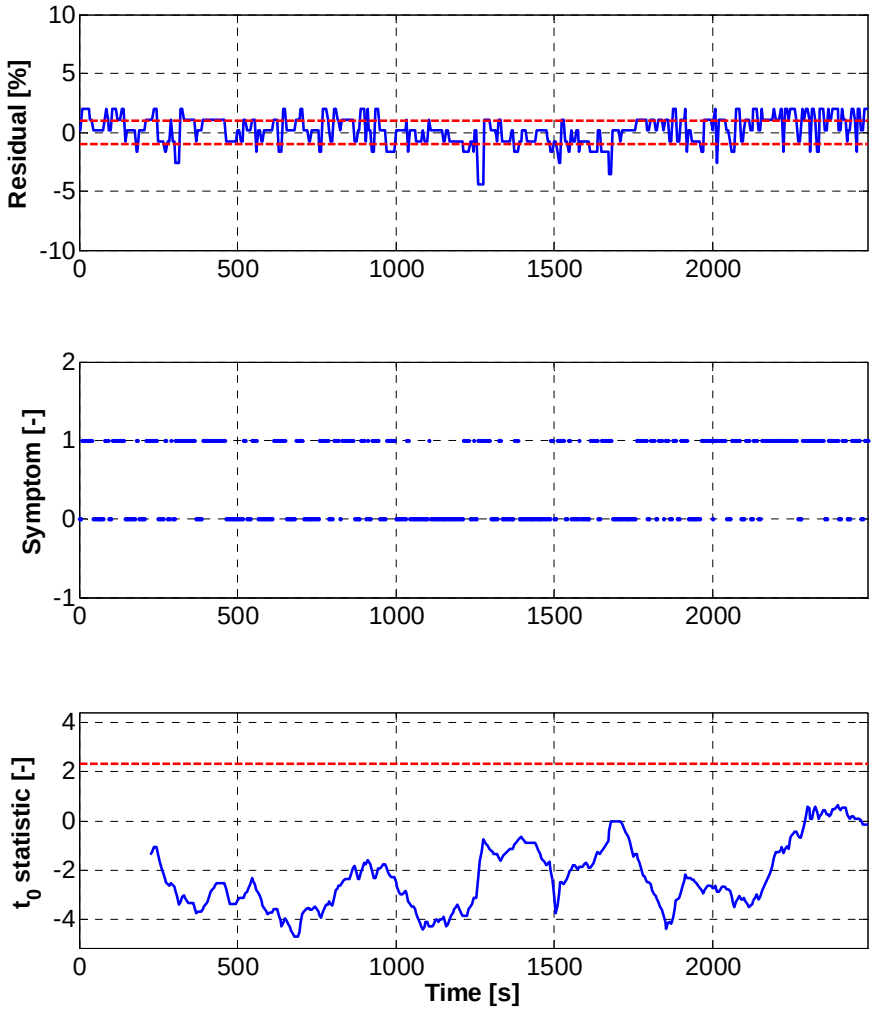

Figure 5.15 Exhaust blower power residual, analytical symptom and t_0 statistic related to a surface degradation of the CPO.

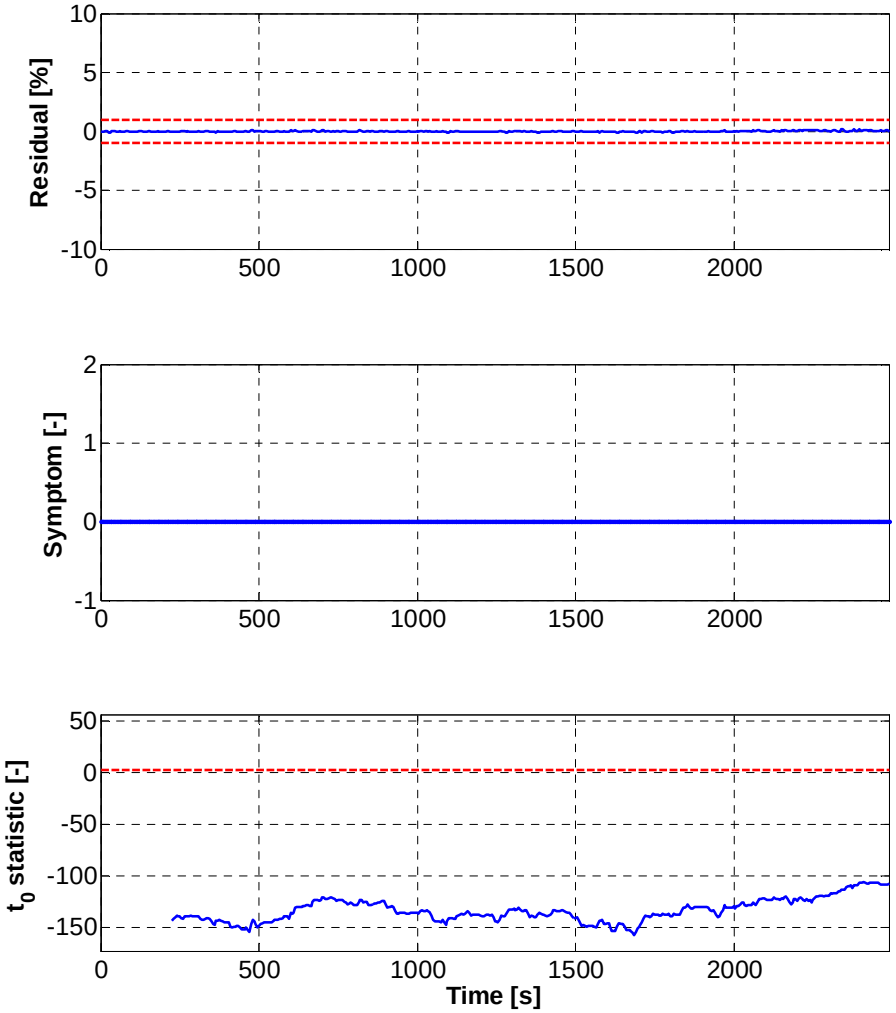

Figure 5.16 Stack temperature residual, analytical symptom and t_0 statistic related to a surface degradation of the CPO.

What might be also interesting to notice is that, although the t_0 statistic related to the stack power is still beyond the H_0 rejection limit also after the fault ending at 1730 s, no detection is obtained since the symptoms are all 0 after that moment. This conclusion remarks again the importance to combine both the symptoms and the t_0 statistic trend to perform a reliable detection.

5.2.5 Stack fault validation results

The last considered fault entails the increase in the stack ohmic resistance, described in details in paragraph 4.3.5. The results concerning the stack power, the exhaust blower power and the stack temperature are presented in Figure 5.17, Figure 5.18 and Figure 5.19 respectively, in terms of residuals, analytical symptoms and t_0 statistics.

In accordance with the experimental results described in paragraph 4.3.5, the stack power residual presented in Figure 5.17 is evidently affected by the induced fault. Indeed, it shows abrupt changes, as those displayed in Figure 4.11 by the stack power measured signal. The residual goes under the -1% threshold limit at 600 s, around 1 minute after the first electrical box resistance switch (see Figure 4.11), reaching then a minimum value of about -7%, in correspondence to an electrical resistance of 60 mΩ. It finally returns into the ±1% threshold range at 3000 s. This residual behavior leads all the symptoms within 600 s and 3000 s to be 1. But, according to the t_0 statistic trend, only those after 760s can be ascribed to a faulty state.

Concerning the exhaust blower power residual showed in Figure 5.18, it exhibits strong oscillations which induce the repeated crossing of both the ±1% thresholds limits during the whole considered timespan. Furthermore, the residual values are located more frequently around the +1% threshold level, especially in the first half of the time window, showing a maximum value of +3.8% around 1750 s and then returning between the ±1% threshold range after 3000 s. This behavior is due to the lower sensitivity of the exhaust blower power to the induced fault, as described in paragraph 4.3.5. The direct consequence of this trend is that most of the symptoms values are equal to 1. However, a clearer interpretation of the fault effects on the exhaust blower power can be achieved through the related t_0 statistic trend. From Figure 5.18 it is possible to observe that the t_0 statistic crosses one time the H_0 rejection limit at 875 s, going again under this value until 1000 s. Then it crosses this limit for the second time at 1000 s, with an initial fluctuation, which induces few points to go under 2.326 at 1300s.

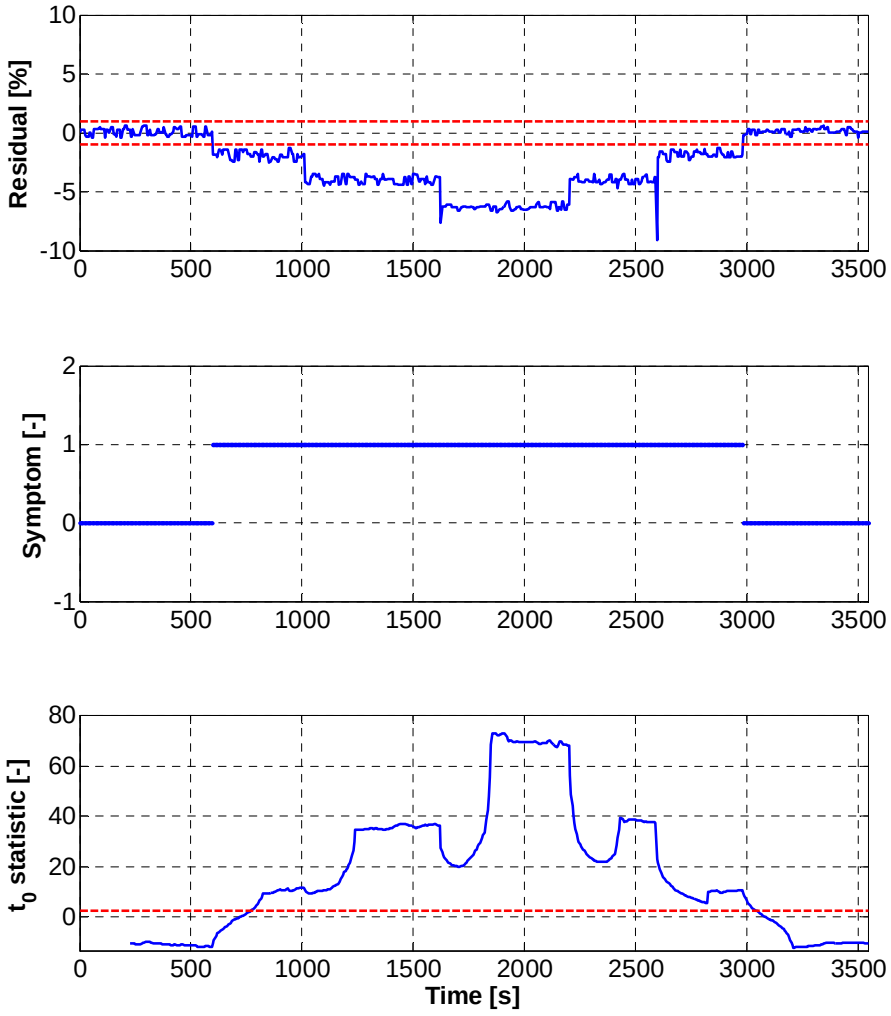

Figure 5.17 Stack power residual, analytical symptom and t_0 statistic related to an increase in the stack ohmic resistance.

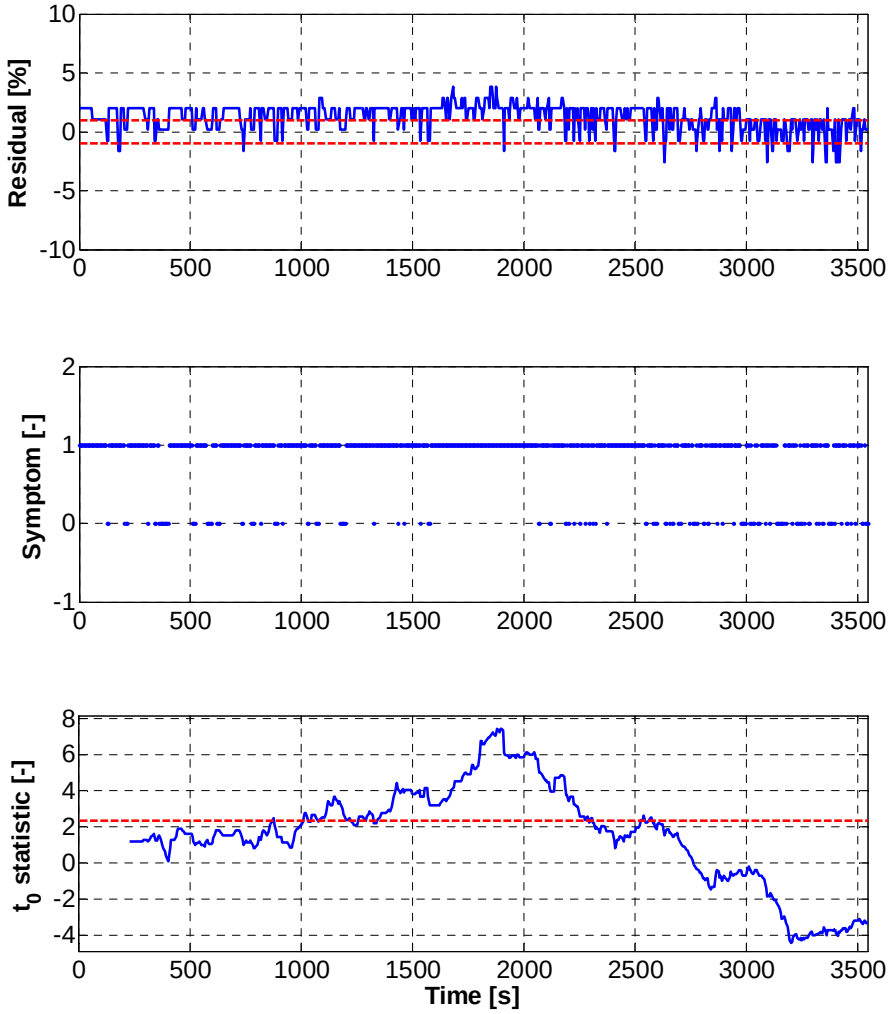

Figure 5.18 Exhaust blower power residual, analytical symptom and t_0 statistic related to an increase in the stack ohmic resistance.

After this moment, the t_0 statistic remains over the H_0 rejection limit until 2300 s, when it goes again under this value, with a last crossing at 2540 s. After this time, the t_0 statistic remains lower 2.326 until the end of the considered timespan.

About the stack temperature results presented in Figure 5.19, no effect

induced by this fault is visible, thus the stack temperature remains unchanged during the entire time window.

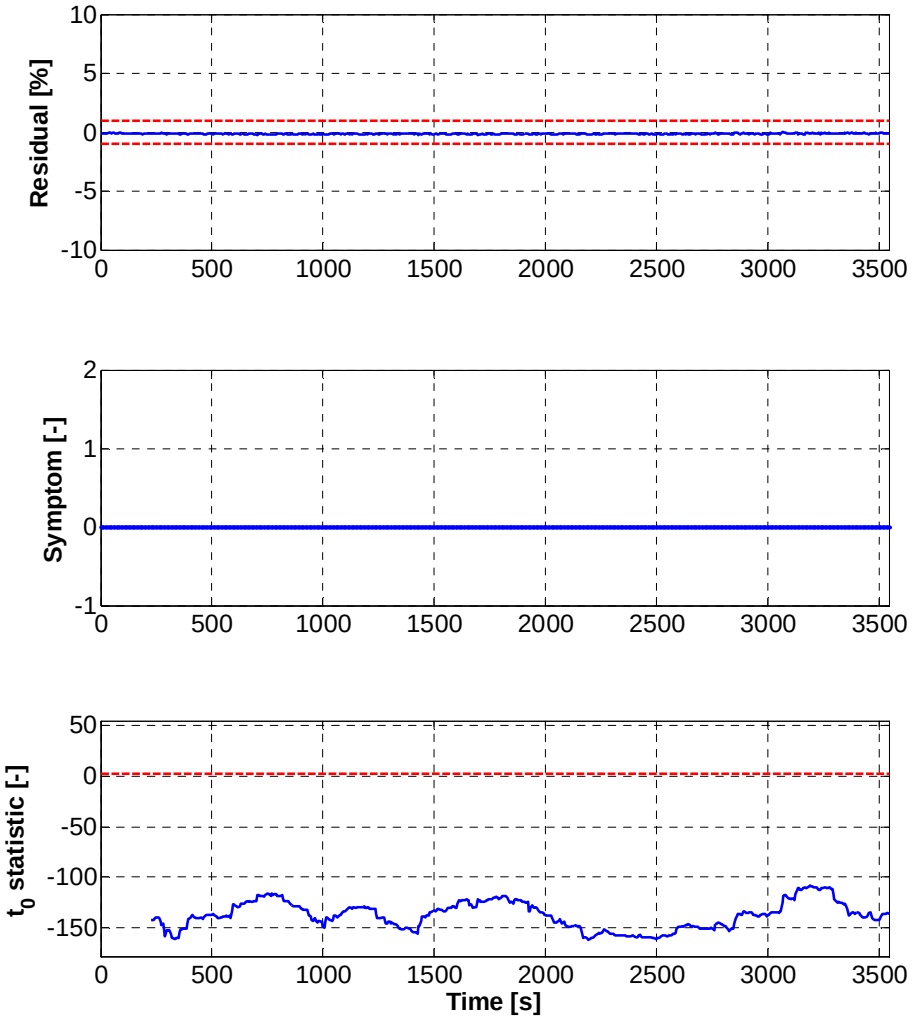

Figure 5.19 Stack temperature residual, analytical symptom and t_0 statistic related to an increase in the stack ohmic resistance.

From the evaluation of the obtained results it is possible to state that the variables affected by the current fault are the stack power and the

exhaust blower power. From the symptoms behavior here illustrated, coupled with the corresponding t_0 statistics trends, the obtained symptoms vector is [1 1 0]. As happened for the controller failure validation, this pattern has been reached after a certain period of time because the symptoms related to the stack power became 1 before those of the exhaust blower power. The initial pattern reached at 760 s is [1 0 0]. Then it alternates between [1 0 0] and [1 1 0] from 875 s until 1300 s, when it becomes steadily [1 1 0]. This pattern is kept until 2300 s, after which it alternates again between [1 0 0] and [1 1 0] until 2540 s, when it becomes [1 0 0] until 3000 s. Comparing the pattern [1 1 0] with each row of the FSM of Table 5.3, a perfect match with the one related to the fault f_5 is obtained. Since the fifth row of the considered FSM presents an unambiguous symptoms vector pattern, the fault is univocally isolated, ensuring that the algorithm correctly detects and isolates the expected fault. In this case the delay between the detection of a faulty state and the isolation of the correct fault is 9 minutes, which can be considered an acceptable amount of time. What should be also remarked is that the current induced fault can be univocally detected by this algorithm only if the electric resistance is 40 mΩ or higher. However, such a value can be considered still representative of an incipient fault.

With this last result, the complete successful validation of the presented diagnostic algorithm has been performed.

5.3 Graphic User Interface for the diagnostic algorithm online application

The validation process presented in the previous paragraphs has been successfully performed both offline and online on the Galileo 1000N at the EIFER's laboratories. Nevertheless, before its online implementation, the developed diagnostic algorithm required further adaptations.

The first tackled issue concerned the algorithm computational speed. Indeed, the online data treatment processes (i.e. data reading, residuals calculation, symptoms generation, t_0 statistic evaluation and fault isolation) should be performed with a frequency higher or at least equal to the one required by the HexisViewLogger for the data saving (which is

0.2 Hz). This constraint is mandatory to avoid the writing/reading superimposition of the diagnostic algorithm and the system control software during data transfer (see paragraph 5.1.1). For this purpose, by means of an optimized software programming, the developed diagnostic algorithm has been capable to perform the data treatment process with a frequency higher than 0.2 Hz on a PC with an Intel Core 2, Duo CPU (3.16 GHz), 3.46 GB of RAM and Microsoft Windows XP as operating system.

Another crucial issue has been the verification of the onboard algorithm implementation. For this purpose, the diagnostic algorithm has been coupled with a dedicated Graphic User Interface (GUI) and embedded into a comprehensive executable file implemented on board (i.e. on the same PC running the Galileo 1000N control software).

The development of a GUI has been mainly motivated by the need for a rapid and easy tuning of the algorithm and for the real time checking of its functionalities and the diagnosis results. The use of such a GUI has been also a proof of the easiness of use of the developed algorithm.

In Figure 5.20 the flow chart of the whole online diagnostic algorithm is presented, whereas in Figure 5.21 and Figure 5.22 the screenshots of the GUI during its application are showed, for normal and faulty behaviors of the Galileo 1000N, respectively. It is worth noting that the flow chart describes step by step the diagnostic procedure, including the interaction with the user and the possible results of the diagnosis. Moreover, the blocks presented in Figure 5.20 have a direct coincidence with the buttons and the panels in Figure 5.21 and Figure 5.22.

After starting the algorithm (i.e. lunching the executable file – *Start* block in the flow chart), the first step consists in the verification of the communication protocol between the algorithm and the Galileo 1000N control software. This task is accomplished by pushing the *Connect* button in the upper left corner of the GUI (i.e. the *Connect* block in the flow chart): if the communication text file is found, the CONNECTION STATUS panel, located in the lower left part of the GUI, displays the string “System Connected”; on the other hand, if the text file is not present in the defined path, the panel displays “Warning: File Missing”.

The second step consists in the definition of the threshold levels (*Threshold selection* block in the flow chart). The THRESHOLD SELECTION panel allows the user to select the thresholds in two ways: *one for all*, for a common value for all the monitored variables, and *one*

by one, for a specific value for each monitored variable. In the proposed examples (Figure 5.21 and Figure 5.22) the same threshold levels are chosen for all the variables and they have been set equal to ±1%. If the user does not manually select the threshold levels, the thresholds are automatically set equal to ±1% for all the monitored variables.

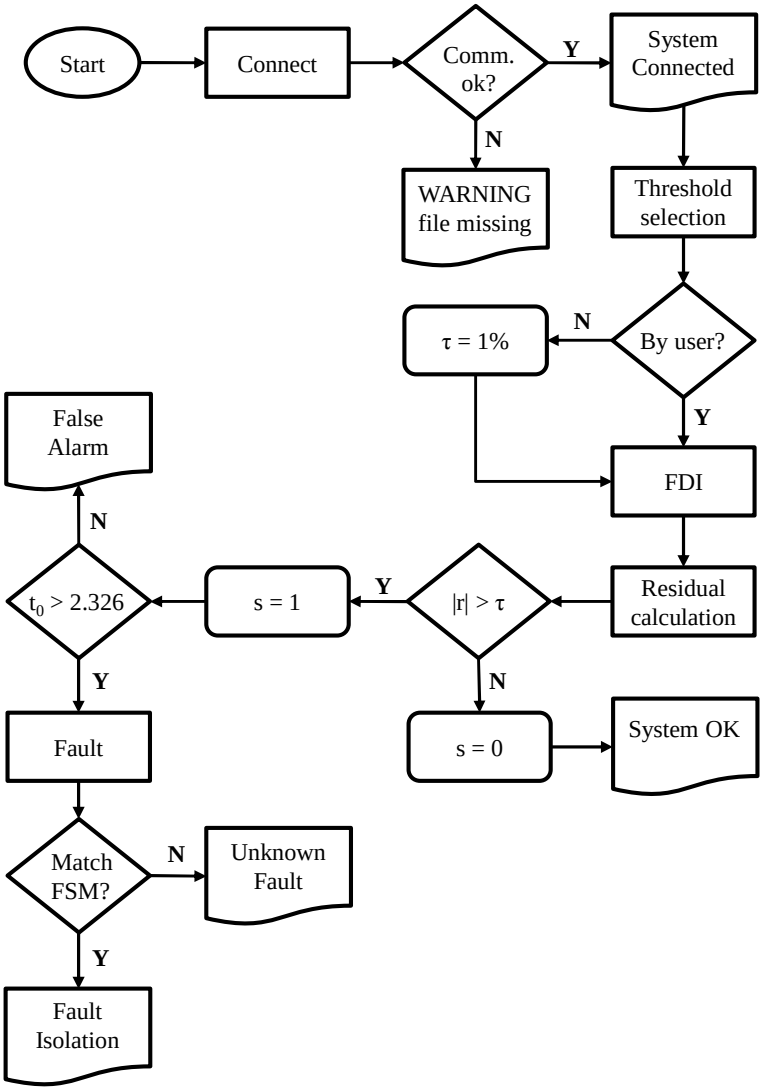

Figure 5.20 Online diagnostic algorithm flow chart.

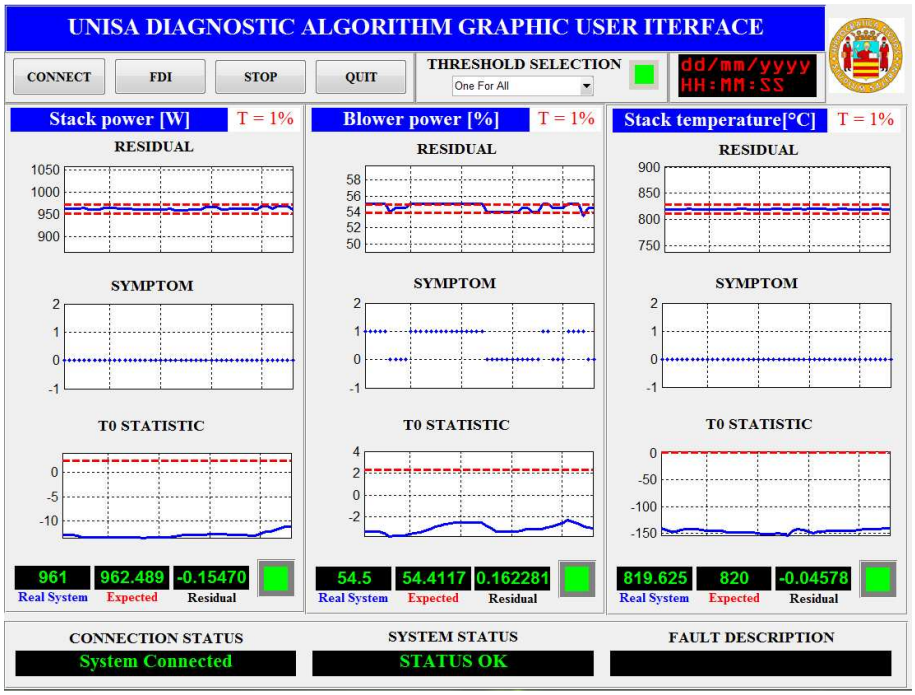

Figure 5.21 Diagnostic algorithm GUI during system monitoring in normal operating condition.

Once the communication protocol is established and the thresholds are set, the entire diagnosis procedure can be started by pushing the FDI button in the upper left side of the GUI. During its online application, the algorithm can always be paused or closed by pushing the STOP or the QUIT buttons, respectively. During the diagnosis, the residuals are computed by the algorithm (*Residual calculation* block in the flow chart) and then compared to the threshold levels: if a residual lies within the threshold range, the related symptom is 0, otherwise it becomes 1. If all the considered symptoms are 0, the system is assumed in normal condition and the SYSTEM STATUS panel displays the string “STATUS OK”. Moreover, if one or more symptoms are equal to 1, to understand if a fault is occurring or the event can be classified as a false alarm, the t_0 statistic related to each symptom is investigated. If it is lower than 2.326, the symptom is relate to a false alarm, otherwise a fault is taking place. In the first case, the SYSTEM STATUS panel also displays the string

"STATUS OK". In the other case, the SYSTEM STATUS panel displays the string "WARNING FAULT" and all the arisen symptoms are gathered into a symptoms vector, then compared to the FSM (*Fault* block in the flow chart). If a match occurs (*Fault isolation* block), the specific fault is isolate: the FAULT DESCRIPTION panel displays the string with the fault type. On the other hand, if no match occurs (*Unknown fault* block) the FAULT DESCRIPTION panel displays the string "UNKNOWN FAULT".

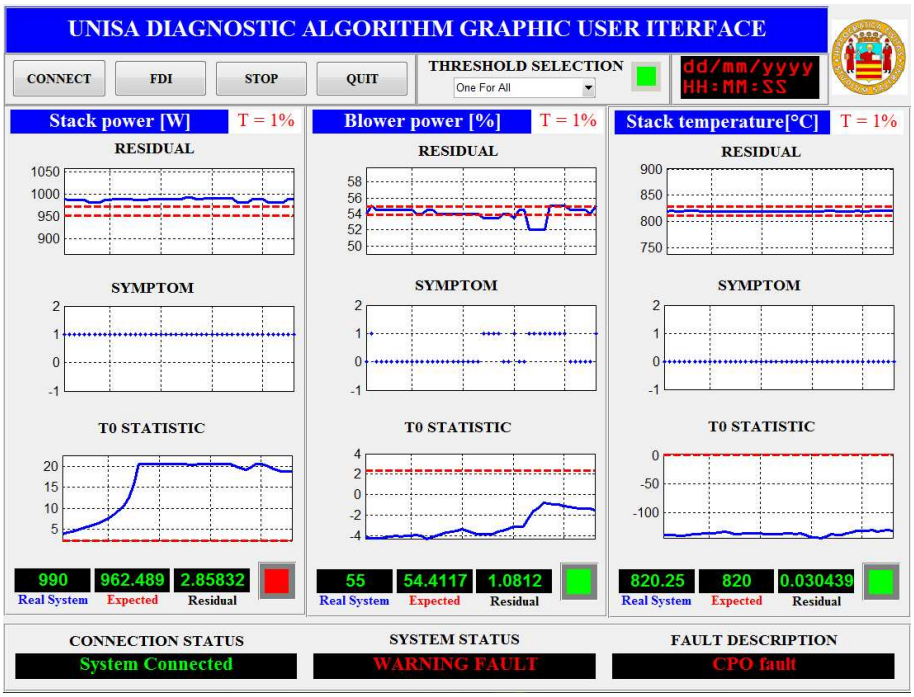

Figure 5.22 Diagnostic algorithm GUI during system monitoring in faulty operating condition: the CPO fault is correctly isolated.

Considering the GUI screenshot in Figure 5.21, it is possible to observe that in the central part of the GUI the plots of the residuals, with the ±1% threshold range, the symptoms behaviors and the t_0 statistic trends of the three monitored variables are showed. Moreover, under each plot, the current acquired value (REAL SYSTEM panel), the current simulated value (EXPECTED panel) and the current residual value

(RESIDUAL panel) of the monitored variables are displayed, coupled with a control square. When a symptom being 1 is associated to a faulty state through the t_0 statistic, the square becomes red, otherwise it is green, meaning that the variable is in faulty or in normal condition, respectively. In the proposed example, the diagnostic algorithm correctly identifies the system normal operating condition, showing in the SYSTEM STATUS panel the string “STATUS OK”. Moreover, the control squares, located at the right side of each RESIDUAL panel, are all green. In this case, all the arisen symptoms are classified as false alarms.

In Figure 5.22, instead, the correct online isolation of the CPO fault is presented. In this case, it can be observed that the SYSTEM STATUS panel displays the string “WARNING FAULT” and the FAULT DESCRIPTION panel displays correctly the isolated fault type. Indeed, the only control square which becomes red is that of the stack power residual, which is the only variable influenced by the considered fault, in accordance with what presented in paragraph 5.2.4.

The same successful results have been obtained applying the diagnostic tool online during the induction of the other faults (not displayed here for the sake of brevity).

CHAPTER 6 Conclusions

In this manuscript the complete procedure for the development and the application of a model-based diagnosis algorithm oriented towards Solid Oxide Fuel Cell (SOFC) systems has been presented. Part of the results presented in this dissertation have been carried out within the framework of the European Project GENIUS (Generic diagnosis instrument for SOFC systems – grant agreement n° 245128). The main objectives of this work have been the characterization of the basic elements of the diagnostic algorithm and the organization of the procedure required for their development and implementation, aiming at both an offline and an online diagnosis. Furthermore, an experimental activity has been carried out for the induction of controlled faulty states on a pre-commercial micro-Combined Heat and Power (μ-CHP) SOFC system, the Galileo 1000N, manufacture by the Swiss company HEXIS AG. The same system has been also exploited for the validation of the developed diagnostic algorithm.

A model-based approach has been followed for the development of a reliable diagnostic algorithm. Several elements have been identified as mandatory components: i) a mathematical model for the calculation of residuals during the monitoring phase, ii) specific threshold levels for the generation of symptoms during the detection phase and iii) a Fault Signature Matrix (FSM) for the location of the faulty component during the isolation phase. A specific methodology has been defined for the offline design and characterization of the whole algorithm and its further application on the Galileo 1000N.

First of all, the improvement of an SOFC system model, available in literature [1][2], has been performed, so as to simulate the behaviors of a generic SOFC system both in normal and faulty conditions. Five sub-models have been developed, with respect to the following faults: i) an increase in the air blower mechanical losses, ii) an air leakage, iii) the failure of the temperature controller, iv) the corrosion of the pre-reformer heat exchange surface and v) an increase in the cell ohmic resistance.

The simulation of the aforementioned faults allowed deriving quantitative relationships linking the monitored variables variations and the faults magnitudes. This analysis represented one of the main innovations brought by the presented research activity. The obtained results have been exploited for the improvement of an existing Fault Signature Matrix (FSM), developed by Arsie et al. [4] following a Fault Tree Analysis (FTA) approach. Both the direct and the indirect correlations among the faults and the monitored system variables have been also considered. Residuals have been first computed for each monitored variable, comparing the values simulated by the SOFC system model both in normal and faulty conditions. Then, the obtained residuals have been compared to percent threshold levels, i.e. ±1% and ±5% of the variable values at normal condition, to understand the sensitivity of the monitored variables to the considered faults.

The obtained results highlighted that the development of an FSM following only a heuristic approach might lead to a non-optimal fault isolation. Indeed, the knowledge of the real effects of a fault on the influenced variables become essential to meet the requirements and cope with the limitations of real system applications, such as the monitoring of only a limited number of variables, or the availability of measurement devices with low resolution. Especially in this last case, the exploitation of such kind of measurement devices drives the choice towards high threshold levels, which might hinder the univocal isolation of single faults, as showed assuming a threshold level of ±5%. On the other hand, by setting low threshold levels, such as ±1%, it is possible to avoid redundancy problems and detect incipient faults, but high resolution devices (i.e. high costs) and accurate monitoring models (i.e. high computational burdens) could be necessary.

Once identified all the algorithm components, a characterization procedure has been followed to adapt the whole algorithm on the Galileo 1000N. Primarily, the available monitored variables with respect to those listed in the FSM have been identified as: i) stack power, ii) blower power and iii) stack temperature. Then, the mathematical model required for the simulation of the aforementioned variables in normal condition has been characterized. The need for a fast and handy model, which can be rapidly tuned by the algorithm user, led to the choice of a map-based model rather than a more complex one, such as that used for the FSM improvement. Indeed, especially for pre-commercial systems, the SOFC

stack characteristics might rapidly change due to further improvements on the production line, which can be mandatory for the market release of the final version of a system. The map-based model exploits numerical maps, taking as input the values of the controlled set-points at a specific operating condition and returning as output the values of the monitored variables for that operating condition. For this purpose, the monitored variables have been measured at a specific operating condition, and the averages of the acquired signals have been computed. This procedure allowed the development of a model without requiring either a large number of experimental data (i.e. long term experiments) or the computation of specific parameters (sometimes based on information hard to retrieve).

The computation of the variables standard deviation and quantization error allowed setting a threshold level of ±1% for the symptoms generation. This value and the list of the monitored variables have been exploited for the FSM characterization. However, the availability of only three symptoms for the isolation of five different faults (i.e. those accounted into the FSM) led to two faults with the same pattern, that are the increase in the blower mechanical losses and the leakage at stack outlet. Consequently, they have been grouped into a common cluster, hindering the possibility to perform a univocal isolation of these two faults.

A further element has been included into the algorithm in order to perform a probabilistic analysis of the results instead of a deterministic one. Indeed, the probability of false alarm and missed fault have been included within the symptoms evaluation procedure through a statistical hypothesis test. This test allowed associating an arisen symptom to a real faulty state or to a false alarm evaluating a statistic with a *t* distribution. The comparison of this statistic to a specific null hypothesis rejection level allowed this discrimination.

For the validation of the developed diagnostic algorithm a dedicated experimental activity has been performed. This activity dealt with the induction of controlled faulty states on the Galileo 1000N. The further original feature of this work consisted in the design of specific procedures to mimic faults on a real SOFC system. For the induction of three faults, that are the increase in the blower losses, the temperature controller failure and the degradation of the catalytic partial oxidizer (CPO) surface, the procedure involved only software maneuvers. On the other hand, the

air leakage and the increase in the cell ohmic resistance required specific hardware modifications. More in details, a hole has been drilled right after the stack exhausts for the leakage induction. This hole has been then connected to a faucet in order to regulate the leak amount. The location of the leakage has been chosen with respect to the system configuration and specific mechanical constrains. Moreover, the increase in the cell ohmic resistance has been mimicked by means of a resistor box connected in series with the positive terminal of the stack. The design of the faults experimental induction has been performed considering that in some cases only the faults effects were reproducible instead of mimicking the causes.

The signals measured during the faults experimental induction have been exploited for the algorithm validation. Each induced fault has been correctly detected and univocally isolated, except for the increase in the blower losses and the leakage. Since these faults have been grouped into a fault cluster, their isolation was not univocal, but the expected fault cluster has been correctly isolated in both cases. These results proved the capability of the designed algorithm to perform a reliable and precise fault diagnosis. It has been demonstrated that a combined interpretation of the symptoms and the hypothesis test statistics led to a robust detection of the faulty events. Moreover, the analysis of the detection and isolation delays remarked the importance of waiting a certain amount of time before performing a reliable inference on the system status.

The validation has been performed both offline and online. For the online algorithm application, a specific communication protocol has been developed, connecting the Galileo 1000N control software with the developed algorithm by means of a text file. Moreover, a dedicated graphic user interface has been developed to allow an easier algorithm management and a real-time interpretation of the results.

CHAPTER 7 Appendix

7.1 Introduction

In this chapter, an insight into the further activity performed on the Galileo 1000N system within the framework of the European project GENIUS is given. This activity was carried out in addition to the experiments described in Chapter 4 and it was performed at the EIFER laboratories in the frame of a student exchange program between the University of Salerno and the EIFER institute.

More in details, the work dealt with the contribution to the *2nd Experimental Test Plan*, scheduled on the Galileo 1000N in the Description of Work of the GENIUS project. The main accomplishments concerned the acquisition of experimental data, the control of the Galileo 1000N operating conditions through the HexisView software and the collection of EIS spectra by means of a dedicated EIS station, manufacture by the Italian company MaterialsMates Italia©. The data gathered during this activity have been useful to understand the system behaviors and to highlight significant issues for the diagnostic algorithm development. In particular, the measurement of EIS spectra has been worthwhile for the periodic evaluation of the system status. Indeed, as stated in [44], the evaluation of an EIS spectrum shape gives direct information about the status of the SOFC stack. The comparison of these spectra in time has been a further indicator used within the GENIUS project to evaluate if the Galileo 1000N system operation was still normal after specific experimental maneuvers, as showed in paragraph 7.3.4.

A detailed description of the Galileo 1000N system and the EIFER test bench has been given in paragraph 4.1. To perform the EIS spectra acquisition, the Galileo 1000N system is connected to an EIS station, developed by the MaterialsMates Italia© company. This station is

characterized by two electronic loads and a dedicated EIS software, installed on a standard PC. Figure 4.3 gives a picture of the aforementioned EIFER test bench with the Galileo 1000N system, the EIS station and other components. Because the EIS station is separated from the electrical feed/supply system, to perform the EIS spectra measurement a specific switching procedure has to be followed. For this purpose, a customized switch is located between the Galileo 1000N stack and the inverter. By using this switch it is possible to disconnect the stack output from the inverter and to connect it to the electronic load of the EIS spectrometer.

7.2 2nd Test Plan Description

The purpose of the *2nd Experimental Test Plan* was the collection of the monitored variables values at different operating conditions, as the one presented in paragraph 5.1.2. It is worth noting that the working operating points were defined following a randomization methodology. The control parameters are those listed in Table 5.1 and here recalled:

- Stack temperature;
- Single cell voltage;
- Gas input power;
- λ_{CPO}.

As shown in Figure A.1, 52 operating points were chosen within a triangular domain according to the Galileo 1000N system limitations, defined by the manufacturer (i.e. HEXIS AG limit curve). The points labelled with a green X are the corner points, while the one labelled with the yellow X is the nominal operating condition corresponding to that represented in Table 5.1, which was chosen as the reference one for the diagnostic algorithm validation.

Only the nominal condition and the corner points were investigated with EIS, while the other points (i.e. generic conditions) were measured to give as much information as possible on the Galileo 1000N system operation. More in details, the values of the four control parameters for each operating condition are given in Table A.1. The column EIS

specifies if the EIS measurement was performed at that specific operating condition, whereas the last column defines the point type: nominal condition point (NC), generic condition point (GC) or domain corner point (DC).

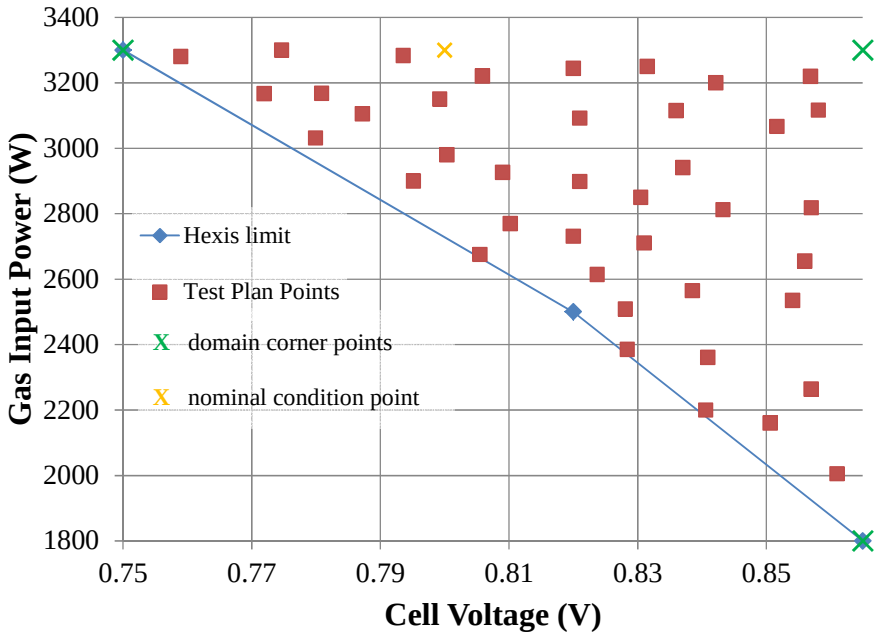

Figure A.1 *2nd Experimental Test Plan* domain and DOE operating points.

Table A.1 *2nd Experimental Test Plan* set-point values.

Operating point (#)	Stack temperature (°C)	Cell voltage (V)	Gas input power (W)	λ_{CPO} (-)	EIS	Operating point type
01	820	0.8000	3300	0.29	yes	NC
02	850	0.8569	3220	0.28	no	GC
03	850	0.8406	2200	0.29	no	GC
04	850	0.8385	2565	0.30	no	GC
05	850	0.8409	2361	0.31	no	GC
06	850	0.865	3300	0.32	yes	DC
07	850	0.8422	3200	0.28	no	GC
08	850	0.8305	2850	0.29	no	GC
09	850	0.8281	2508	0.30	no	GC

10	850	0.8541	2534	0.31	no	GC
11	850	0.865	1800	0.27	yes	DC
12	850	0.8210	2898	0.28	no	GC
13	850	0.8102	2770	0.29	no	GC
14	838	0.8004	2980	0.30	no	GC
15	840	0.7952	2900	0.31	no	GC
16	820	0.8000	3300	0.29	yes	NC
17	827	0.7799	3031	0.28	no	GC
18	840	0.8055	2675	0.29	no	GC
19	835	0.8200	2731	0.30	no	GC
20	827	0.8370	2941	0.31	no	GC
21	800	0.865	3300	0.32	yes	DC
22	830	0.8200	3244	0.28	no	GC
23	834	0.8433	2812	0.29	no	GC
24	841	0.7992	3150	0.30	no	GC
25	841	0.7747	3300	0.31	no	GC
26	800	0.7500	3300	0.27	yes	DC
27	828	0.8517	3066	0.28	no	GC
28	841	0.8506	2160	0.29	no	GC
29	841	0.8610	2005	0.30	no	GC
30	833	0.8570	2264	0.31	no	GC
31	820	0.8000	3300	0.29	yes	NC
32	838	0.8581	3116	0.28	no	GC
33	827	0.8090	2926	0.29	no	GC
34	832	0.8560	2655	0.30	no	GC
35	840	0.8284	2385	0.31	no	GC
36	850	0.7500	3300	0.32	yes	DC
37	838	0.8315	3250	0.28	no	GC
38	841	0.8237	2614	0.29	no	GC
39	836	0.8360	3115	0.30	no	GC
40	826	0.8210	3092	0.31	no	GC
41	800	0.8650	3300	0.27	yes	DC
42	839	0.7936	3283	0.28	no	GC
43	840	0.7590	3280	0.29	no	GC
44	836	0.7719	3167	0.30	no	GC
45	838	0.7872	3105	0.31	no	GC
46	820	0.8000	3300	0.29	yes	NC
47	837	0.8059	3221	0.28	no	GC
48	831	0.7809	3168	0.29	no	GC
49	836	0.8310	2710	0.30	no	GC
50	828	0.8570	2818	0.31	no	GC
51	820	0.8000	3300	0.29	yes	NC

Before undergoing the test measurements, the Galileo 1000N had been run through a start-up phase, characterized by four sub-phases: reduction, activation, initialization and conditioning. Figure A.2 gives a representation of the procedure, focusing on the natural gas power input and the DC and AC power output.

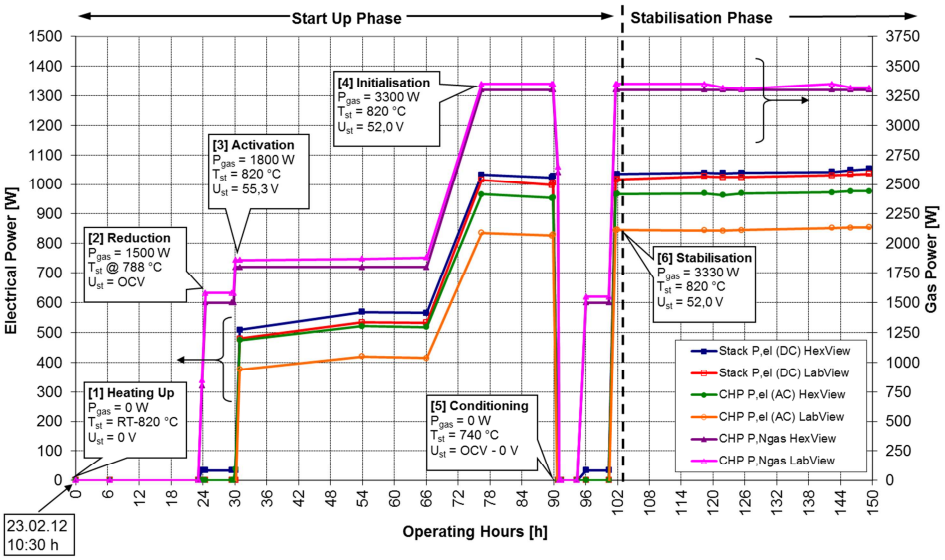

Figure A.2 Example of the natural gas power input and DC and AC power output behaviors during the Galileo 1000N start-up phase, acquired by both the HexisView software and a LabVIEW acquisition algorithm developed by EIFER.

After the conditioning, the system reached the stabilization phase and was kept at a fixed operating condition for more than 700 hours, before starting the *2nd Experimental Test Plan* measurements.

The standard procedure for each operating point was characterized by a transient manoeuver from a condition to another (according to the order of Table A.1), followed by a stabilization phase and a long term acquisition at steady state. Then, the EIS spectra were acquired when planned.

7.3 Examples of data plots

The information gathered during the *2nd Experimental Test Plan* refer to four different kinds of data: transients, long term acquisitions, V-I curves and EIS spectra. The transient data concern the change from one operating condition to another; the long term data refer to the stabilization and steady state phases at each point; the V-I curves offer a representation of the stack characteristic as the stack voltage plotted against the current drawn from the electric load; finally, the EIS spectra are those collected by means of the MaterialsMates Italia© company EIS station at the designed operating conditions.

7.3.1 Transient

An example of data plot related to a transient maneuver is given in Figure A.3. Here the change from the operating point #5 to the operating point #6 is considered (see Table A.1 for further details).

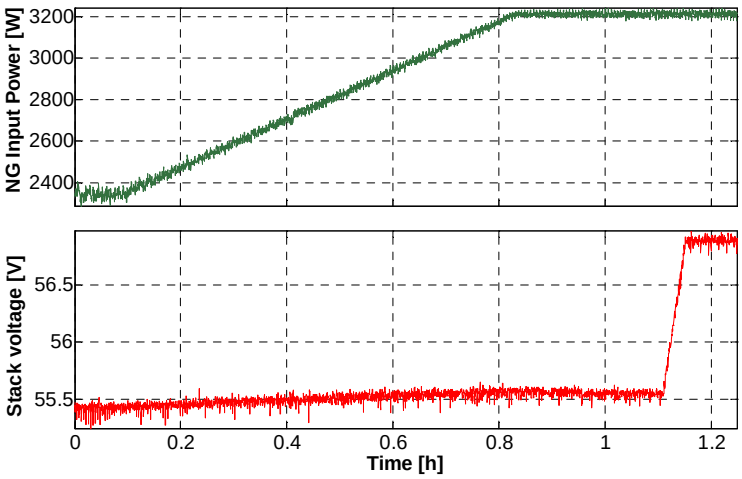

Figure A.3 Example of transient manoeuver from operating point #5 to operating point #6.

To properly drive the system from one operating condition to another, only one parameter at a time is changed, waiting for the system stabilization before each change. This precaution is essential to avoid unexpected or dangerous states, leading the system to the safety mode alarm and to a consequent shut-down. All the parameters are changed following a specific rate, e.g. 0.35 W/s for the gas input power and 0.01 V/s for the stack voltage.

As explained in Chapter 2, taking into account such procedure becomes essential for the development of a dynamic model in order to avoid the wrong interpretation of a transient maneuver as an undesired or faulty condition.

7.3.2 Long Term

The long term data give an overview of the system variables behaviour during the steady state at a specific operating condition. Furthermore, these data contain also EIS spectra measurements as part of the same data matrices. An example is given in Figure A.4, where the long term plots of the stack voltage and the stack current are presented for the operating point #6.

In this plot, it is possible to observe the switching procedure done before performing EIS spectra measurements. During the normal operation, the fuel cell stack is connected to the inverter and the system delivers power directly to the electrical grid. To record EIS spectra, the stack is first brought to OCV (almost 63 V) and the inverter is disconnected, using a dedicated electrical switch. Then, the stack is connected to the EIS station electronic loads and the voltage is driven to its minimum value (i.e. around 52.5 V). This procedure is done with the purpose of acquiring a V-I curve. Then, the voltage is brought up to OCV again (i.e. another V-I curve measurement) and the stack is then reconnected to the inverter.

In Figure A.4, four EIS spectra are recorded ramping up the voltage to OCV: two at 0.8 V/cell, one at 0.865 V/cell and one at 0.9 V/cell. It is worth remarking that the EIS measurements were performed in order to have a side evaluation of the system status.

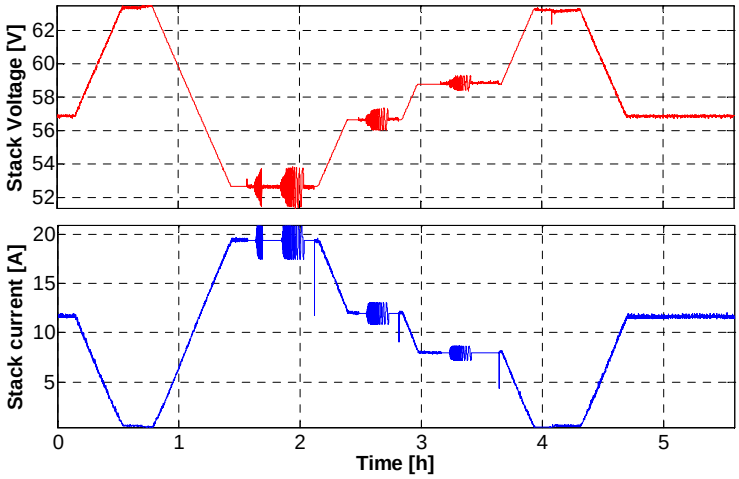

Figure A.4 Example of long term data for condition #6 and the switching procedure from the inverter to the EIS device.

7.3.3 V-I curves

As described in the previous paragraph, V-I curves were measured bringing the voltage from OCV to the minimum and then ramping it back to OCV. The ramps are both at a constant rate of 4.5 mV/s. An example of V-I curves measured at the operating point #6 is given in Figure A.5.

The horizontal and vertical voltage-current picks correspond to the EIS spectra measurements and are related to the amplitude of the EIS AC signal injected into the stack. It is important to observe that the two V-I curves show the same slope, meaning that the system behavior was normal during both the ramps and also after each EIS spectrum measurement. Coupled with the EIS spectrum shape analysis, the evaluation of the V-I curves characteristics helps the system state monitoring and allows the evaluation of the system degradation in time. Indeed, the time comparison of the stack voltage at the same current is an indicator of the degradation progress. However, to understand which kind of mechanism might induce the system performance reduction, the V-I curve is not sufficient and the analysis of the related EIS spectra is required.

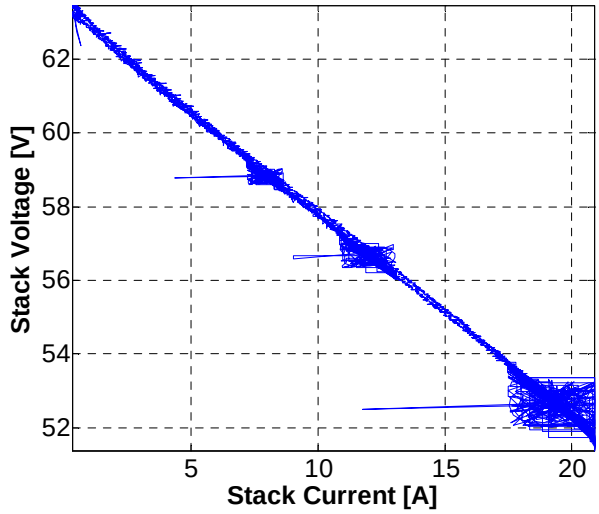

Figure A.5 Example of V-I curves data for the Galileo 1000N stack at condition #6.

7.3.4 EIS spectra

The EIS spectra acquisition was performed following the switching procedure described in paragraph 7.3.2. An example of EIS spectra plot is given in Figure A.6 and Figure A.7.

The spectra sketched in these figures were all measured at the reference point at 0.8 V/cell and at 0.9 V/cell respectively. In both the examples, it is possible to observe that the stack impedance shows a different behavior at 2478 hours and 2808 hours compared to the initial and final part of the tests. This discrepancy might be due to some problems experienced with the measuring equipment. However, almost at the end of the tests, the stack impedance shows behaviors closer to those of the initial spectra.

As previously mentioned, the study of the EIS shape helps the understanding of the system status, since its characteristics are strictly related to the physical phenomena occurring into the cells. The exploitation of such analysis might be coupled with the diagnostic algorithm presented in this manuscript in order to perform a more detailed

diagnosis on the stack behavior. This might be a future improvement for the SOFC diagnosis, aiming at a comprehensive estimation of both the system behavior (i.e. the stack and the BOP) coupled with a detailed insight into the SOFC inner status.

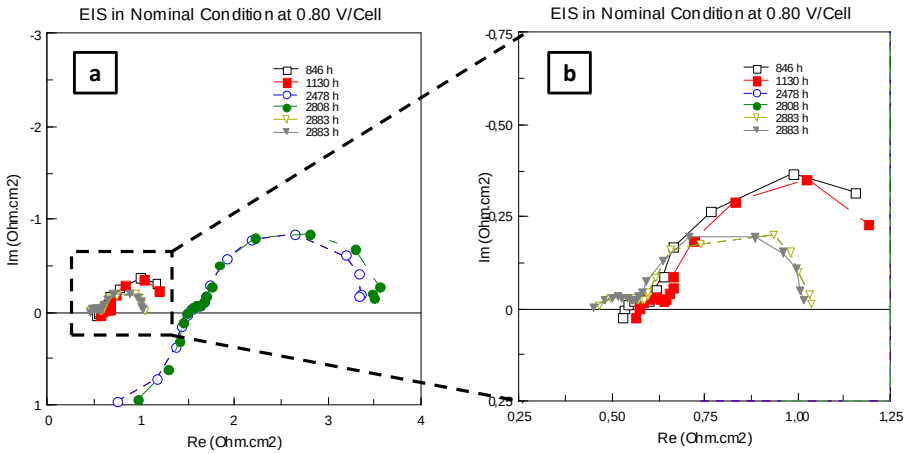

Figure A.6 Stack EIS spectra at 0.8 V/cell acquired at different times: global plot (a) and close-up (b).

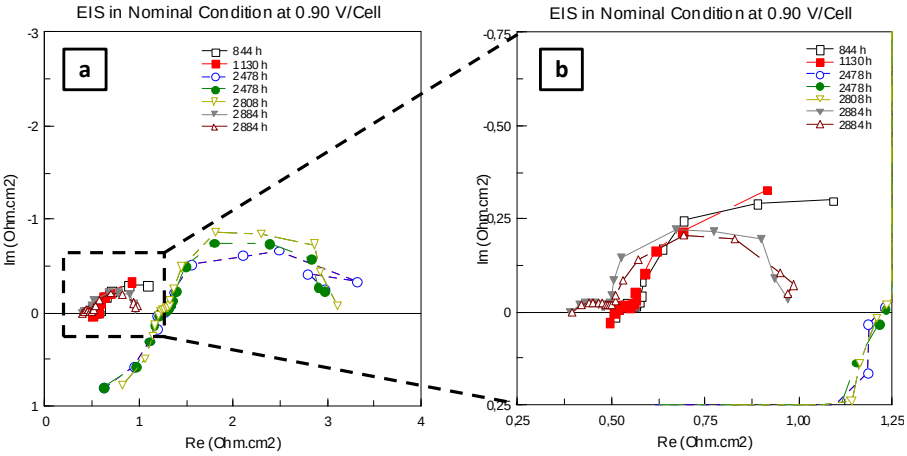

Figure A.7 Stack EIS spectra at 0.9 V/cell acquired at different times: global plot (a) and close-up (b).

References

[1] Sorrentino M., Pianese C., "Model-based development of low-level control strategies for transient operation of solid oxide fuel cell systems", *Journal of Power Sources* 196 (2011) 9036-9045.

[2] Sorrentino M., Pianese C., "Control oriented modeling of solid oxide fuel cell auxiliary power unit for transportation applications", *Journal of Fuel Cell Science and Technology* Vol. 6 (2009) 041011-1.

[3] Sorrentino M., Pianese C., Guezennec Y. G., "A hierarchical modeling approach to the simulation and control of planar solid oxide fuel cells", *Journal of Power Sources* 180 (2008) 380-392.

[4] Arsie I., Di Filippi A., Marra D., Pianese C., Sorrentino M., "Fault tree analysis aimed to design and implement on-field fault detection and isolation scheme for SOFC systems", *Proceedings of the ASME 2010 Eighth International Fuel Cell Science, Engineering and Technology Conference*, FuelCell2010, June 14-16, 2010, Brooklyn, New York, USA, FuelCell2010-33344.

[5] Singhal. C. S., Kendell K., "High Temperature Solid Oxide Fuel Cells: Fundamentals, Design and Applications", (2004), *Elsevier Ltd.*, The Boulevard, Langford Lane, Kidlington, Oxford OX5 1GB, UK.

[6] Braun R. J., "Optimal design and operation of solid oxide fuel cell systems for small-scale stationary applications", (2002), *Ph.D. Thesis*, Mechanical Engineering Department, University of Wisconsin – Madison.

[7] Arsie I., Flauti G., Pianese C., Rizzo G., Barberio C., Flora R., Serra G., Siviero C., "Confidence level analysis for on-board estimation of SI engine catalytic converter efficiency", *Proceedings of the SYSID 2000 IFAC Symposium on System Identification* (2000) 137–142.

[8] Zizelman J., Shaffer S., Mukerjee S., "Solid oxide fuel cell auxiliary power unit – a development update", *SAE Paper* No.

2002-01-0411 (2002).

[9] Isermann R., "Model-based fault-detection and diagnosis – status and applications", *Annual Reviews in Control* 29 (2005) 71-85.

[10] Isermann R., "Fault-Diagnosis Systems – An Introduction from Fault Detection to Fault Tolerance", (2006), *Springer*.

[11] Witczak M., "Identification and Fault Detection of Non-Linear Dynamic Systems", (2003), *University of Zielona Gora Press*, Poland.

[12] Veseley W. E., "Fault Tree Handbook", *Systems and Reliability Research, Office of Nuclear Regulatory Research*, (1981), U.S. Nuclear Regulatory Commission, Washington, D.C.

[13] Di Filippi A., "Fault Tree Analysis and development of a Fault Detection and Isolation scheme for SOFC systems", (2009), *Master Thesis*, Mechanical Engineering Department, University of Salerno, Italy.

[14] Yuhu D., Huilin G., Jing'en Z., Yaorong F., "Mathematical modeling of gas release through holes in pipelines", *Chemical Engineering Journal* 92 (2003) 237–241.

[15] Yuhua D., Huilin G., Jing'en Z., Yaorong F., "Evaluation of gas release rate through holes in pipelines", *Journal of Loss Prevention in the Process Industries* 15 (2002) 423–428.

[16] Huang Q., Hui R., Wang B., Zhang J., "A review of AC impedance modeling and validation in SOFC diagnosis", *Electrochemical Acta* 52 (2007) 8144-8164.

[17] Escobet T., Feroldi D., De Lira S., Puig V., Quevedo J., Riera J., Serra M., "Model-based fault diagnosis in PEM fuel cell systems", *Journal of Power Sources* 192 (2009) 216-223.

[18] Ingimundarson A., Stefanopoulou A. G., McKay D., "Model-based detection of hydrogen leaks in a fuel cell stack", *IEEE Transaction on Control System Technology*, Vol. 16, No. 5 (2008) 1004-1012.

[19] Fouquet N., Doulet C., Nouillant C., Dauphin-Tanguy G., Ould-Bouamama B., "Model based PEM fuel cell state-of-health monitoring via ac impedance measurements", *Journal of Power Sources* 159 (2006) 905-913.

[20] Kimmich F. et al., "Fault detection for modern Diesel engines using signal- and process model-based methods", *Control Engineering Practice* 13 (2005) 189-203.

[21] Simani S., Fantuzzi C., "Dynamic system identification and model-based fault diagnosis of an industrial gas turbine prototype", *Mechatronics* 16 (2006) 341-363.

[22] Leite A. C., Da Fonseca Lopes R. V., Kuga H. K., "Model-based fault detection on a reaction wheel", *DINCON 2006, Brazilian Conference on Dynamics, Control and Their Applications*, May 22 – 26 (2006) Guaratinguetà, SP, Brazil.

[23] Lo C. H., Wong Y. K., Rad A. B., "Model-based fault detection in continuous dynamic systems", *ISA Transaction* 43 (2004) 459-475.

[24] Chantler M., Aldea A., "A scheduling algorithm for time-constrained model-based diagnosis", *Engineering Applications of Artificial Intelligence* 11 (1998) 135-148.

[25] Papadopoulos Y., "Model-based system monitoring and diagnosis of failures using statecharts and fault trees", *Reliability Engineering and System Safety* 81 (2003) 325-341.

[26] Frank P., García E. A., Köppen-Selinger B., "Modelling for fault detection and isolation versus modelling for control", *Mathematics and Computers in Simulation* 53 (2000) 259-271.

[27] McKenzie F. D., Gonzales A. J., Morris R., "An integrated model-based approach for real-time on-line diagnosis of complex systems", *Engineering Applications of Artificial Intelligence* 11 (1998) 279-291.

[28] Kim Y., Rizzoni G., Utkin V., "Automotive Engine Diagnosis and Control via Nonlinear Estimation", *IEEE Control System*, Vol.18 (1998) 84-99.

[29] Ataer Ö.E., İleri A., Göğüş Y., "Transient behavior of finned-tube cross-flow heat exchangers", *International Journal of Refrigeration*, Vol. 18, No. 3, (1995), pp. 153-160.

[30] Zhang S., Yuan X., Wang H., Mérida W., Zhu H., Shen J., Wu S., Zhang J., "A review of accelerated stress tests of MEA durability in PEM fuel cells", *International Journal of Hydrogen Energy* 34 (2009) 388-404.

[31] Simani S., Fantuzzi C., Patton R. J., "Model-based fault diagnosis in dynamic systems using identification techniques", (2003) *Springer-Verlag New York*, Inc. Secaucus, NJ, USA.

[32] Omdahl T., "Reliability, Availability and Maintainability (RAM)

Dictionary", (1998), *ASQC Quality Press*, Milwaukee.

[33] Sorrentino M., "Development of a Hierarchical Structure of Models for Simulation and Control of Planar Solid Oxide Fuel Cells", *Ph.D. Thesis*, (2005), University of Salerno, Italy.

[34] Larminie J., Dicks A., "Fuel Cell System Explained, Second Edition", (2003), *John Wiley & Sons Ltd.*, The Atrium, Southern Gate, Chichester, West Sussex, England.

[35] EG&G Technical Services, Inc., "Fuel Cell Handbook (Seventh Edition)", (2004), *U.S. Department of Energy*, *Office of Fossil Energy*, National Energy Laboratory, Morgantown, West Virginia, USA.

[36] Colorado Fuel Cell Center web page www.coloradofuelcellcenter.org.

[37] Wikimedia Commons web page commons.wikimedia.org.

[38] George R. A., "Status of tubular SOFC field unit demonstrations", *Journal of Power Sources* 86 (2000)134-139.

[39] Marra D., "Development of Solid Oxide Fuel Cell stack models for monitoring, diagnosis and control applications", *Ph.D. Thesis*, (2012), University of Salerno, Italy.

[40] Kakaç S., Pramuanjaroenkij A., Zhou X. Y., "A review of numerical modeling of solid oxide fuel cells", *International Journal of Hydrogen energy* 32 (2007) 761-786.

[41] Bove R., Ubertini S., "Modeling solid oxide fuel cell operation: Approaches, techniques and results", *Journal of Power Sources* 159 (2006) 543-559.

[42] Faghri A., Guo Z., "Challenges and opportunities of thermal management issues related to fuel cell technology and modeling", *Internal Journal of Heat and Mass Transfer* 48 (2005) 3891-3920.

[43] Tsikonis L., "Approach on the Thermal Management and Parameter Estimation of Solid Oxide Fuel Cells and their Systems", *Ph.D. Thesis*, (2011), École Polytechnique Fédérale de Lausanne, Lausanne, Switzerland.

[44] Barelli L., Barluzzi E., Bidini G., "Diagnosis methodology and technique for solide oxide fuel cells: A review", *International Journal of Hydrogen Energy* 38 (2013) 5060-5074.

[45] Virkar A. V., "A model for solid oxide fuel cell (SOFC) stack degradation", *Journal of Power Sources* 172 (2007) 713-724.

[46] Larrain D., Van Herle J., Favrat D., "Simulation of SOFC stack

and repeat elements including interconnect degradation and anode reoxidation risk", *Journal of Power Sources* 161 (2006) 392-403.

[47] Gemmen R. S., Jhonson C. D., "Evaluation of fuel cell system efficiency and degradation at development and during commercialization", *Journal of Power Sources* 159 (2006) 646-655.

[48] Fuel Cells and Hydrogen Joint Undertaking (FCH JU) web page www.fch-ju.eu.

[49] European Project "Generic diagnosis instrument for SOFC systems (GENIUS)" web page genius.eifer.uni-karlsruhe.de.

[50] European Project "Degradation signature identification for stack operation diagnostic (DESIGN)" web page www.design-sofc-diagnosis.com.

[51] European Project "DC/DC converter-based diagnostic for PEM systems (D-CODE)" web page dcode.eifer.uni-karlsruhe.de.

[52] HEXIS AG Company web page www.hexis.com.

[53] Esposito A., Ludwig B., Moçoteguy P., Polverino P., Pianese C., Iwanschitz B., Mai A., "Experimental Investigation of an SOFC μ-CHP System for the Development and Validation of Diagnostic Algorithms", *5th Internationa Conference on Fundamentals & Dvelopment of Fuel Cells*, 16th-18th April, (2013), Karlsurhe, Germany.

[54] Polverino P., Pianese C., Sorrentino M., Esposito A., Ludwig B., Iwanschitz B., Mai A., "Experimental validation of a model-based diagnosis algorithm dedicated to a SOFC μ-CHP system", *5th Internationa Conference on Fundamentals & Dvelopment of Fuel Cells*, 16th-18th April, (2013), Karlsurhe, Germany.

[55] Di Domenico A., "A Dynamic model of automotive PEM Fuel Cell System for powertrain Design, Control and hierarchical model identification within Hardware in the Loop Fuel Cell Hybrid Testing", *Ph.D. Thesis*,(2006), University of Salerno, Italy.

[56] Kays W. M., London A. L., "Compact Heat Exchanger, 2nd Edition", *McGraw-Hill*, (1964), New York, USA.

[57] Montgomery D. C., Runger G. C., Hubele N. F., "Engineering Statistics, 3rd Edition", (2004), *John Wiley & Sons, Inc*.

[58] Nouri-Borujerdi A., Ziaei-Rad M., "Numerical Modeling of Transient Turbulent Gas Flow in a Pipe Following a Rupture",

Transaction B: Mechanical Engineering, Vol. 17, No. 2 (2010), pp. 108-120.

[59] Riascos L. A. M., Simoes M. G., Miyagi P. E., "On-line fault diagnostic system for proton exchange membrane fuel cells", *journal of Power Sources* 175 (2008) 419-429.

[60] Kamgar-Parsi B., Kamgar-Parsi B., "Evaluation of Quantization Error in Computer Vision", *IEEE Transaction on Pattern Analysis and Machine Intelligence*, Vol 11, No. 9, (1989), pp. 929-940.

[61] Awad M. M., "Fouling of Heat Transfer Surfaces, Heat Transfer – Theoretical Analysis, Experimental Investigations and Industrial Systems", *Prof. Aziz Belmiloudi (Ed.), InTech*, ISBN: 978-953-307-226-5.

[62] Isermann R., "Fault-Diagnosis Applications – Model-based condition monitoring: Actuators, drives, machinery, plants, sensors, and fault-tolerant systems", (2011), *Springer*.

[63] Bird R. B., Stewart W. E., Lightfoot E. N., "Transport Phenomena", (1960), *John Wiley & Sons, Inc.*

[64] Botti J. J., Grieve M. J., MacBain J. A., "Electric Vehicle Range Extention Using an SOFC APU", *SAE Paper* No. 2005-01-1172 (2005).

[65] Hendricks W. A., Robey K. W., "The sampling distribution of the coefficient of variation", *The Annals of Mathematical Statistics*, Vol. 7, No.3, (1936), pp. 129-132.

[66] Gray R. M., Neuhoff D. L., "Quantization", *IEEE Transaction on Information Theory*, Vol. 44, No. 6, (1998), pp. 2325-2383.